

NAL PROPOSAL No. 193
Scientific Spokesman: Z.G.T. Guiragossian
High Energy Physics Laboratory
W. W. Hansen Laboratories of
Physics
Stanford University
Stanford, California 94305
Telephone: (415) 327-7800 Ext. 333

NAL PROPOSAL FOR
DEEP INELASTIC ELECTRON SCATTERING; SEARCH FOR
INTERMEDIATE BOSONS, HEAVY LEPTONS, ANOMALOUS
LEPTONIC PROCESSES AND TESTS OF
QUANTUM ELECTRODYNAMICS

Submitted by

Z. G. T. Guiragossian, R. Hofstadter, R. F. Schilling, and M. R. Yearian
The W. W. Hansen High Energy Physics Laboratory and Department of Physics
Stanford University, Stanford, California 94305

and

E. V. Hungerford III, G. S. Mutchler, and G. C. Phillips
The T. W. Bonner Nuclear Laboratories and Department of Physics
Rice University, Houston, Texas 77001

and

B. W. Mayes
Department of Physics
The University of Houston, Houston, Texas 77001

October 1972*

*Proposals, 164-I and 164-II were originally submitted together
on December 1971. This proposal updates 164-II.

TABLE OF CONTENTS

	Page
Abstract	1
I. Introduction	2
II. Experimental Program	7
A. Search Experiments	7
1. Intermediate Vector Boson Search	8
2. Heavy Lepton Search	15
B. Electron Deep Inelastic Scattering	21
1. Deep Inelastic e-N Scattering Event Rates at NAL	26
2. Search for Lee-Wick Heavy Photons as Exchange Particles in Deep Inelastic e-N Collisions	32
3. Deep Inelastic Electron-Neutron Scattering	34
4. Two-Photon Interaction Processes in High Energy Electron-Proton Coulomb Collisions	36
C. Tests of Quantum Electrodynamics with Electron and Positron Beams	39
1. Tridents and Search of Lee-Wick Heavy Photons	40
2. Wide Angle Bremsstrahlung and Search for Heavy Excited Leptons	42
3. Inelastic Wide Angle Bremsstrahlung with Electrons and Positrons and Search for Nucleon Constituents	43
4. Search for Quark Production in Electromagnetic Processes	44

	Page
Summary	45
III. Experimental Method	47
A. Radiation Corrections in Electron-Proton Scattering	47
B. Beam Pion Impurity Corrections	49
C. 20 kgauss Superconducting Dipole Magnet	53
D. Experimental Configurations and Acceptances of the Spectrometer System	56
1. Detection of Showers Induced by Electrons and Gamma-Rays .	65
2. Muon Identifiers	67
3. Errors	68
Summary of Proposal Requirements	75
References	76
Appendix I. High Quality Electron / Photon Beam for NAL	

Proposal to the National Accelerator Laboratory
for
DEEP INELASTIC ELECTRON SCATTERING; SEARCH FOR
INTERMEDIATE BOSONS, HEAVY LEPTONS, ANOMALOUS
LEPTONIC PROCESSES AND TESTS OF QUANTUM ELECTRODYNAMICS

ABSTRACT

We propose to study deep inelastic electron scattering processes at incident electron and positron energies of 50 - 250 GeV, in the range of $Q^2 = 0.5 - 50 \text{ (GeV/c)}^2$ and hadronic mass values of up to 21 GeV, attainable only at NAL. We propose to observe energetic or high transverse momentum gamma rays in pairs or singles. We also propose to observe leptons, in pairs or as singles, emerging from electron-nucleon collisions, in coincidence with scattered electrons. In these studies we plan to search for structure in the effective mass continuum of various pair combinations or in the transverse momentum spectra in order to reveal with finer sensitivity the possible production of intermediate bosons, or Lee-Wick heavy photons and sequential heavy leptons. These processes will be studied in association with electron-nucleon scattering. Also, anomalous leptonic processes will be investigated. Important tests of Quantum Electrodynamics can be made by studying the wide angle bremsstrahlung process and the trident process produced by incident electrons and positrons. The behavior of time-like and space-like propagators, up to virtual mass values of 8 GeV will be explored. High resolution and large acceptance spectrometer configurations will be used, based on detectors made of large NaI (Tl) crystals and multi-wire proportional planes as well as a 20 kgauss superconducting analyzing magnet.

I. INTRODUCTION

We have modified our original electron physics experimental proposal, 164-II, to include a first generation search at NAL for intermediate bosons W, Lee-Wick heavy photons B, and sequential heavy Leptons L, from e - N scattering processes. In some cases we show that this electron beam experiment is competitive with other experiments using ν_μ , μ or p beams. In other cases we demonstrate that the experiment with electron beam is unique and could provide exclusively new information.

We argue, therefore, that a first generation electron/positron beam experiment of the above type must be made at NAL for the following reasons: We believe that the fundamental tools at NAL's disposal involve beams of ν_μ , μ , ν_e and e. The situation at NAL is such that (1) the ν_e beams are necessarily of low intensity; (2) the muon beam intensity is neither optimal nor intense⁽¹⁾; (3) ν_μ beams are very wide band, a monochromatic ν_μ beam being necessarily of low intensity. Thus, this situation leaves the electron beams in the position of being the most powerful tool available. The electron beam energy provides an additional constraint in the analysis of any physics results. This argument has further significance because the essential differences between electrons and muons, as well as between ν_e and ν_μ , have not yet been discovered.

Next, we have enlarged the scope of Quantum Electrodynamics tests to include the important trident process together with the study of elastic and inelastic wide angle bremsstrahlung processes, using both incident electron and positron beams. The fact that electron and positron beams

of high energy are produced only at NAL with equal intensities is used to unique experimental advantage in sorting out contributions from several competing processes. We show that these potential tests at NAL exceed the present kinematical capabilities of e^+e^- storage rings which are now becoming operational. We argue that QED tests must be made at NAL in early generation experiments to explore the behavior of time-like and space-like propagators of leptons and photons. This argument is based on the understanding that strong interactions among hadrons at large momentum transfers are dominated by QED processes by which high Q^2 virtual photons are exchanged between the constituents of hadronic states. Therefore, large transverse momentum hadronic collision studies at NAL must rely also on the validity of these QED tests.

Finally, we emphasize the need for exploring the lepton-hadron deep inelastic kinematical region with electrons at NAL because among other reasons, the relative merit of muon experiments at NAL is also based on an electron-muon comparison of results. The electron-muon puzzle and the possibility of anomalous leptonic behavior are sufficiently fundamental interests supporting the need of studying, at the same time, both electron and muon scattering processes. The physical laws derived from these experiments are so fundamental that from past experience we can assert the need for performing both experiments. In this case different beam qualities and different detectors are involved, so that the relative comparisons will be sharp and clear. Therefore, we suggest the electron scattering experiment must be made in conjunction with the muon experiments at NAL.

As is well known, we show once more that at NAL energies, the level of radiative corrections in the electron scattering experiment is not at all different from the muon experiments. However, compared with muons, electrons have an experimental advantage which permits the design of a high quality beam. This beam is discussed in detail in Appendix I. Only with electrons is it possible to deliver a ± 2 mm spot size, free of halo, at the experimental target and also have optimized intensity. It is this small spot size quality which allows us to use an economical spectrometer design with large acceptance and without the sacrifice of energy resolution. Moreover, we have used to advantage the fact that electrons are efficient producers of real and virtual photons, by designing a spectrometer configuration which simultaneously tags the energy of these photons and detects the pair production of large angle leptons. We show that the experimental sensitivity of this method is superior to a tagged photon beam setup especially for the pair production of intermediate bosons and heavy leptons. Compared to a tagged photon experiment this method is more efficient, more compact, and more economical.

While the scope of the present experiment has been enlarged over Proposal 164, this is done efficiently and economically, using basically the same set of detectors as originally proposed. The major changes are the following:

- a) The spectrometer analyzing magnet has been redesigned to have superconducting coils at 20 kgauss. The magnet is 15 feet long and usefully 3 feet wide with a 1 foot gap. The cost of this magnet is estimated at about \$ 150 K.

- b) Several multi-wire proportional chamber planes are incorporated in spectrometer configurations, in some cases to provide also redundant information on track orbits of large angle scattered electrons or muons.
- c) Muon identifiers are added to the large NaI(Tl)/MWPC spectrometer modules, to include the efficient detection of muons together with gamma-rays and electrons.
- d) The electron beam purity is improved dramatically. We have re-examined the role of synchrotron radiation in purifying the electron beam. The beam's pion contamination is eliminated without the use of any new and costly "chicane" superconducting magnets and also without the loss of valuable electron intensity. A beam tuning method is devised which enhances synchrotron radiation throughout the beam transport systems. The radiation compensated tuning displaces pions from the small spot size of electrons, at the fourth focus. This method can work only with the high quality four stage beam design, presented in Appendix I. We estimate that this technical breakthrough, solving the electron beam purity issue, is equivalent to a real saving of about \$ 0.5 M.

In performing the experiments proposed herein, new knowledge will be acquired covering the main features of electron scattering processes at the highest possible energy and momentum transfer. This knowledge is both essential and timely in the planning and design of high energy e-p storage rings now being discussed, such as EPA, ISABELLE and PEP. The expected luminosity of such storage rings is about $10^{32} \text{ cm}^{-2} \text{ sec}^{-1}$, a figure which is equivalent to our 10^8 e/pulse on a 25 cm LH₂ target.

We emphasize that our NAL pion and electron experiments are intimately connected not only in the commonality of beams, spectrometers and other experimental facilities, but also most importantly in the physics. The scaling behavior of nucleon structure functions, so far established only from electron deep scattering experiments, is assumed to prevail in hadron-hadron deep scattering processes, both for electromagnetic or leptonic final states. At NAL, we propose to test and establish the scaling properties in pion-nucleon deep scattering processes from our pion experiment and we also propose to observe and discover any new scaling behavior in electron-nucleon deep scattering processes in our electron experiment. In both cases these experiments will be in kinematical regions which are unexplored up to the present time. Experimentally, it is by such an efficient comparison that we expect to acquire new knowledge covering the main features of the nucleon constituents.

II. EXPERIMENTAL PROGRAM

A. SEARCH EXPERIMENTS

We plan to search for the existence of intermediate vector bosons $W_1^{+,-}$, heavy sequential leptons $L^{+,-,0}$, and Lee-Wick heavy photons B^0 , produced in electron-nucleon collisions. We show that beams of up to 250 GeV electrons or positrons at NAL provide a powerful tool to investigate several very fundamental questions. For example, with 200 GeV electrons and their virtual or real photons, the total energy in the center of mass system is such that up to 18 GeV massive particles can be produced singly, or up to 9 GeV massive particles can be produced in pairs. Several production mechanisms are available in the initial $e - p$ system. Briefly, these are 1) electromagnetic pair production by virtual or real photons from primary electron interactions in a target, 2) semi-leptonic $e - p$ collisions or 3) other anomalous leptonic processes. The above mentioned elusive massive objects are postulated to have very high mass values and theoretical predictions range over at least one order of magnitude. The advantage of using ep collisions to investigate the production of these objects is that reliable theoretical cross sections can be calculated. In the case of a negative search, at least a meaningful lower limit can be set on the mass values and the coupling constants. Predominantly, the W 's and L 's can be produced in pairs (in low Q^2 electromagnetic ep collisions) or in singles (in semi-leptonic ep interactions). The B^0 or W_1^0 can be produced singly, in trident type ep electromagnetic or semi-leptonic collisions, or their presence as an exchanged particle can be observed in deep inelastic large Q^2 ep collisions.

1. Intermediate Vector Boson Search

Up until now, the search for intermediate vector bosons has been concentrated on the use of ν_μ and proton beams as probes. At NAL, even though the ν_μ carries only about one third the energy of parent pions and ν_μ beams are not monochromatic at high intensities, these beams are favored because the ν_μ has the correct helicity to induce the production of W's in:



If $M_W = 10$ GeV, at $E_\nu = 100$ GeV this reaction has $\sigma_\nu \approx 10^{-39} \text{ cm}^2$.

At NAL, muon beams carry about two third the energy of parent pions and monochromatic beams can be prepared with some sacrifice in intensity. However, these high energy muons (both μ^- and μ^+) are polarized and have the wrong helicity^(2a) to induce the production⁽²⁾ of W's by:



Independent of this severe muon polarization difficulty, there are purely kinematical effects due to the dominance of propagators in both semi-leptonic processes. Reaction (1) is favored over reaction (2)

by about two orders of magnitude difference in the production cross sections.

The advent of high energy electron beams at NAL can change drastically the above situation. New avenues are now open to carry out this important search with electrons, and we examine these individually. The advantages provided by electrons are 1) the above muon polarization difficulty is eliminated entirely because e^+ or e^- beams at NAL are unpolarized; 2) electrons are efficient producers of real and virtual photons; 3) with electrons an optimally high intensity beam can be provided.

We propose to study effects due to the semi-leptonic reactions:

$$e^+ Z \rightarrow ZW^+ \bar{\nu}_e \quad (3)$$

$$(W^+ \rightarrow e^+ \nu_e; W^+ \rightarrow \mu^+ \nu_\mu)$$

and

$$e^- Z \rightarrow ZW^- \nu_e \quad (4)$$

$$(W^- \rightarrow e^- \bar{\nu}_e; W^- \rightarrow \mu^- \bar{\nu}_\mu)$$

These electron and positron induced reactions are valuable because at NAL they are equivalent to having a ν_e and $\bar{\nu}_e$ beam for the purpose of exploring the $e \nu_e W$ vertex, and to compare this with the ν_μ beam's derived information on the $\mu \nu_\mu W$ vertex. Reaction (3) and (4) would produce leptons having anomalously large transverse momentum values. The transverse momentum spectra of final state leptons, (e^\pm, μ^\pm) would show a sharp upper cutoff, at a value corresponding to the mass M_W , at

$$P_{\perp}(e^{\pm}, \mu^{\pm}) \approx M_W/2.$$

In published calculations, the production cross section of reaction (3) or (4) is not given specifically. We take these to have the same values⁽²⁾ as the cross sections for reaction (2), without the detrimental muon polarization factor; although slightly larger cross sections should be expected for electrons than for muons. At NAL, if we compare the cross sections of reaction (1) for 70 GeV with the cross sections of reaction (3) for 200 GeV (as we should) we find that the electron induced reaction is of about the same order of magnitude as the neutrino reaction. In fact, it is instructive to compare the ratio

$$R(M_W) = \sigma_{\nu}(70 \text{ GeV})/\sigma_e(200 \text{ GeV}).$$

For $M_W = 5 \text{ GeV}$, $R = 11$, at $M_W = 8 \text{ GeV}$, $R = 2.2$, but when

$$M_W = 10 \text{ GeV} \quad R = 5.25 \times 10^{-3}.$$

Therefore, the electron beam experiment at NAL is potentially a more powerful method of searching for W's, especially if the mass of the intermediate vector boson is greater than 8 GeV.

The semi-leptonic reaction:



is especially interesting because the dominant mechanism in this case is actually the photoproduction of W's without the emission of neutrinos. In Fig. 1(a) the expected behavior of this cross section is displayed⁽³⁾. The electrons provide virtual photons to produce W's. From hard radiation in our experimental target, high energy real photons are also provided, so that these cross sections are further enhanced (but must be distinguished). Other calculations based on the quark-parton model⁽⁴⁾

give a cross section of 6×10^{36} cm² for $M_W = 10$ GeV and $E_\gamma = 200$ GeV in the reaction:

$$\gamma N \rightarrow W^+ + \text{hadrons} \quad (6)$$

Similarly, a calculation based on the target fragmentation model⁽⁵⁾ yields a cross section of 3.5×10^{-33} cm² with the above parameters where nucleon magnetic moment coupling is also included. These calculations are not altogether definitive because of unknown weak form factors both in space-like and time-like regions.

Another attractive reaction is one which produces W's at a hadronic vertex as a result of semi-weak interactions in the process:

$$\text{and} \quad \left. \begin{array}{l} e^- p \rightarrow e^- n W^+ \\ e^- n \rightarrow e^- p W^- \end{array} \right\} \quad (7)$$

The cross section of these processes is estimated⁽⁶⁾ to be 2×10^{-35} cm², for $M_W = 10$ GeV and $E_e = 200$ GeV. We consider reactions (7) as valuable sources of new information because these can be compared directly with semi-weak hadronic collisions:

$$\pi^- N \rightarrow W^+ + \text{hadrons} \quad (8)$$

We discuss details of reaction (8) in our associated pion experiment proposal.

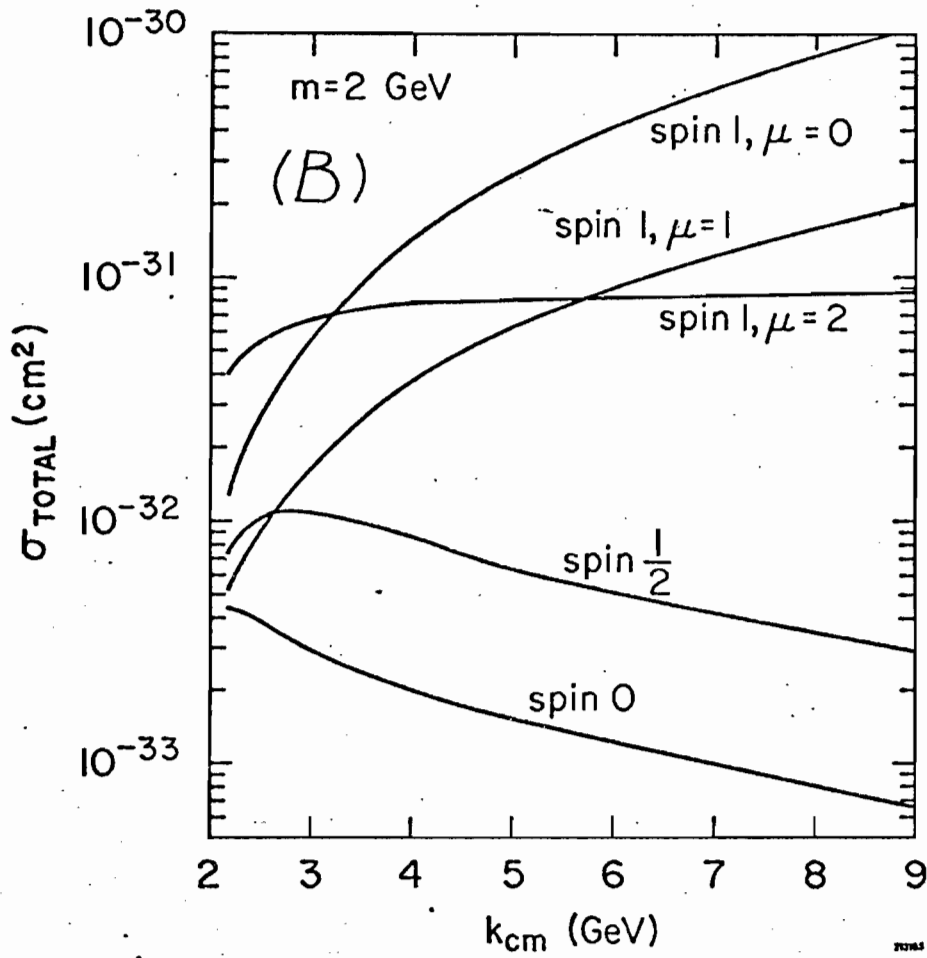
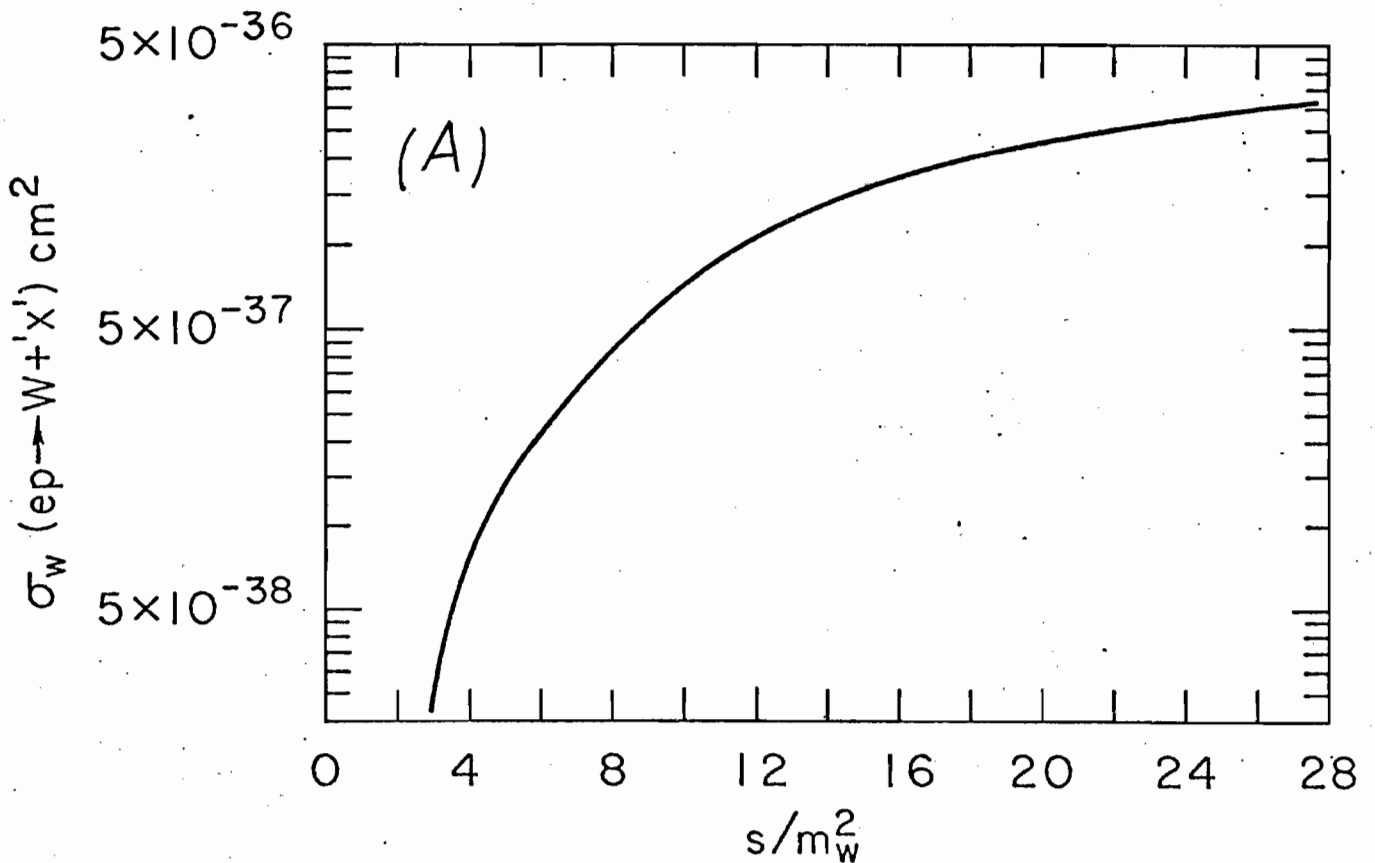


Figure 1



--Total intermediate vector meson (W) production cross section in lepton-hadron collisions.

We propose to look for the pair production of W's by virtual or real photons, in the two step interaction of:

$$\begin{array}{l}
 e^- N \rightarrow e^- W^+ W^- \text{ hadrons} \\
 \text{where } e \rightarrow e' \gamma^* \\
 \gamma^* N \rightarrow W^+ W^- \text{ hadrons}
 \end{array}
 \quad \left. \vphantom{\begin{array}{l} e^- N \rightarrow e^- W^+ W^- \text{ hadrons} \\ e \rightarrow e' \gamma^* \\ \gamma^* N \rightarrow W^+ W^- \text{ hadrons} \end{array}} \right\} \quad (9)$$

Small angle and low energy scattered electrons (low Q^2 and high $v = E - E' \cong k_\gamma$) will be observed in coincidence with the production of large angle asymmetric and uncorrelated leptons. These leptons will have a large transverse momentum imbalance due to the unobserved neutrinos in the decays of $W \rightarrow l + \nu$. The transverse momentum spectra of large angle electrons and muons will be examined in singles and in pairs, to search for confirmation that in such samples the large angle leptons are indeed uncorrelated. The search for any heavy object by the pair production mechanism is very useful because of two important reasons. First, the electromagnetic pair production process is well understood and provides reliable calculations of cross sections. To be able to set significant mass limits in any search experiment a well defined production cross section is required, so that the level of experimental sensitivity can be determined. Second, the pair production of intermediate bosons and heavy leptons is particularly valuable because observation of the reaction's energy dependence provides immediately information on the spin and magnetic moment of pair produced particles⁽⁷⁾. This fact is well demonstrated⁽⁷⁾ in Fig. 1(b).

Because electrons are efficient producers of real and virtual photons, at NAL and for the pair production of heavy particles, we demonstrate the value of using electrons directly on an experimental target. Higher pair production event rates are obtained with electrons than in the case of first preparing a tagged photon beam and then using these tagged photons on an experimental target. Also a more compact and economical experimental arrangement in the electron case is used.

Note that real photons are produced by electrons at a radiator by the bremsstrahlung process $\sim Z_R^2 \alpha^3$. Subsequently, tagged photons pair produce massive particles M_W , on an experimental target Z_T , by the pair production process $\sim Z_T^2 \alpha^3 / M_W^2$.

Hence, the overall probability of this two step process is

$$\sim Z_R^2 \cdot Z_T^2 \cdot \alpha^6 / M_W^2 . \quad \text{Whereas, the pair production by}$$

low Q^2 virtual photons using an electron beam on the experimental target is $\sim Z_T^2 \alpha^4 / M_W^2$. In the case of tagged photon beams the en-

hancement factor is not really proportional to Z_R^2 because in all cases, the tagged photon producing Pb radiator must be about 1% of a radiation length; otherwise the tagging counters would be confused. Thus, the enhancement factor, for fixed unit of a radiation length, is given by

$$Z_R^2 \rho L/A. \quad \text{Between Pb and LH}_2 \text{ radiators the factor is } 3.275 \text{ and not } (82)^2. \text{ We use the above } \alpha^2 \text{ difference in the rates to assert that}$$

the pair production of heavy leptons and intermediate bosons is detected more efficiently and economically by using electrons directly on a 25 cm LH_2 target, rather than using tagged photon beams for this purpose.

Electron beams provide a finer experimental sensitivity and have the added advantage of studying at the same time, the pair production of heavy particles and the single production of these particles in other semi-leptonic processes. Tagged photon beams can only be useful in pair production

because semi-leptonic processes, to lowest order, are not initiated by real photons.

At NAL, for the pair production of heavy objects, only the wide-band photon beam can provide higher experimental sensitivity than our method. However, that method suffers from the lack of providing an additional constraint which is available to us. In our case, the photon energy is known, both for real and virtual photons.

In Fig. 2 the result of our photon flux calculations⁽⁸⁾ is shown, as a function of photon energies, for the case of low Q^2 virtual photons and hard radiated real photons from a 25 cm LH_2 target.

2. Heavy Lepton Search

Several categories of heavy leptons are postulated. Some of the popular varieties are the following:

- a) Heavy Sequential Leptons - here each new lepton has its own lepton number and correspondingly a new neutrino must also exist; typical decay mode of interest to us are these:

$$\begin{aligned} L^- &\rightarrow e^- \bar{\nu}_L \bar{\nu}_e; \quad \mu^- \bar{\nu}_L \bar{\nu}_\mu \\ L^+ &\rightarrow e^+ \bar{\nu}_L \nu_e; \quad \mu^+ \bar{\nu}_L \nu_\mu \end{aligned} \tag{10}$$

- b) Heavy Excited Leptons - these are postulated massive states of electrons and muons and radiatively decay to the usual lepton ground states. They carry the same lepton number as their ground state and by definition, no new corresponding neutrino is required to exist; we propose to search for the decay modes:

$$\text{and } \left. \begin{aligned} E_+^* &\rightarrow e^+ \gamma \\ E_-^* &\rightarrow e^- \gamma \end{aligned} \right\} \tag{11}$$

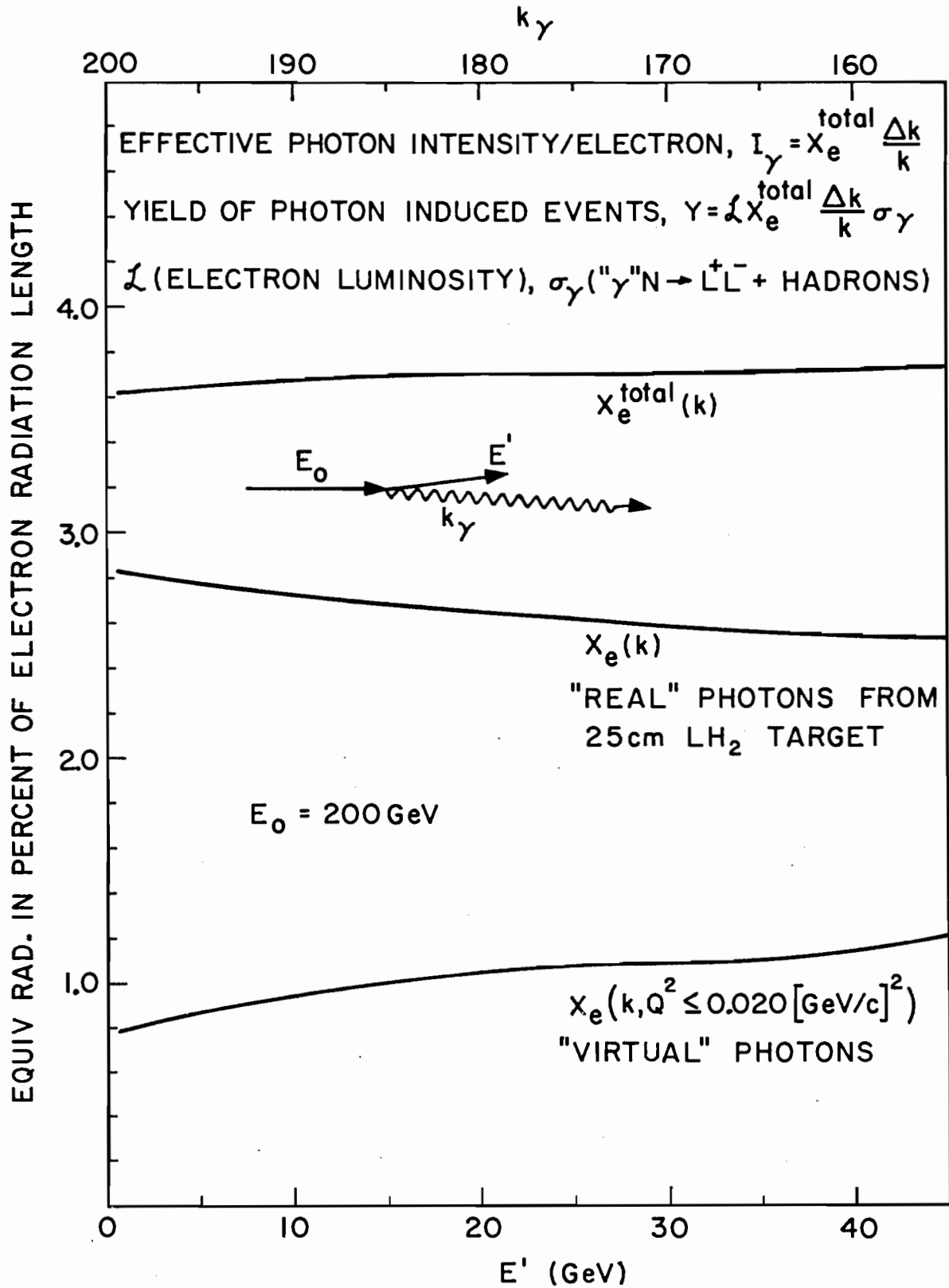


Figure 2

The proposed search for heavy excited leptons is discussed subsequently together with our QED tests and the wide angle bremsstrahlung process.

c) Heavy Leptons - renormalizable theories of weak interactions almost invariably require a set of spin 1/2 fermions E^+ and E^0 , M^+ and M^0 , with the same lepton number assignments as the familiar set (e, ν_e) and (μ, ν_μ) .

Specifically, we propose to search for the following heavy leptons in these decay modes:

$$E^0 \rightarrow e^+ \mu^- \bar{\nu}_\mu ; e^+ e^- \bar{\nu}_e ; e^+ + \text{hadrons} \quad (12)$$

and

$$\bar{E}^0 \rightarrow e^- \mu^+ \nu_\mu ; e^- e^+ \nu_e ; e^- + \text{hadrons} \quad (13)$$

We do not dwell long on previous search attempts for all categories of heavy leptons. These are described in recent excellent reviews⁽¹⁰⁾. Suffice it to say that heavy leptons have not yet been discovered. Consequently, there appear to be 66 renormalizable theoretical models⁽¹¹⁾ of weak and electromagnetic interactions where hopefully, only one of these may describe the real world. Clearly, this proliferation can only be resolved by the necessary input of high energy experiments which are done exclusively with electrons, neutrinos and muons. In experiments with beams, in each case, a unique and exclusive set of new pieces of information can be made available. For example, only the following beams can produce singly the associated heavy leptons:

$$e^+ \rightarrow E^0$$

$$e^- \rightarrow \overline{E^0}$$

$$\mu^+ \rightarrow M^0$$

$$\mu^- \rightarrow \overline{M^0}$$

$$\nu_\mu \rightarrow M^+$$

$$\bar{\nu}_\mu \rightarrow M^-$$

$$\nu_e \rightarrow E^+$$

$$\bar{\nu}_e \rightarrow E^-$$

These are produced as in the following reactions:

$$\mu^+ + N \rightarrow M^0 + \text{hadrons} \quad (14)$$

$$\left[\begin{array}{l} \mu^+ \mu^- \bar{\nu}_\mu \\ \mu^+ e^- \bar{\nu}_e \\ \mu^+ + \text{hadrons} \end{array} \right.$$

$$e^+ + N \rightarrow E^0 + \text{hadrons} \quad (15)$$

$$\left[\begin{array}{l} e^+ \mu^- \bar{\nu}_\mu \\ e^+ e^- \bar{\nu}_e \\ e^+ + \text{hadrons} \end{array} \right.$$

$$\nu_\mu + N \rightarrow M^+ + \text{hadrons} \quad (16)$$

$$\left[\begin{array}{l} \nu_\mu \nu_\mu \mu^+ \\ \nu_\mu \nu_e e^+ \\ \nu_\mu \text{ hadrons} \end{array} \right.$$

Among these beams the value of experiments with electrons and positrons is outstanding. This is because of the fact that only with electrons is it possible to observe, at the same time, the pair production of all heavy leptons and the semi-leptonic single production of those heavy leptons which have electron-like leptonic numbers.

In Table I the partial decay rates of heavy sequential leptons is given from a recent calculation^(7d). The branching ratio of heavy leptons is shown in Fig. 3 from another theoretical calculation⁽¹¹⁾. In both cases the leptonic decay modes into electrons and muons are dominant, provided that the mass of heavy leptons is less than the mass of intermediate bosons.

We propose to search for the semi-leptonic production of single heavy leptons E^0 and $\overline{E^0}$ in the following reactions and decay modes:

E^0 production by e^+ as in reaction (15)

and

$$e^- + N \rightarrow \overline{E^0} + \text{hadrons}$$

$$\left[\begin{array}{l} e^- + \nu_\mu \\ e^- + \nu_e \\ e^- + \text{hadrons} \end{array} \right. \quad (17)$$

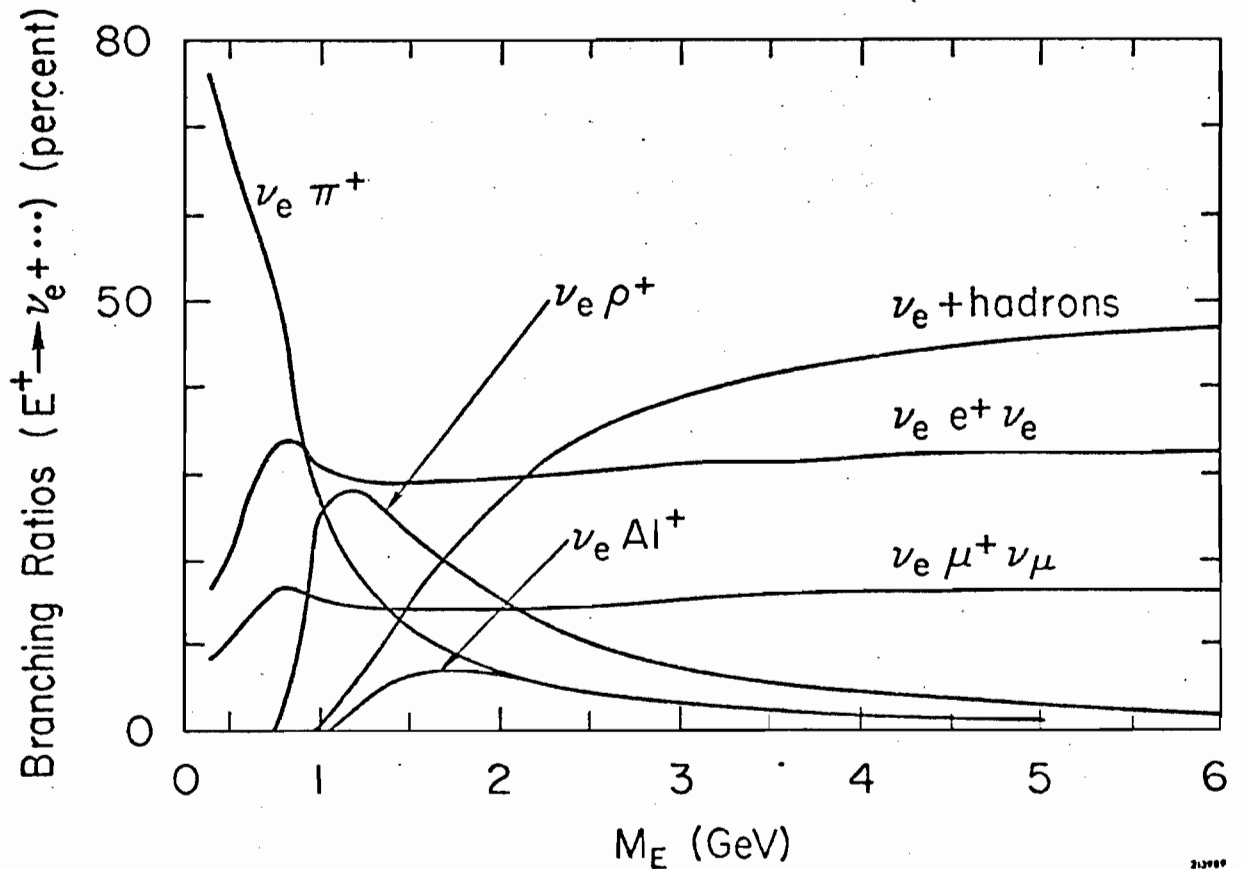
The transverse momentum spectra of large angle leptons, in pairs and in singles, will be examined to search for structure. The most useful combination is found in the pairs of $(e^- \mu^+)$ and $(e^+ \mu^-)$ from reactions (17) and (15). The transverse momentum distribution of these correlated pairs

TABLE I

Partial and total decay rates of l for various values of M_1 . Decay rate (10^{10} sec^{-1}) = $(\Gamma/\hbar) = 1/\tau$.

M_1 (GeV)	0.6	0.8	0.938	1.2	1.8	3.0	6.0
Decay mode							
$l \rightarrow \nu_l + \nu_e + e$	0.266	1.12	2.46	8.5	64.6	831	26 600
$\nu_l + \nu_\mu + \mu$	0.2	0.96	2.21	7.97	63	823	26 533
$\tau + \nu_l$	1.02	2.57	4.17	9.0	30	143	1145
$K + \nu_l$	0.0092	0.09	0.2	0.55	2.3	11.7	98
$\rho + \nu_l$	0	0.21	3.8	19	96	486	3900
$K^* + \nu_l$	0	0	0.03	0.96	6.3	33	280
$A_1 + \nu_l$	0	0	0	0.6	33.7	364	1550
$Q + \nu_l$	0	0	0	0	0.17	15.2	133
$\nu_l + \text{hadron continuum}$	0	0	0	0.5	27	737	25 900
$l \rightarrow \nu + \text{hadrons}$	1.03	2.87	8.2	29.6	195	1790	33 006
Total rate	1.5	4.95	12.9	46.1	323	3444	85 539
Decay length in cm at $E_l = 5$ GeV	16.5	3.73	1.2	0.26	0.024
Decay length in cm at $E_l = 50$ GeV	167	37.7	12.2	2.7	0.257	0.0145	...

2130A4



should exhibit a sharp peak, corresponding to the mass value of heavy leptons M_E , at $p_{\perp}(e^{\pm} \mu^{\mp}) \approx M_E/2$. In one theoretical evaluation, the production cross section of heavy leptons in reactions (15) and (17) is estimated⁽¹¹⁾ to be between 10^{-35} cm^2 and 10^{-37} cm^2 .

All categories of heavy leptons can be pair produced by the well known electromagnetic interaction. Compared with a wide-band photon beam experiment proposed at NAL (E-87A), the basic advantage of our method is the fact that the energy of real or virtual photons, initiating the pair production process, is well defined. Therefore, the important mass correlation with photon energies can only be made by our proposed method. We propose to search for the pair production of heavy leptons in the two step electromagnetic process, using high energy electron beams directly on our experimental targets:

$$\left. \begin{array}{l} e N \rightarrow e L^+ L^- + \text{hadrons} \\ \left(\begin{array}{l} e \rightarrow e' \gamma^* \\ \gamma^* N \rightarrow L^+ L^- + \text{hadrons} \end{array} \right) \end{array} \right\} \quad (18)$$

$$L^{\pm} \rightarrow \left[\begin{array}{l} \mu^{\pm} \nu_{\ell} \nu_{\mu} \\ e^{\pm} \nu_{\ell} \nu_e \end{array} \right]$$

Large angle electrons and muons will be observed in coincidence with scattered electrons which yield low Q^2 and high ν kinematical parameters.

Structure will be searched for in the transverse momentum spectra of single leptons, after verifying that the lepton pairs are not correlated in such a sample of events. A diagram of the pair production process of heavy leptons is shown in Fig. 4 and the cross sections for this process are listed in the associated Table II. These are obtained from a recent precise theoretical calculation^(7b).

A clear and valuable signature of this process is derived by observing the energy dependence of the pair production measured cross section, for a fixed value of the heavy lepton mass. This dependence is seen in Fig. 5(b), as obtained from an exact calculation. Fig. 5(a) displays the expected lifetime of heavy sequential leptons as a function of their mass values. Both of these figures are from a recent review^(10a).

The search for Lee-Wick heavy photons B^0 , will be discussed in the following sections on deep inelastic e-p scattering and the QED tests with the trident process.

B. ELECTRON DEEP INELASTIC SCATTERING

In this section we bring our original NAL proposal 164-II up-to-date and include our new ideas and calculations which are related to electron-nucleon deep inelastic scattering collisions. This process contains one of the most fundamental pieces of information in physics. Potentially it can answer best the questions connected with the constituent nature of nucleons, especially when experiments are made with deep scattered electrons, in coincidence with multi-gamma-ray final states. This information is contained in the behavior of the nucleon structure functions, $W_1(Q^2, \nu)$ and $\nu W_2(Q^2, \nu)$, obtained from electron-proton and electron-neutron deep inelastic scattering cross sections.

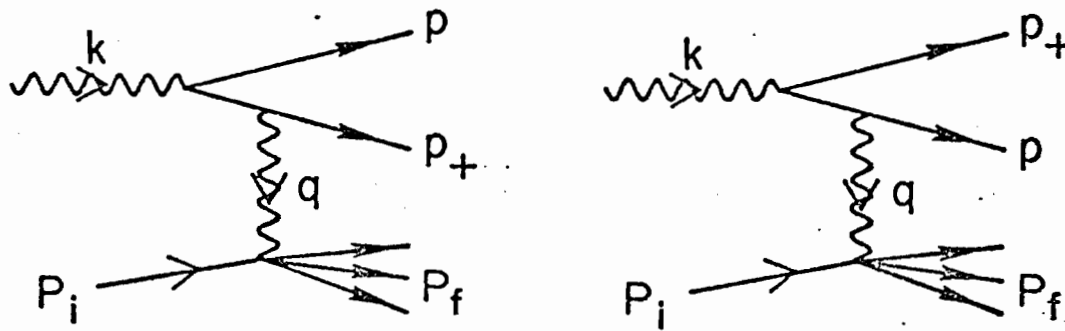


Figure 4

Table II

2055A1

Total Heavy Lepton Production Cross Section

GeV k	Be Coherent	Proton Elastic	Neutron Elastic	Be-Quasi- Elastic	Proton Inelastic	Be Total
m = 0.105	10^{-30}	10^{-31}	10^{-33}	10^{-31}	10^{-33}	10^{-30}
20	1.611	1.267	1.546	1.081	6.114	1.774
40	2.047	1.551	1.557	1.134	6.336	2.238
100	2.579	1.926	1.563	1.171	6.044	2.750
200	2.787	2.177	1.565	1.184	5.683	2.956
m = 0.5	10^{-32}	10^{-33}	10^{-34}	10^{-33}	10^{-34}	10^{-32}
20	0.902	1.607	1.342	4.443	3.559	1.666
40	1.913	2.604	1.536	5.895	5.355	2.984
100	3.784	4.122	1.672	7.324	6.846	5.133
200	5.487	5.352	1.717	8.034	7.161	6.934
m = 1.0	10^{-33}	10^{-34}	10^{-35}	10^{-33}	10^{-34}	10^{-33}
20	0.170	0.923	1.958	0.410	0.288	0.839
40	0.797	2.293	3.070	0.814	0.728	2.266
100	3.014	5.063	4.014	1.358	1.343	5.578
200	5.857	7.698	4.442	1.703	1.664	9.057
m = 2.0	10^{-34}	10^{-35}	10^{-36}	10^{-34}	10^{-35}	10^{-34}
40	0.053	0.634	2.085	0.350	0.234	0.614
100	0.764	3.404	6.293	1.420	1.290	3.345
200	2.963	7.396	8.781	2.472	2.353	7.553
m = 4.0	10^{-36}	10^{-36}	10^{-37}	10^{-35}	10^{-36}	10^{-35}
100	0.243	0.371	1.498	0.223	0.140	0.374
200	2.856	2.758	7.990	1.432	1.131	2.735
m = 6.0	10^{-38}	10^{-38}	10^{-38}	10^{-37}	10^{-38}	10^{-36}
100	0.376	0.006	0.003	0.004	0	0
200	6.932	9.975	4.178	6.079	3.826	1.021

2130A5

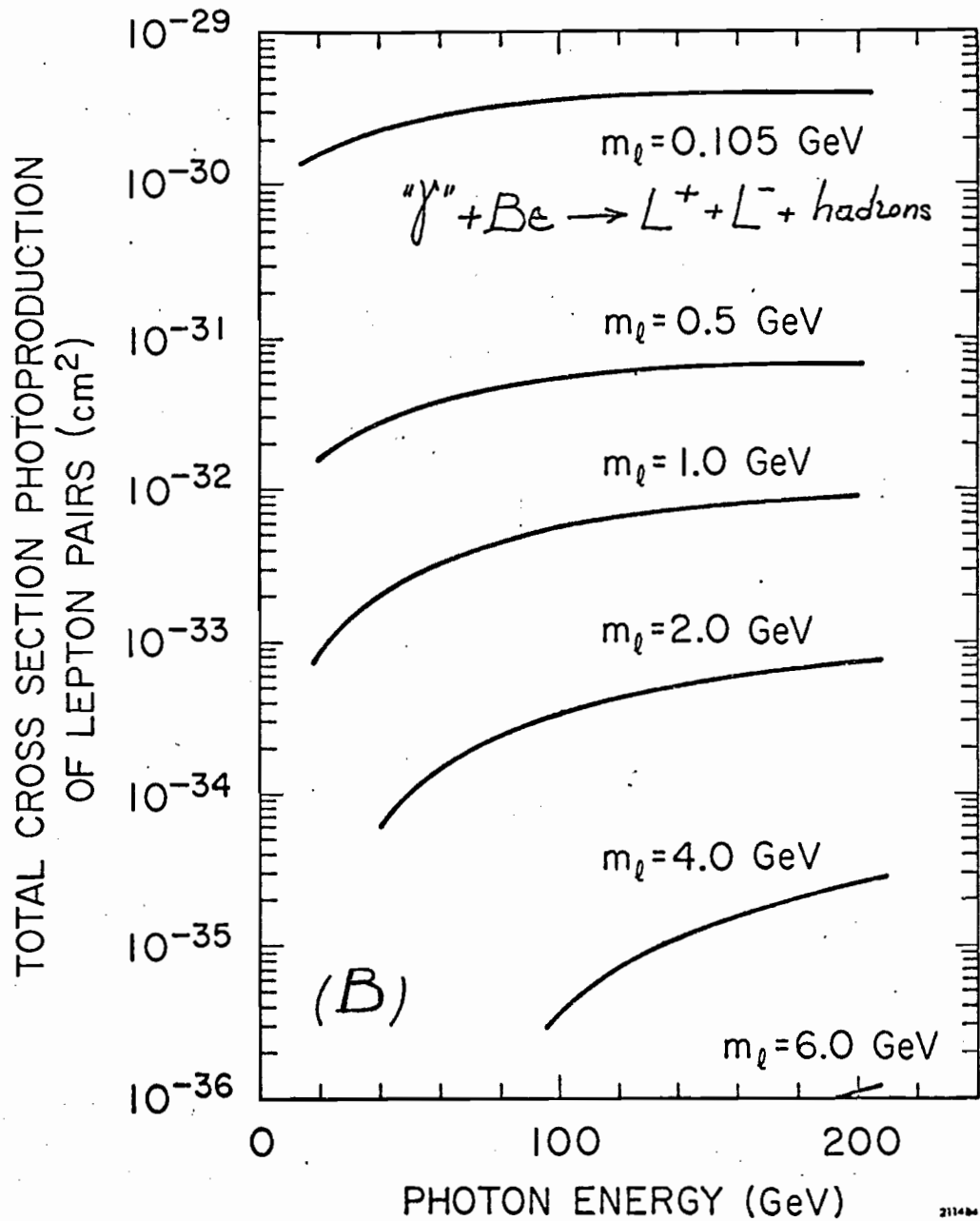
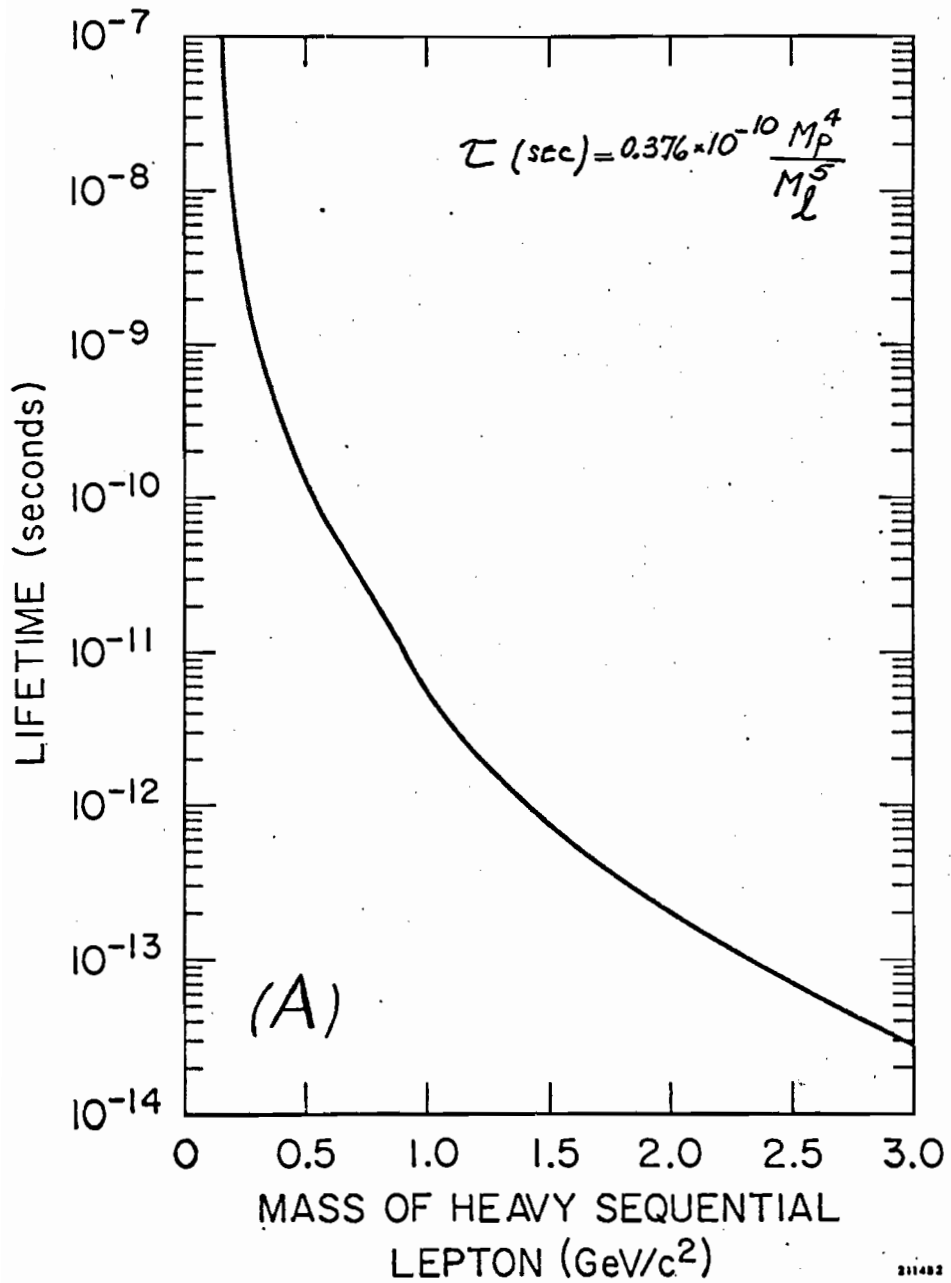


Figure 5

Some of the fundamental questions facing us at this time are the following: a) Does the scaling behavior, in terms of $x = Q^2 / 2M\nu$ continue to apply for these functions when the nucleon is probed deeper in the scattering region? Could there be a gradual breakdown of scaling due to the exchange of heavy photons or other anomalous QED behavior? b) Where are the quasi-elastic scattering peaks due to scattering off of the nucleon constituents? c) Could these peaks be revealed when we scatter high Q^2 photons on nucleons and observe physical gamma-rays in coincidence with scattered electrons? d) Could the electron-muon puzzle be resolved in the deep scattering region? At NAL these are some of the questions which we expect to approach experimentally.

In Fig. 6 the present knowledge of the proton structure function is displayed. This figure is obtained from the proposal of a recently approved project, the RLA⁽¹²⁾. At NAL we plan to probe deeper in the nucleon structure functions than is possible elsewhere. Corresponding to the scale of this figure, we demonstrate that the W^2 range of our experiment will extend to $441 (\text{GeV})^2$, whereas $81 (\text{GeV})^2$ will be available at the RLA. We believe, complementary physics information from both areas should become available. While the main features of the very deep scattering regions are explored by our high energy electron experiment at NAL, the high electron beam intensity of the RLA could be used to study more rarely occurring phenomena.

Our large acceptance and high resolution spectrometers system will be used to observe structure in the deep inelastic eN cross sections, as a function of W^2 and Q^2 . The behavior of the nucleon structure functions $\nu W_2(x)$ and $W_1(x)$ will be studied, especially in the region of large x . Accurate knowledge of the behavior in this region is essential

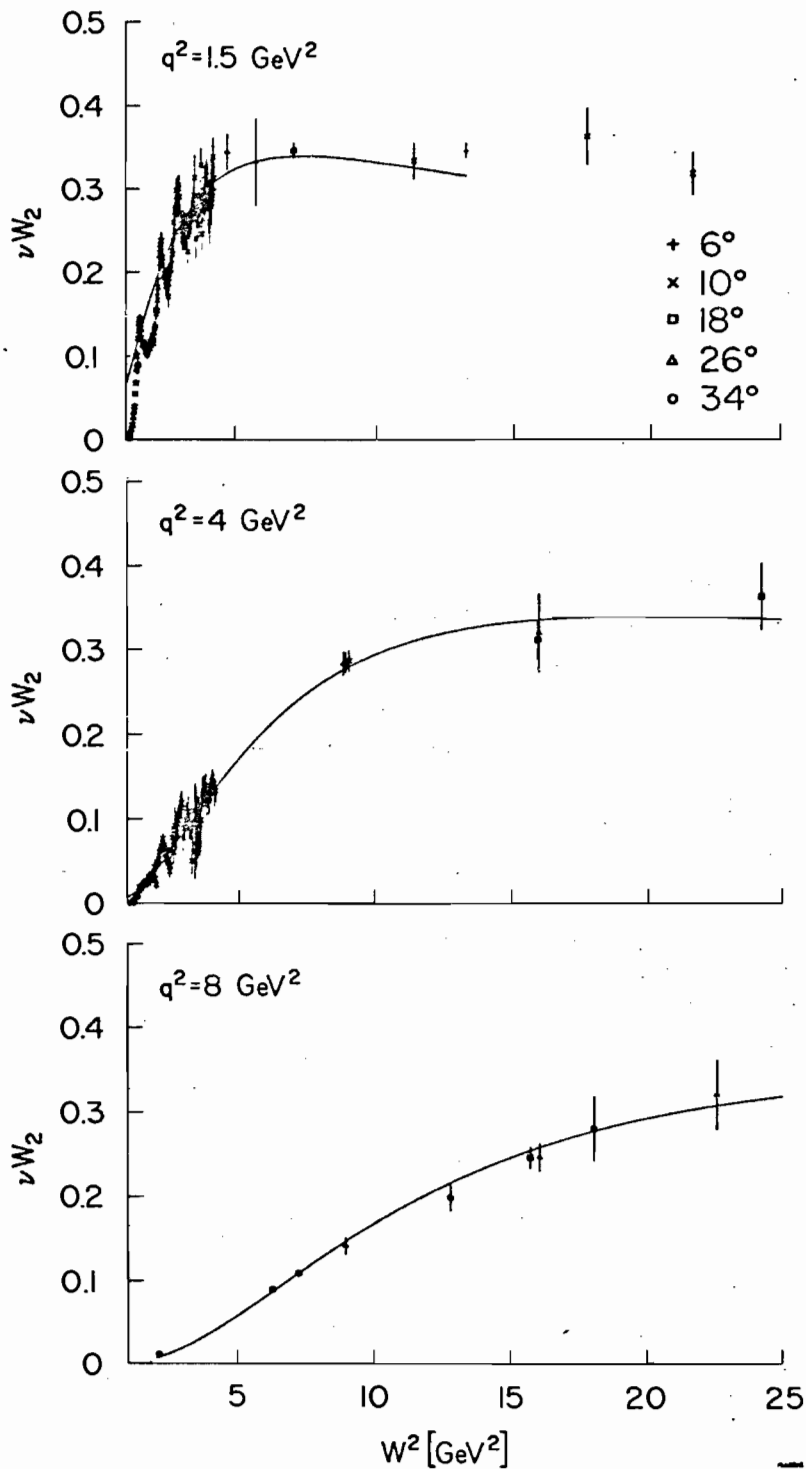


Figure 6

--Structure function of the proton from SLAC inelastic electron-proton scattering data. The horizontal scale is the square of the mass of the final hadron state $W^2 = M_p^2 + 2M_p\nu - q^2$. The laboratory cross section, in terms of the structure functions $W_1(\nu, q^2)$ and $W_2(\nu, q^2)$ and the electron scattering angle θ , is

$$\frac{d\sigma}{d\Omega dE'} = \frac{\alpha^2}{4E^2} \frac{\cos^2 \theta/2}{\cos^4 \theta/2} (W_2 + 2 \tan^2 \theta/2 W_1).$$

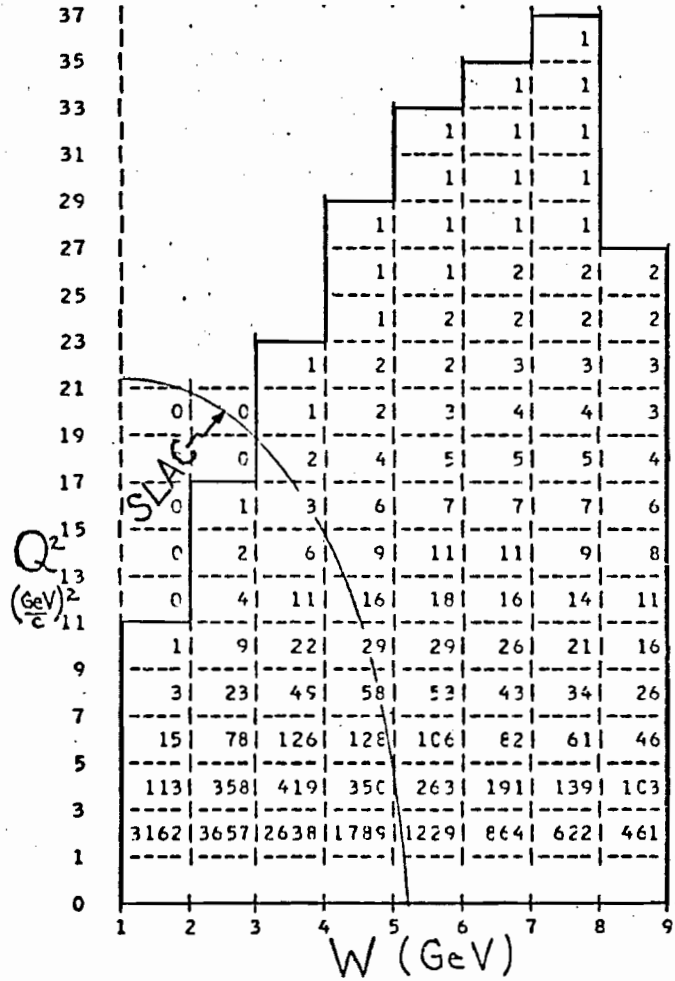
to the understanding of experiments on hadron-hadron deep scattering processes⁽¹³⁾ at NAL, because electromagnetic and semi-weak interactions are involved.

Our spectrometer configuration can be used at NAL to explore a scattering region which is sensitive to questions related to the "size" of virtual photons. This region is defined by a condition⁽¹⁴⁾ $\nu \gtrsim 3 + 5Q^2$, by which Q^2 is large (the virtual photon size is small) and also the scattering could proceed through a diffraction mechanism. That is, a kinematical region is defined where 1) the virtual photon could develop hadronic constituents prior to its interaction with the target nucleon and 2) the hadronic virtual states of such photons are so long-lived that their time development is negligible, while the states are within the interaction range of target nucleons. We indicate the kinematical region defined by this condition in following figures.

1. Deep Inelastic e-N Scattering Event Rates at NAL

We have calculated the event rates of deep inelastic electron-nucleon collisions at NAL energies. The calculations are made in the (Q^2, W) kinematical space, for electron beam energies between 50 GeV and 250 GeV. Differential cross sections are computed, based on empirical parametrizations⁽¹⁵⁾ of the nucleon structure functions $\nu W_2(x)$ and $W_1(x)$. These are obtained from fits to recent SLAC measurements. Numerical integrations are made within the boundaries of each cell $(\Delta Q^2, \Delta W)$. The number of events in each cell is obtained by converting integrated cross sections with the following experimental assumptions: 1) a 25 cm long LH₂ target will be used with 2) an electron beam intensity of 10^8 e/pulse and 3) an accelerator pulse repetition rate of 1 pulse/4 sec would be available. Typically, a luminosity of 100

DEEP INELASTIC ELECTRON SCATTERING EVENTS/HOUR AT NAL,
IN PROPOSAL 164. ELECTRON BEAM = 50.0 GEV.



3295 4131 3277 2356 1733 1260 926 692

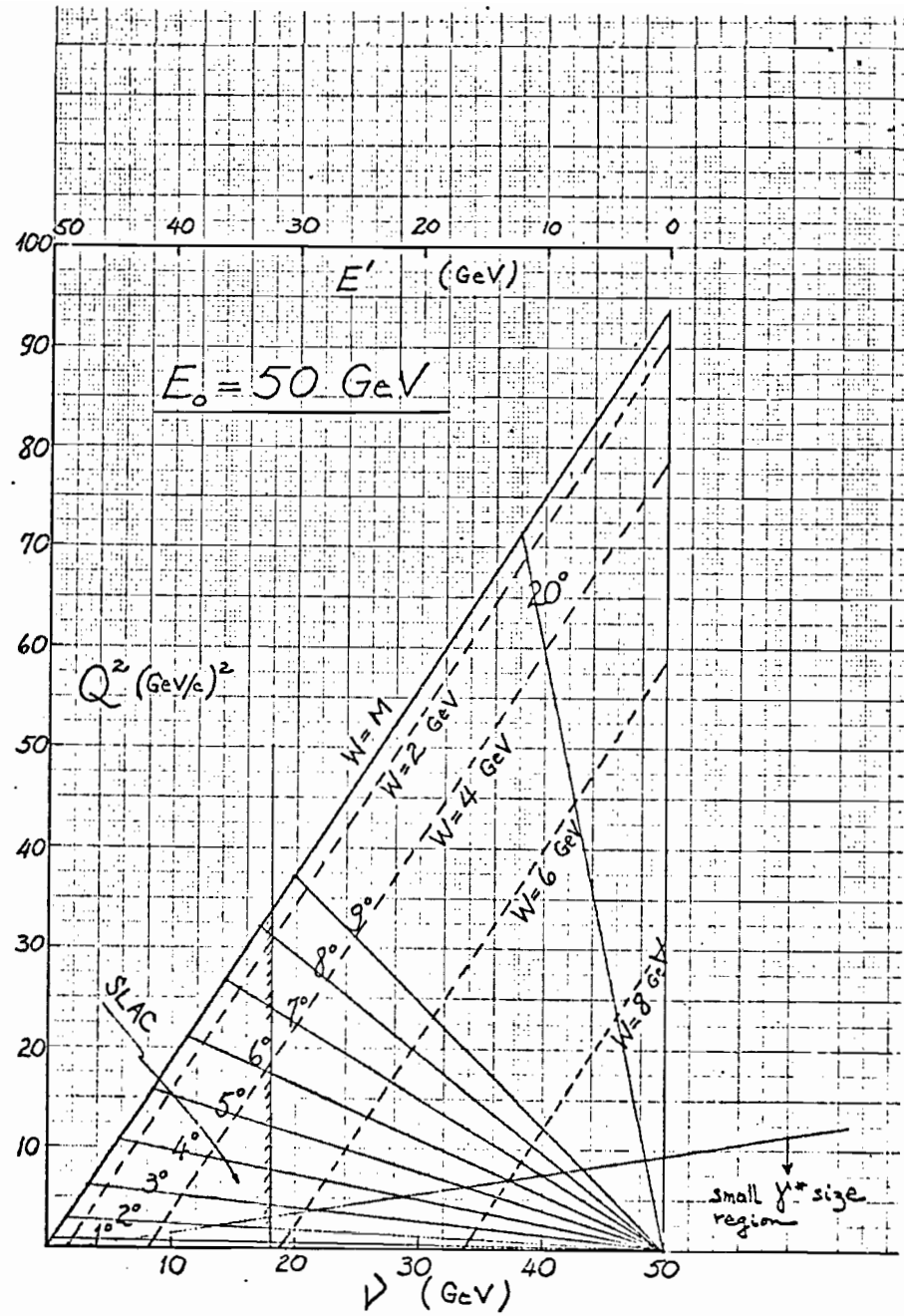
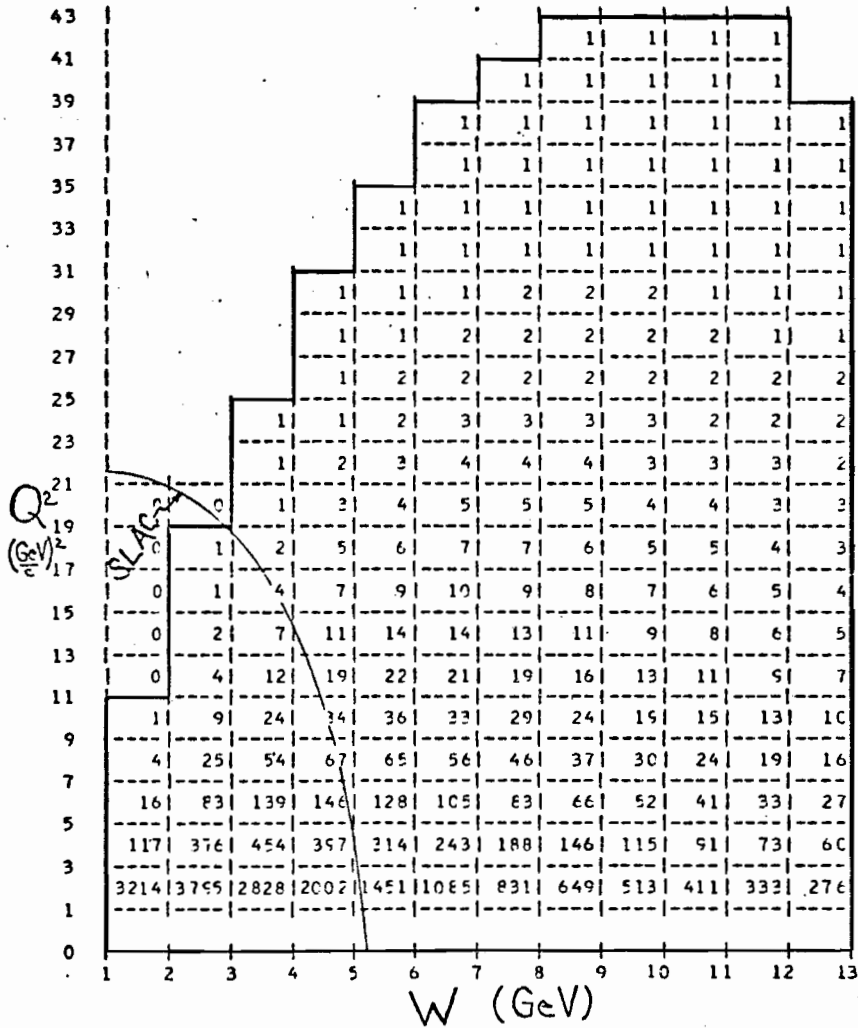


Figure 7

DEEP INELASTIC ELECTRON SCATTERING EVENTS/HOUR AT NAL.
IN PROPOSAL 164. ELECTRON BEAM = 100.0 GeV.



3351 4257 3527 2658 2062 1555 1248 566 785 631 513 423

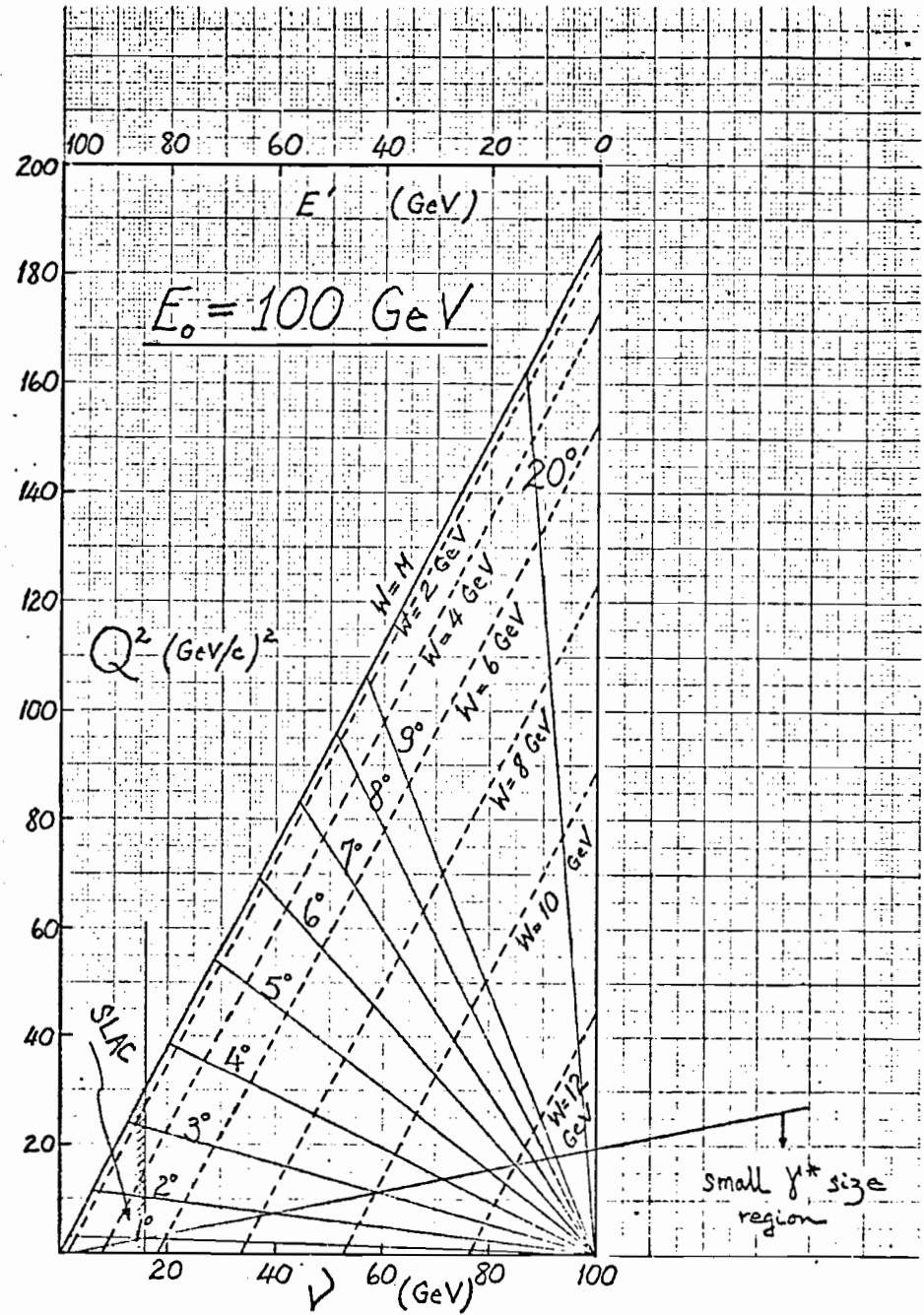
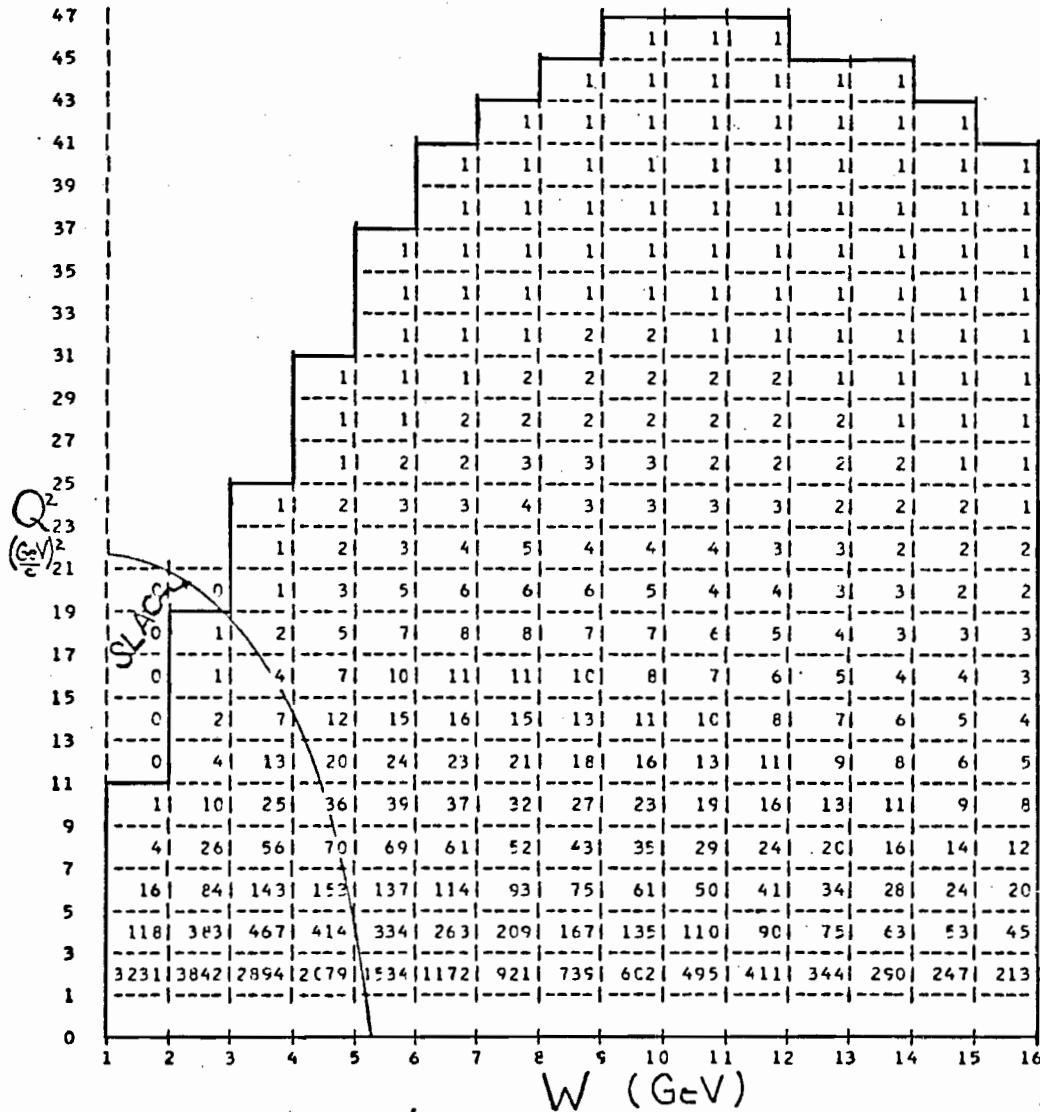


Figure 8

DEEP INELASTIC ELECTRON SCATTERING EVENTS/HOUR AT NAL,
IN PROPOSAL 164. ELECTRON BEAM = 150.0 GEV.



3370 4353 3614 2806 2186 1729 1387 1127 924 763 634 530 446 379 326

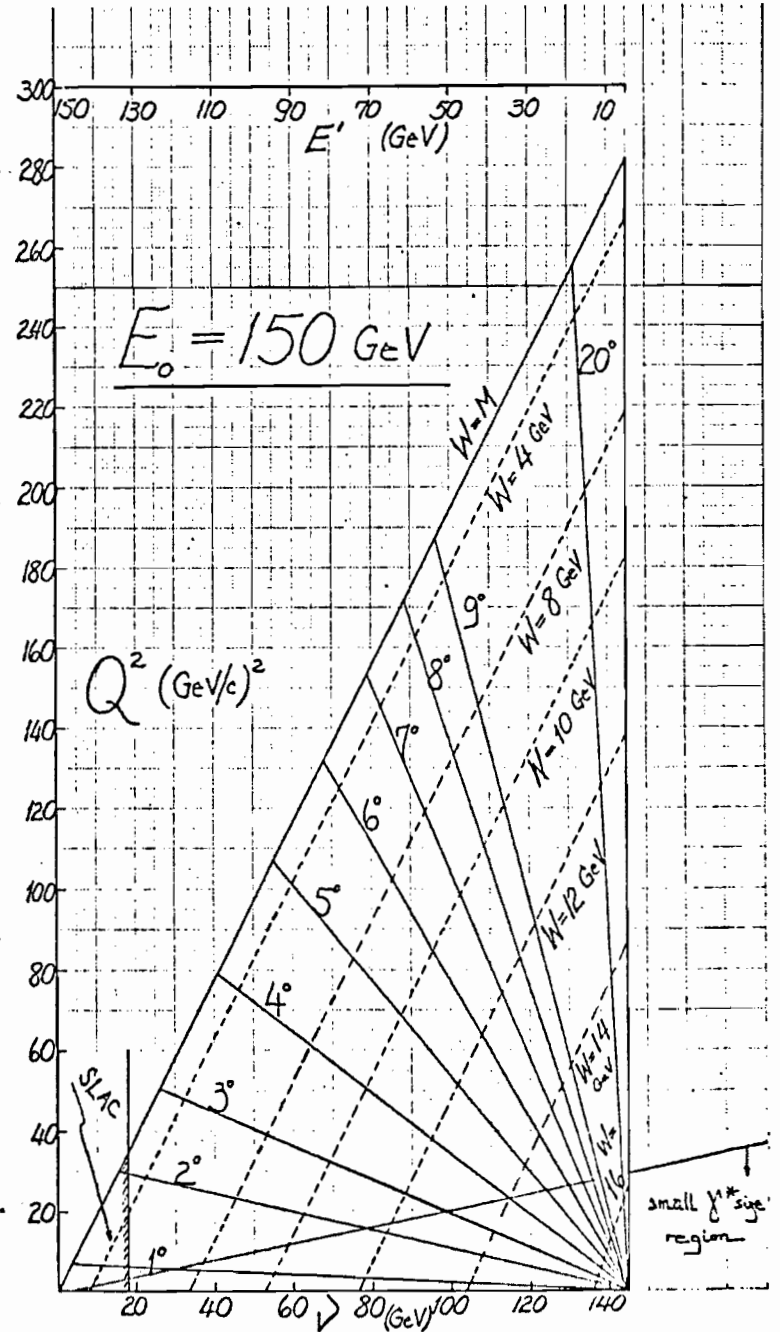
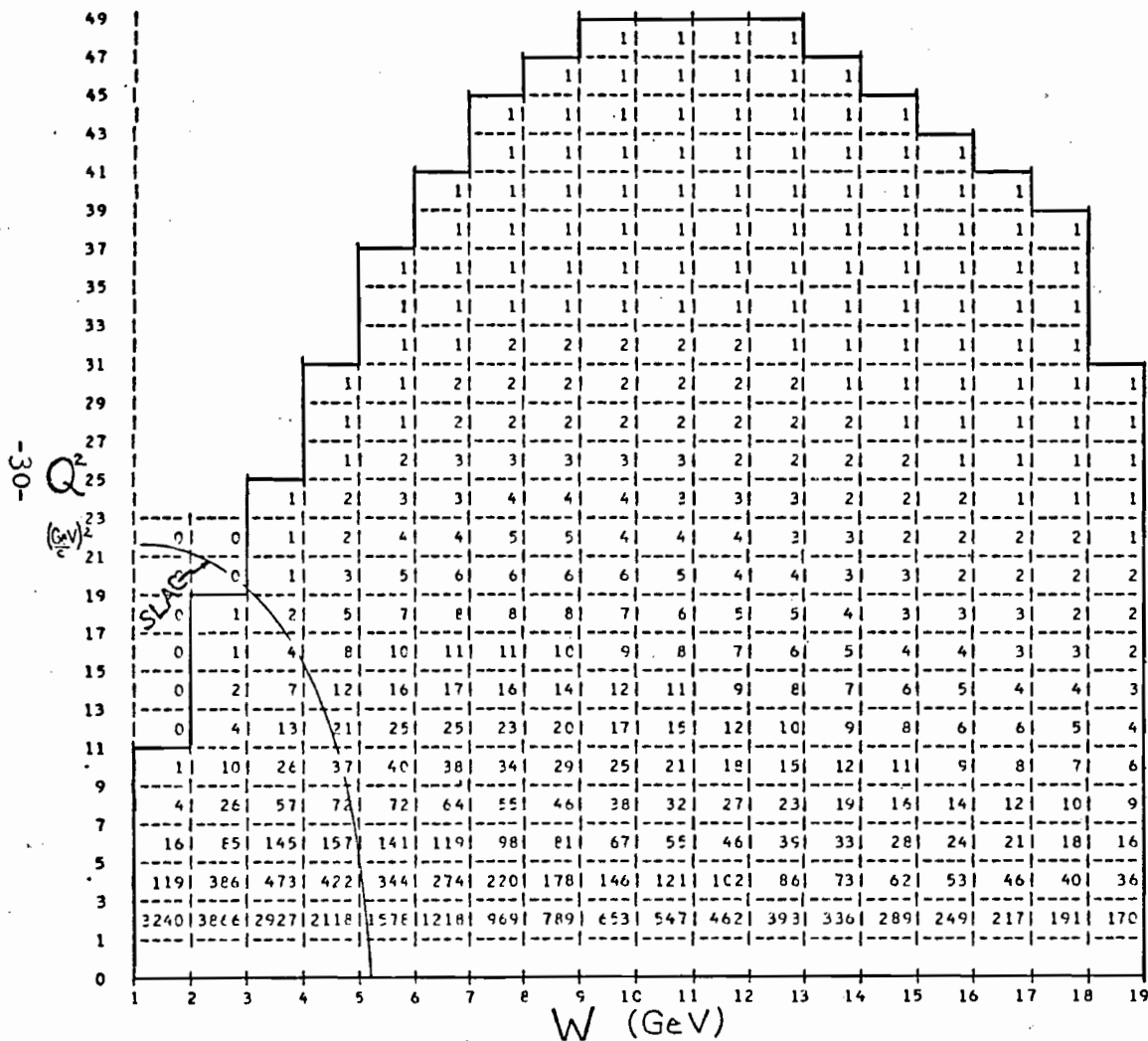


Figure 9

DEEP INELASTIC ELECTRON SCATTERING EVENTS/HOUR AT NAL,
IN PROPOSAL 164. ELECTRON BEAM = 200.0 GeV.



3380 4362 3658 2862 2250 1800 1464 1206 1005 845 714 607 518 444 382 331 290 255

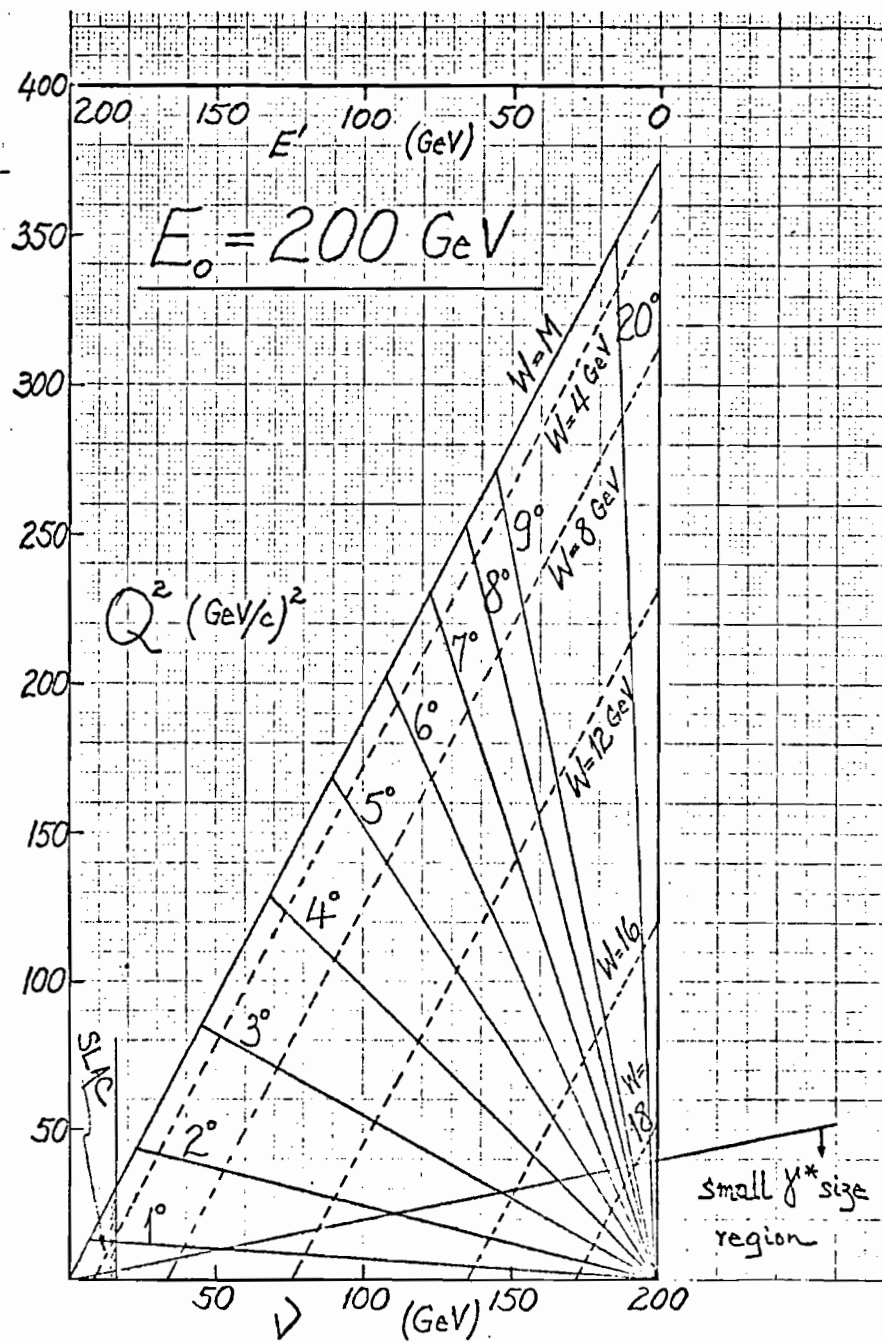


Figure 10

DEEP INELASTIC ELECTRON SCATTERING EVENTS/HOUR AT NAL,
IN PROPOSAL 164. ELECTRICAL BEAM = 250.0 GEV.

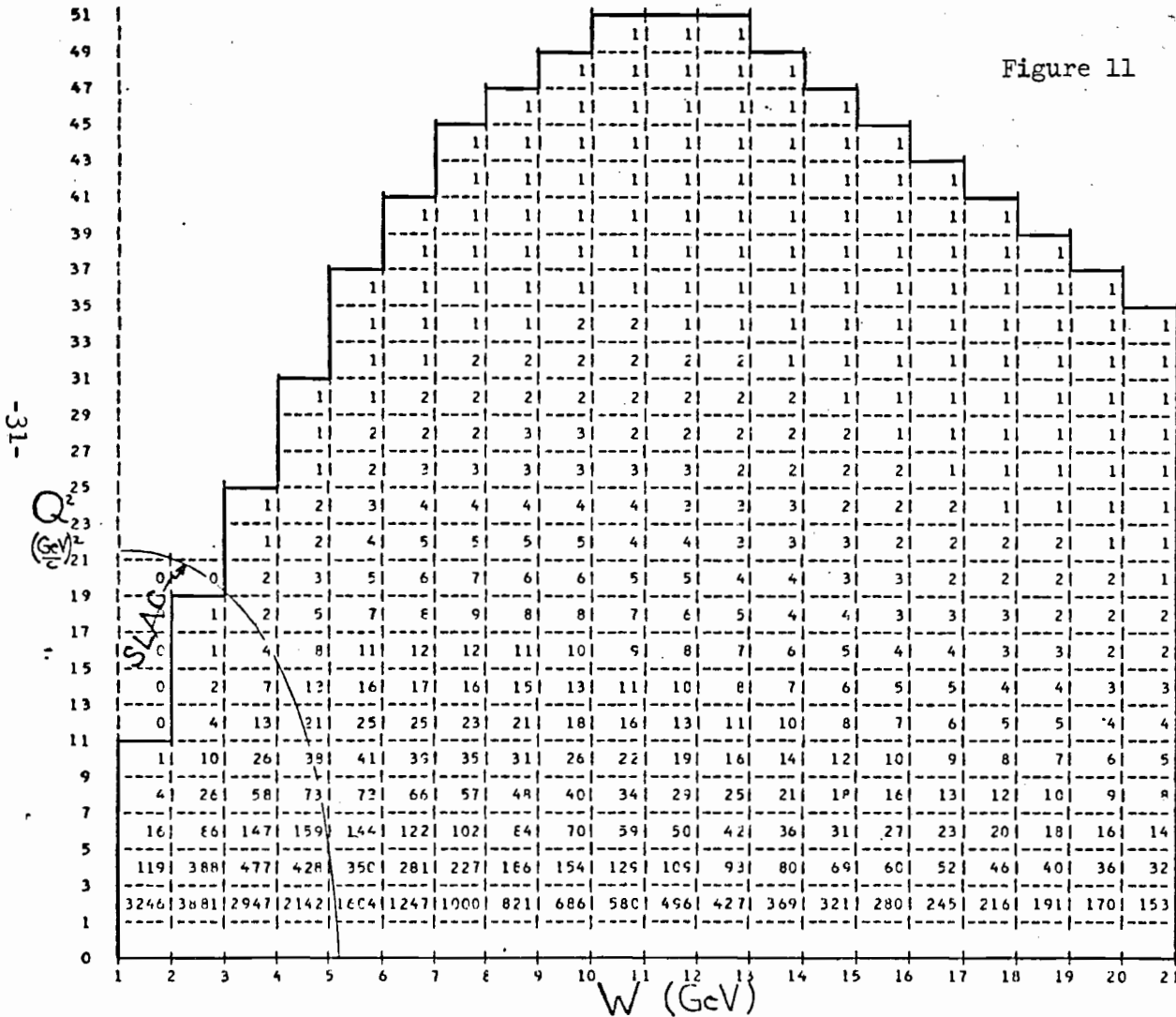
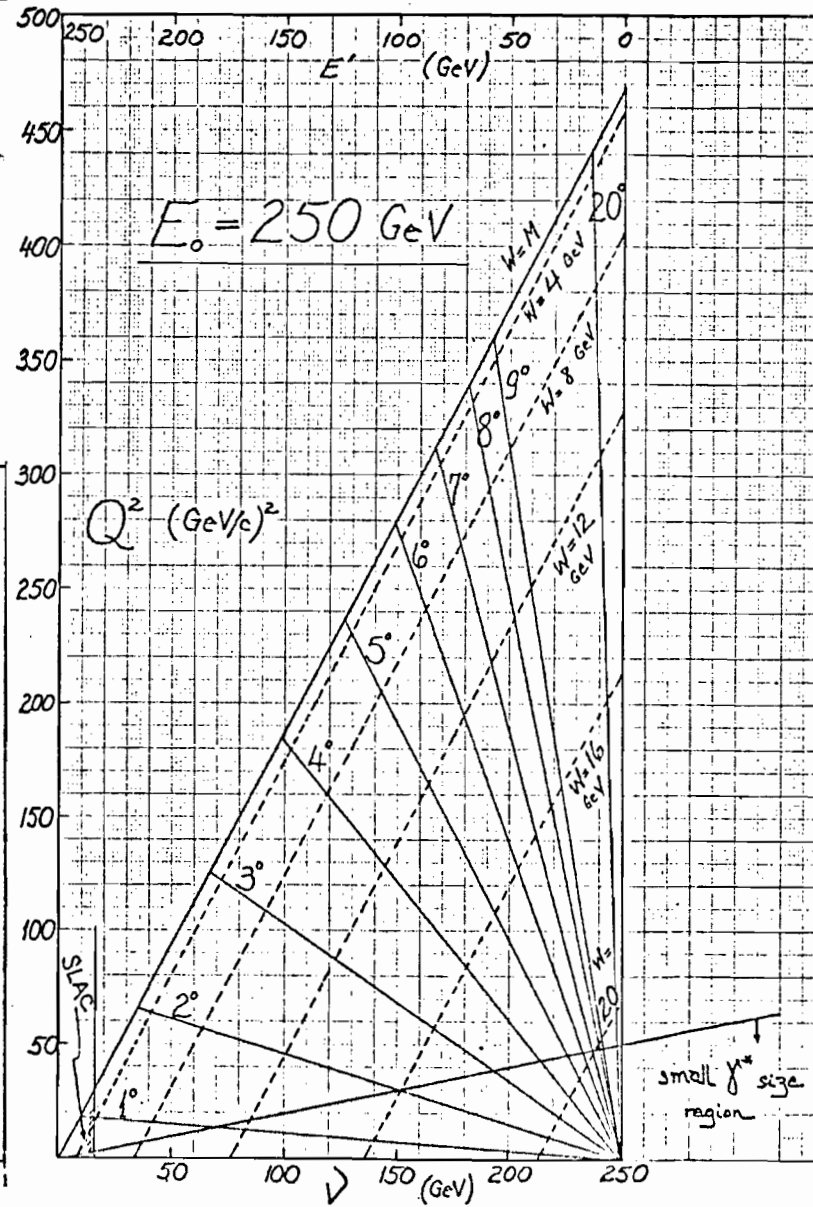


Figure 11



events/hr-nb is obtained. We have computed the event rates, down to 1 count/hr. These are displayed in Fig. 7 for the case of 50 GeV beam electrons. The kinematical region of (Q^2, ν) is shown with fixed values of the scattering angle and fixed values of W . Fig. 8-11 provide the counting rates with electron beam energies of 100, 150, 200 and 250 GeV.

These figures demonstrate the value of performing this deep inelastic electron scattering experiment at NAL. High counting rates are available at the largest possible kinematical values in W , even in the deep scattering region of $Q^2 \sim 8 \text{ GeV}/c^2$.

2. Search for Lee-Wick Heavy Photons as Exchange Particles in Deep Inelastic e - N Collisions.

Divergence difficulties of Quantum Electrodynamics and Weak Interaction dynamics could be removed by postulated⁽¹⁶⁾ negative metric "heavy photons" and spin zero intermediate bosons, B^0 and W_0^0 . The B^0 modifies the one-photon-exchange propagator. If a B^0 exists, it should be manifested in deep inelastic electron scattering processes as an exchanged particle. Consequently, the scaling properties of nucleon structure functions are modified by the equations displayed in Fig. 12. In these $F_1(\omega)$ and $F_2(\omega)$ describe the parts of the nucleon structure functions which obey the scaling law, presumably in one-photon-exchange processes. A limiting value of $M_{B^0} > 9 \text{ GeV}$ is deduced for the mass of a heavy photon, from currently available SLAC measurements. Theoretically, the mass of B^0 is predicted⁽¹⁶⁾ to be $M_{B^0} = 37.29 \text{ GeV}$ or possibly higher⁽¹⁷⁾. The most likely decay modes of the B^0 are e^+e^- and $\mu^+\mu^-$, with equal branching ratios. In Section C. we discuss the possibility of observing

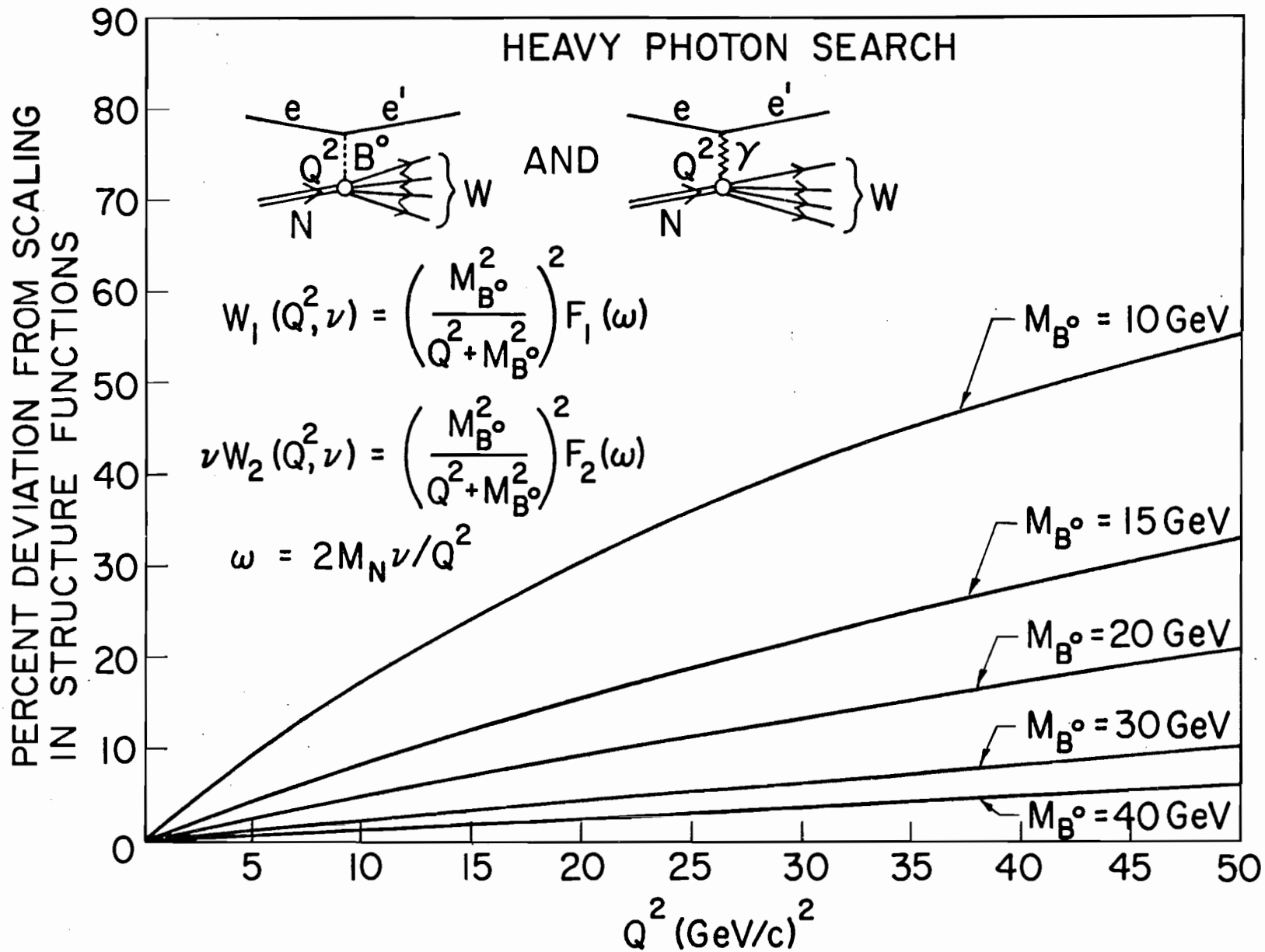


Figure 12

B^0 production in $e - N$ collisions as part of our proposed QED tests, especially in the trident process. In Fig. 12 the result of a computation is shown. We exhibit the expected percentage deviation from the scaling law of nucleon structure functions, in terms of assumed B^0 mass values. As a function of Q^2 a dramatic and gradual deviation could be observed, up to Q^2 values of $50(\text{GeV}/c)^2$, with the counting rates of our experiment at NAL. For example, if $M_{B^0} = 40 \text{ GeV}$, at $Q^2 = 50 (\text{GeV}/c)^2$ we should observe a 6% discrepancy; if $M_{B^0} = 30 \text{ GeV}$, the discrepancy is 10% and at $M_{B^0} = 20 \text{ GeV}$, this is 20%.

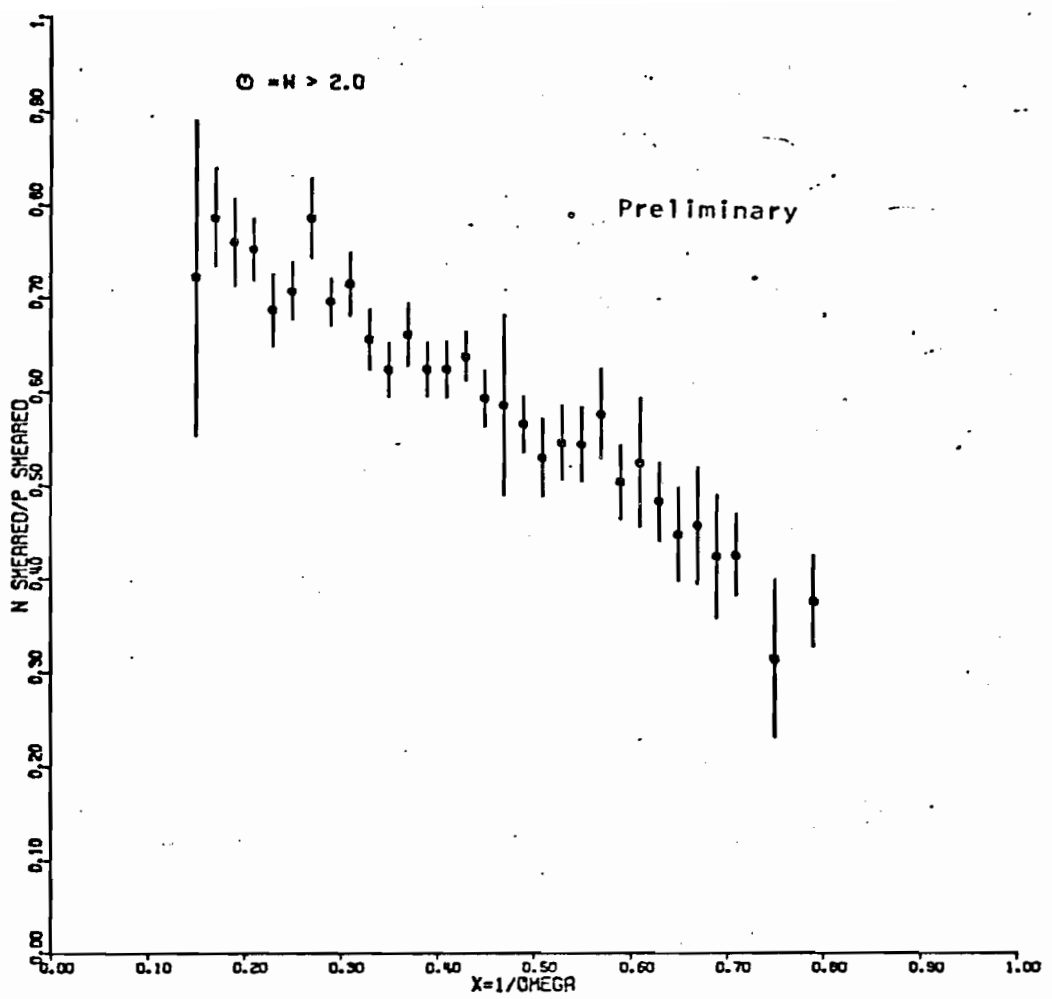
We wish to stress the value of this search method. At NAL, using 400 - 500 GeV protons, experiments designed to detect the production and decay of B^0 's (such as in this experiment with tridents and in E - 70) are limited to observing B^0 masses of up to about 20 GeV. Therefore, a search for the B^0 in the higher mass range of 20 - 40 GeV can only be made possible by observing carefully, changes in the scaling law of $e - N$ deep scattering collisions.

3. Deep Inelastic Electron-Neutron Scattering.

Compared to electron-proton scattering processes and together with these, the study of electron-neutron deep inelastic scattering provides valuable new knowledge. Rigorously, several nucleon constituent theories can be distinguished and possibly new scaling variables discovered only from a complete set of data available both in $e-p$ and $e-n$ experiments. In this case, the basic information is contained in the nucleon structure function ratio, W_2^n / W_2^p and the difference $(\nu W_2^p - \nu W_2^n)$, as a function of a given scaling variable.

We propose to measure the e -neutron deep inelastic scattering cross sections at NAL, using a LD_2 target. With the measured proton-target and deuterium target electron cross sections, the neutron-target

$$W_2^n / W_2^p$$



$$\nu W_2^p - \nu W_2^n$$

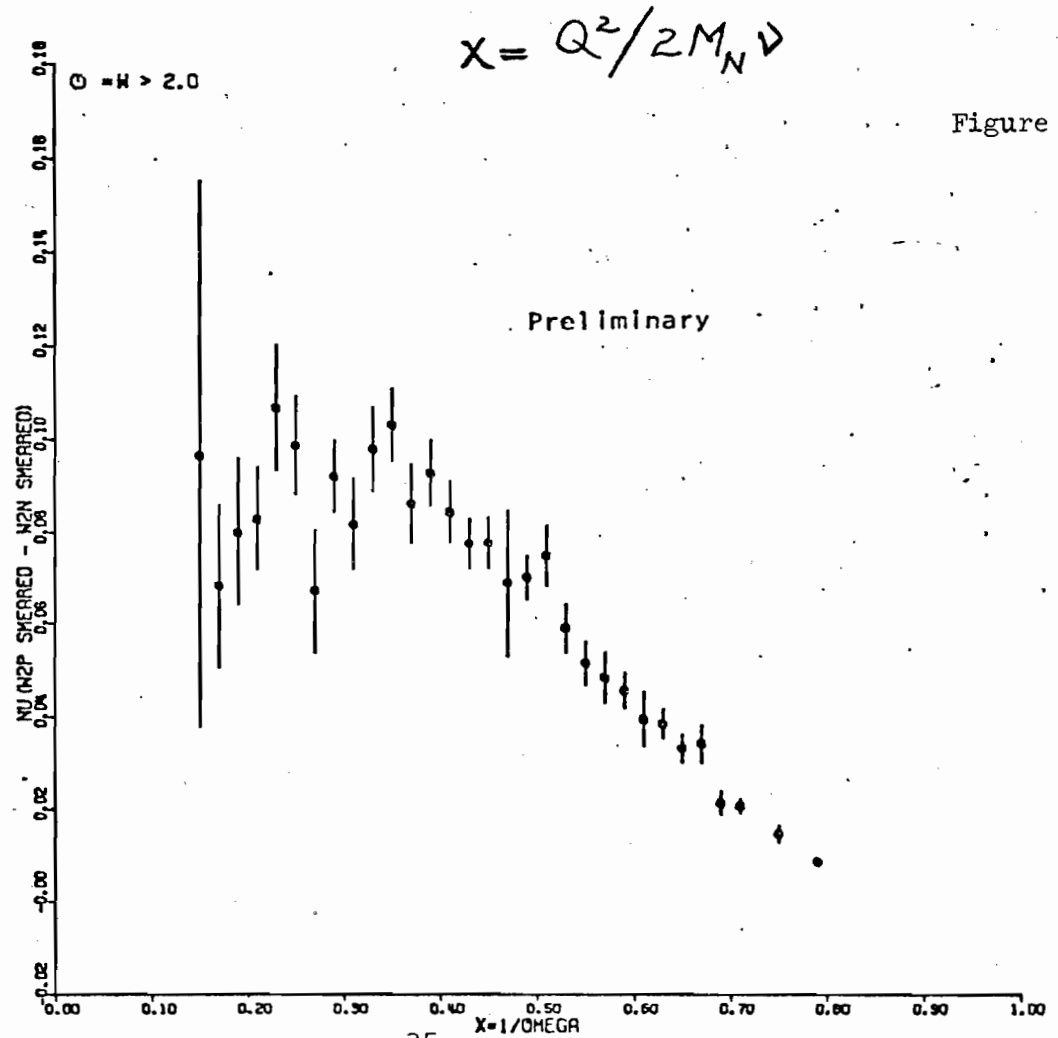


Figure 13

cross sections will be unfolded by a newly developed⁽¹⁸⁾ reliable procedure. In Fig. 13 the recent data from SLAC is demonstrated, exhibiting⁽¹⁹⁾ the ratio and difference of nucleon structure functions of protons and neutrons. We propose to observe the behavior of these quantities, in the new kinematical region which is made available at NAL.

4. Two-Photon Interaction Processes in High Energy Electron-Proton Coulomb Collisions.

A unique and unexplored interaction mechanism is made available at NAL, in high energy e-p Coulomb collisions. By studying these collisions a new field of investigation is opened, based on the photon-photon interaction process. In this case, both beam electrons and target protons are the providers of low Q^2 and energetic gamma-rays:

$$\left. \begin{aligned} e^- p \rightarrow (e^- p) + \gamma_e \gamma_p &\rightarrow \gamma\gamma (\pi^0, \eta, \dots) \\ \gamma_e \gamma_p &\rightarrow e^+ e^- ; \mu^+ \mu^- \end{aligned} \right\} \quad (19)$$

Thus, if suitable experimental conditions are provided, the $\gamma\gamma$ annihilation processes can be identified and separated from all other ep collision mechanisms.

The excellent energy resolution and good space definition of our spectrometer system will permit the observation of the following reactions at NAL:

$$e^- p \rightarrow e^- p \gamma\gamma \quad (20)$$

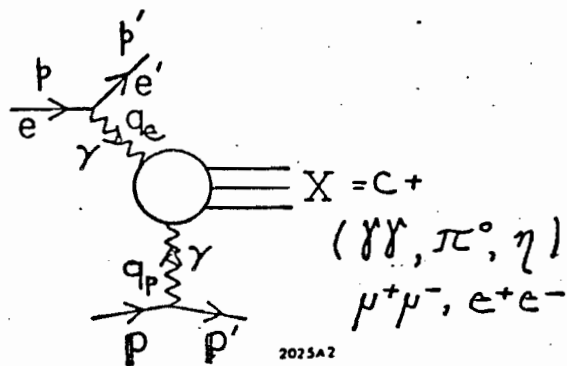
$$e^- p \rightarrow e^- p e^+ e^- \quad (21)$$

$$e^- p \rightarrow e^- p \mu^+ \mu^- \quad (22)$$

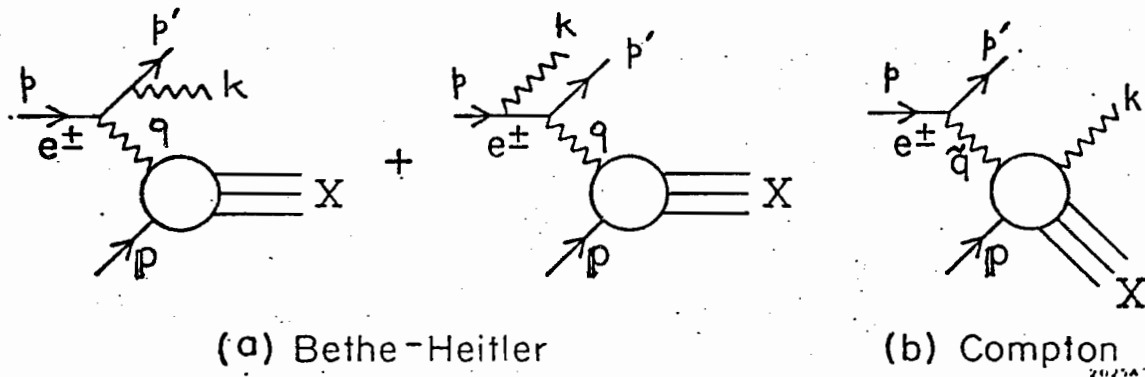
In these reactions the final nucleon variables are reconstructed from the observed gamma-ray pairs or lepton pairs, in coincidence with almost zero degree scattered electrons. In the sample of events, kinematical constraints will be imposed to ascertain that the Q^2 of the proton vertex is also very small. Thus, the interaction process depicted in Fig. 14 (a) can be isolated and tested.

Specifically, this two-photon annihilation mechanism produces only charge conjugation event ($C = +$) states. For example the process $\gamma_e \gamma_p \rightarrow \pi^0 \rightarrow \gamma\gamma$ is especially rewarding to study. Once the π^0 sample of events is isolated together with the above kinematically constraining cuts, this process measures directly a fundamental quantity, the π^0 form factor. We believe, the kinematics of this case is sufficiently well defined to allow for the verification that the π^0 is derived from a $\gamma_e \gamma_p$ interaction, rather than being produced by other hadronic excitation processes. Also, in the case of lepton pair formation [in eq.(19)] the leptons are preferentially distributed in the forward and backward cones defined in the $\gamma_e \gamma_p$ center of mass system⁽⁹⁾.

The cross sections for these e-p Coulomb collisions (reactions 19) grow logarithmically as a function of the e-p center of mass energy. Thus, at NAL energies sizable cross sectional values are developed for the processes shown in Fig. 14 (a). The energy and production angle dependence of these cross sections are evaluated⁽⁹⁾ in a straightforward manner. These are made⁽⁹⁾ primarily for the benefit of projected experiments with e^+e^- colliding beams. Compared to similar Coulomb collisions in e^+e^- storage rings, using a reliable formalism⁽²⁰⁾, we estimate that at NAL energies the e-p process is reduced by no more than a factor of 5 - 10.



(A) Two Photon Annihilation Production Processes in e-p Collisions.



(B) Wide Angle $e^\pm p$ Bremsstrahlung

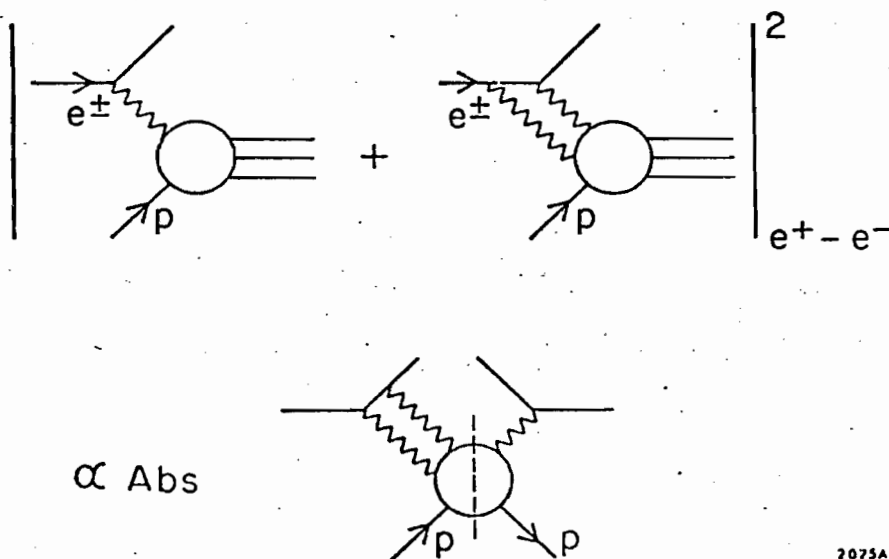


Figure 14

2075A1

(C) Two Photon Exchange Contribution to $\sigma_{e^+p \rightarrow e^+ \text{ all}} - \sigma_{e^-p \rightarrow e^- \text{ all}}$

Therefore, typical e-p induced cross sections of reactions (20-22) via this mechanism are in the range of 10^{-32} cm^2 - 10^{-33} cm^2 . These yield several hundred counts/hr at NAL.

C. Tests of Quantum Electrodynamics with Electron and Positron Beams.

At NAL, important tests of Quantum Electrodynamics can be made possible because remarkable advantages can be derived from development of the high energy and high quality electron beam designed by our group. Both electrons and positrons will be available at NAL, having the same beam intensities and the same experimental qualities. This possibility creates the opportunity for positron-electron difference experiments to be readily implemented. The difference $\sigma(e^+) - \sigma(e^-)$ measures directly the interference term between the Bethe-Heitler and Compton processes. By the measurement of this term we hope to gain new knowledge concerning the constituent nature of nucleons. A quasi-elastic peak, due to the scattering of virtual photons off of constituents is expected to appear, when this term is examined as a function of a scaled variable.

We propose to measure the cross sections and observe the energy and angular dependences of the trident process and wide angle bremsstrahlung process. At NAL we will use both incident electrons and positrons in the energy range of 20 - 250 GeV. Using the capabilities of the e^+ beams and our spectrometer system, coincidence measurements will be made between scattered electrons and forward wide angle lepton pairs or between scattered electrons and single hard photons. We propose to explore the behavior of time-like and space-like propagators both for the cases of virtual photons (M_γ), and virtual leptons (M^*). By choosing the correct experimental conditions, the trident process is best used to study the behavior of virtual photon propagators, both in the time-like and space-like regions.

The wide angle bremsstrahlung process is a better tool with which to explore the time-like and space-like regions of virtual electron propagators. With these measurements, critical tests of Quantum Electrodynamics theory will be made at regions which are only accessible at NAL. The rates of these processes, at NAL beam energies and intensities are such that photon propagators will be explored both in the time-like and space-like regions up to values of $M_\gamma \sim 5 - 6$ GeV; lepton propagators will be examined up to values of $M^* \sim 8 - 9$ GeV also in the time-like and space-like regions.

1. Tridents and Search of Lee-Wick Heavy Photons.

The trident process is the production of lepton pairs in the (nuclear) Coulomb field, induced by an incident lepton radiating a virtual photon. We propose to study and measure the cross sections of the following trident formations:

$$\left. \begin{aligned} e^+ &\rightarrow (e^+)' + e^+e^- \\ e^- &\rightarrow (e^-)' + e^+e^- \end{aligned} \right\} \quad (23)$$

$$\left. \begin{aligned} e^+ &\rightarrow (e^+)' + \mu^+\mu^- \\ e^- &\rightarrow (e^-)' + \mu^+\mu^- \end{aligned} \right\} \quad (24)$$

We note that reactions (23) and (24) are distinguished from the processes in (21) and (22) by kinematical conditions and event triggering requirements. Of course, during data acquisition there will be an overlap which is sorted out in the data analysis phase of our experiment.

The tridents in (23) and (24), and their complements initiated with incident muons, have been examined for some time in detailed theoretical formulations⁽²¹⁾ and extensive computer calculations⁽²²⁾. Up until now however, only one significant experiment has been done at moderately high energy. This is the experiment⁽²³⁾ which confirmed definitively the Fermi

spin-statistic assignment of the muon by measuring the cross section of $\mu \rightarrow \mu\mu\mu$, using a 10 GeV muon beam at BNL.

The trident cross sections have the following characteristic behavior:

$$d\sigma \sim \frac{Z^2 \alpha^4 F^2 (Q_N^2)}{Q_N^4 (M_\gamma)^4 [M^{*2} - m_\ell^2]^2} \quad (25)$$

where, Q_N^2 is the (small) momentum transfer squared to the nucleus or nucleon, M_γ^2 is the time-like or space-like virtual photon-propagator mass squared, and M^{*2} is the mass squared of a time-like or space-like propagating virtual lepton. Specific configurations are devised to enhance one of the above four cases, among space-like or time-like M_γ^2 or M^{*2} . For example, the representation in which Q_N^2 is small and M^{*2} is small will generate sizable cross sections with large M_γ^2 . The time-like region of M_γ^2 is enhanced by observing large transverse momentum e^+e^- or $\mu^+\mu^-$ pairs, predominantly in the forward production cone. (See our Configuration I in Section D.)

The total cross section of process (23) in the incident energy range 20 - 250 GeV is (1.5 - 2.5)mb and for process (24) is (0.04-0.12) μ b, using LH_2 targets. The behavior of large time-like and space-like M_γ^2 cross sections have been calculated (24a) using detailed and precise computer techniques. Based on this calculation we estimate the differential cross section of (23) to be:

$$\frac{d\sigma}{dM_\gamma} \sim 10^{-33} \cdot \left(\frac{1 \text{ GeV}}{M_\gamma} \right)^4 \text{ cm}^2 .$$

The cross section of the trident producing muon pairs in (24) is suppressed by the mass factor $(m_e/m_\mu)^2 \sim 4 \times 10^{-4}$. Hence, at large time-like M_γ^2 values this process will be useful and observable only if a

Lee-Wick heavy photon B^0 , is produced. In this eventuality the rates of reactions (23) and (24) will be the same because B^0 's have equal branching ratios in the decay modes (e^+e^-) and $(\mu^+\mu^-)$. Large signals will be observed at NAL if the B^0 mass is less than ~ 13 GeV. The trident-like reaction:

$$e^\pm + Z \rightarrow e^\pm + Z' + B^0 \quad (26)$$

is calculated^(24b) with reliable precision to have cross sections of $\sim 10^{-34}$ cm² for $M_{B^0} = 7$ GeV and 10^{-36} cm² for $M_{B^0} = 13$ GeV, if an electron beam is used at 200 GeV.

The distinct advantage of searching for the B^0 in reactions (23) and (24) is the fact that by QED theory reliable cross sections can be calculated. In the case of negative search results, at least meaningful mass limits can be set. This situation should be compared in a complementary fashion with our other pion experiment proposal (and also with E-70) in which the B^0 search can extend up to mass values of about 21 GeV. But in these cases, reliable theoretical cross sections are not so available.

2. Wide Angle Bremsstrahlung and Search for Heavy Excited Leptons.

The proposed elastic wide angle bremsstrahlung studies are fully described in our original electron proposal 164-II. We propose to observe the energy and angular dependences and measure the cross sections of:

$$\left. \begin{array}{l} e^- p \rightarrow e^- p \gamma \\ e^+ p \rightarrow e^+ p \gamma \end{array} \right\} \quad (27)$$

using electron and positron beams in the energy range of 20 - 250 GeV at NAL. Positron-electron cross sectional differences will be used to measure the interference between the Bethe-Heitler and Compton interaction

processes, shown in Fig. 14(b). Structure will be searched for in the effective mass of the final ($e\gamma$) system to observe the production of a possible heavy excited lepton⁽²⁵⁾:

$$E_{\pm}^* \rightarrow e^{\pm} \gamma \quad (28)$$

This search will extend up to mass values of about 8-9 GeV.

3. Inelastic Wide Angle Bremsstrahlung with Electrons and Positrons and Search for Nucleon Constituents.

Significant and instructive theoretical progress has been made recently⁽²⁶⁾ which indicates that the elusive quasi-elastic peaks (due to scattering of virtual photons from nucleon constituents) in deep inelastic electron scattering, could be masked. The masking mechanism could be due to an abundance of other processes which proceed with even charge conjugation ($C = +$) quantum number. Therefore, it is argued, to unveil these quasi-elastic peaks one must look in deep inelastic ep processes in which the final states force the amplitudes to have odd charge conjugation ($C = -$) quantum number. These are the inelastic wide angle bremsstrahlung reactions:

$$\left. \begin{array}{l} e^- p \rightarrow e^- \gamma + \text{anything} \\ e^+ p \rightarrow e^+ \gamma + \text{anything} \end{array} \right\} \quad (29)$$

We propose to investigate these important reactions at NAL energies. Although the predicted cross sections drop linearly with S , the high energy available at NAL makes it possible to achieve moderately large Q^2 and \tilde{Q}^2 values at rather small angles. [Q^2 and \tilde{Q}^2 are the momentum transfers in the Bethe-Heitler and Compton diagrams of Fig. 14(b)]. From this point of view, the acceptance and resolution qualities of our spectrometer system are matched very well. The incident e^{\pm} beam energy range 20 - 100 GeV produces counts of several hundreds/hr in our detectors.

Only by doing an electron-positron difference experiment is it possible to measure the nucleon structure functions of process (29), $V(x)$. In measuring $V(x)$ (a structure function containing the cube of parton charges), as a function of the scaling variable x , we expect to find a behavior which is entirely different from the structure function of inclusive deep inelastic electron scattering. This is because $\nu W_2(x)$ is a nucleon structure function arising from the square of parton charges. Also, the ratio $[\sigma(e^+) - \sigma(e^-)] / [\sigma(e^+) + \sigma(e^-)]$ in a well defined formalism, is a direct measure of the mean-cube of parton charges. Therefore, we propose to measure, investigate and compare the behavior of $V(x)$ and $\nu W_2(x)$ in the same experiment. If there are distinct nucleon constituents, this proposed method appears to be one of the best ways of searching for and acquiring new knowledge in this field.

4. Search for Quark Production in Electromagnetic Processes.

This search is described in our original electron proposal 164-II. We wish to emphasize the value of searching for the production of quarks in electromagnetic processes because theoretical cross sections are more reliably calculated for these cases. A recent experiment at the ISR indicates⁽²⁷⁾ that quark masses could be large and in the limiting range of being greater than 13-22 GeV. We propose to look for the production of quarks in all of the above discussed studies. The method was described earlier by us and will not be repeated here.

SUMMARY

We summarize the prominent features of a proposed experimental program at NAL based on the unique facility of electron and positron ultra-high energy beams. The attached Table III provides a condensed summary.

The experimental luminosity for $10^8 e/pulse$, at a rate of 1 pulse/4 sec, with a 25 cm LH_2 target is 100 events/ $10^{-33}/hr$ (in electroproduction and leptonic processes the luminosity is $L_e = 10^{35} cm^{-2}.hr^{-1}$). Therefore, the experimental sensitivity in a given search run of 100 hr ($\sim 10^5$ pulses) and for the observation of 100 sought events is:

$$(\text{Production cross section} \times \text{Branching ratio}) \sigma_e \cdot B = 10^{-35} cm^2 .$$

The limiting sensitivity in the case of negative results is: $\sigma_e \cdot B \sim 10^{-37} cm^2$.

Similarly, in the cases of photoproduction by real or virtual photons in our experiment, the experimental sensitivity (defined above) is:

$$\sigma_\gamma \cdot B = 10^{-34} cm^2 ,$$

where σ_γ is the actual photoproduction cross section. The limiting sensitivity here, is: $\sigma_\gamma \cdot B \sim 10^{-36} cm^2$.

TABLE III

PRODUCTION OF MASSIVE OBJECTS IN 150 - 250 GeV e-N COLLISIONS AT NAL FOR THIS PROPOSAL

MASSIVE OBJECT	INTERACTION MECHANISM	PROPOSED SEARCH SAMPLE	ESTIMATED $\sigma(\text{cm}^2)$ AT MASS LIMITS	REMARKS REACTION NO	MASS LIMITS (GeV)	SPECTROMETER CONFIGURATION TYPE
B^0	exchanged in e-N deep inel.scatt.	breakdown of $W_2(x)$ scaling	see Fig. 12	5% deviation in $W_2(x)$ at $Q^2 = 40 \text{ GeV}^2$	40	I and II
B^0	produced in tridents	$e^+e^-, \mu^+\mu^-$ mass of correlated pairs	$10^{-35} - 10^{-36}$	(23), (24), (26)	10-13	I and III
W^+	leptonic	e^+, μ^+ , large P_{\perp} singles	$10^{-37} - 10^{-38}$	(3) (4)	5	III
W^+	semi-leptonic	" "	6×10^{-36}	(5)	10	III
W^+	inclusive photo-production	" "	$4 \times 10^{-33} - 6 \times 10^{-36}$	(6)	10	III
W^+	semi-weak	" "	2×10^{-35}	(7)	10	III
L^+	heavy lepton pairs photo-produced	e^+, μ^+ large P_{\perp}	10^{-35}	(18)	5	III
E^0	electroproduction semi-leptonic	$(e^+\mu^-)$	$10^{-34} - 10^{-37}$	(15)	10	III
E^0	leptonic	$(e^-\mu^+)$ large P_{\perp} correlated pairs		(17)	10	III
E_{\pm}^*	Heavy excited lepton pairs photoproduced	e^+, μ^+, γ large P_{\perp} uncorrelated pair	—	(11)	5	II and III
Quark					10-22	I
SEARCH FOR NUCLEON CONSTITUENTS						
Deep inelastic e^+e^- -N scatt.		e^+ singles and in coincidence with multi-gamma-rays.	See Fig. 8-11 for counting rates		$Q^2 \leq 50(\text{GeV}^2)$ $W \leq 21(\text{GeV})$	I and II
e^+ and e^- tridents		$e^+(e^+e^-)(\mu^+\mu^-)$	10^{-36}		5	I and III
e^+ elastic wide angle Brems.		$e^+ \gamma$	10^{-36}	(27)	8	I and II
e^- inelastic wide angle Brems.		$e^- \gamma$	10^{-36}	(29)	—	I and II
single E_{\pm}^* production electromagnetic		$e^+ \gamma$ mass of correlated pairs	—	(27), (29)	8	I and II
$ep \rightarrow \mu p$	lepton number conservation test.					I

III. EXPERIMENTAL METHOD

A. RADIATIVE CORRECTIONS IN ELECTRON-PROTON SCATTERING

At NAL energies, we know that the magnitude of radiative corrections in e-p scattering is not significantly different from the magnitude of radiative corrections in the μ -p scattering processes. We also show that the desired experimental energy resolution in e-p scattering is not affected by a 25 cm long LH_2 target. For the purpose of this demonstration we have calculated the radiative corrections in both μ -p and e-p scattering, under identical experimental conditions. Precise, reliable and up to date theoretical formulations⁽²⁸⁾ and computer programs⁽²⁹⁾ are used. A typical example is chosen where 160 GeV incident electrons or muons scatter by 3 degrees, in a 25 cm LH_2 target. To compare with these, the same cases are computed with null target thickness. The latter provides a measure of radiative effects which occur during e-p and μ -p scattering processes, irrespective of the thickness of the experimental target.

We have calculated the radiative tail caused by the production of a fixed mass object in both e-p and μ -p scattering processes. The production of a fixed mass narrow resonant state, with mass W and width Γ_w , causes a radiative tail which can be simulated just as well by observing the radiative effect in elastic scattering; in this case $W = M_p$ and $\Gamma_w = 0$. In Fig. 15(a) and (b) we present the results of this precise computation. All four cases are shown, with incident muon and electron beams, with 25 cm LH_2 target and zero length target. We conclude from these figures that the use of a 25 cm long LH_2 target cannot have any significant or detrimental effect on the desired ex-

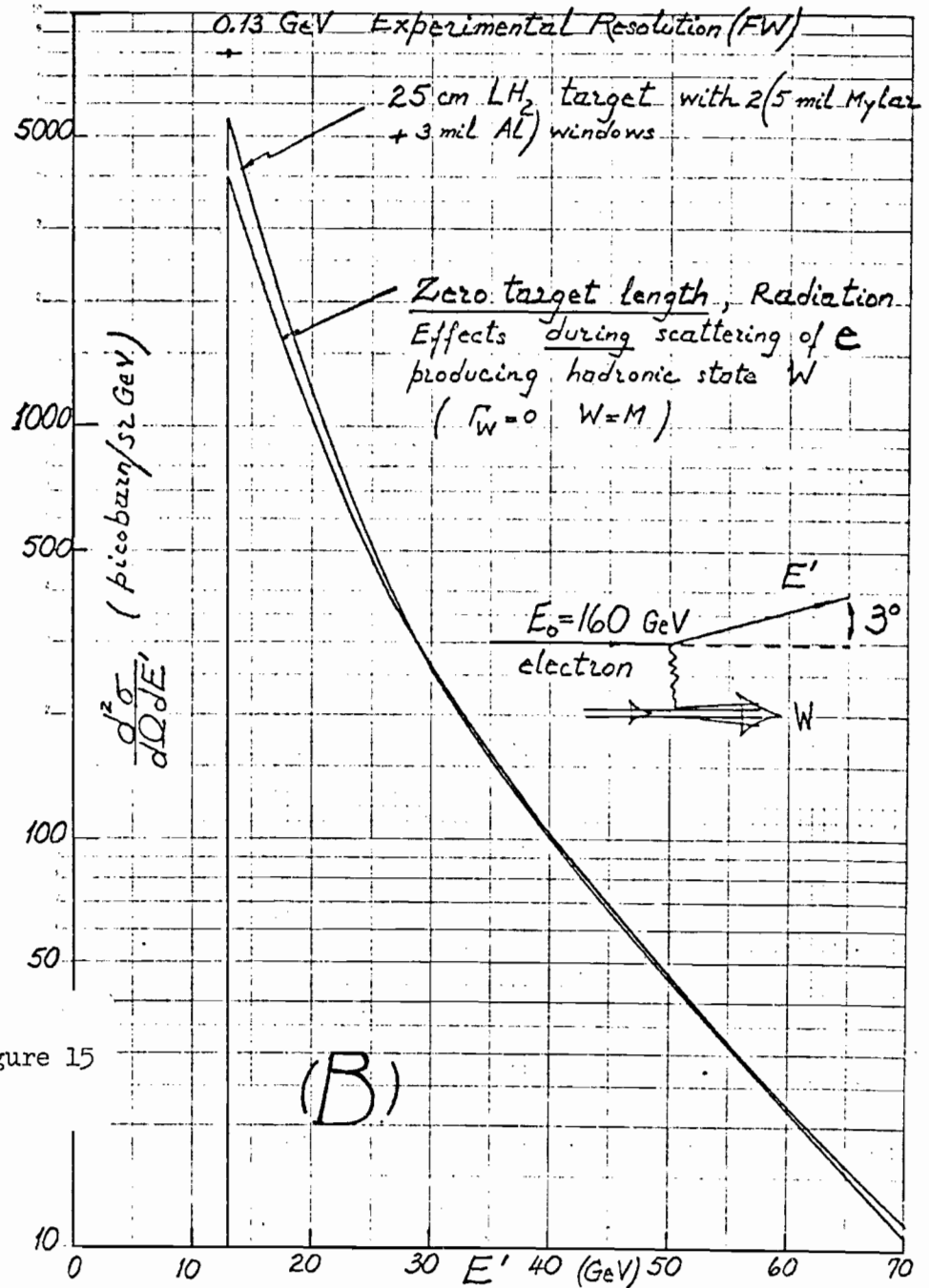
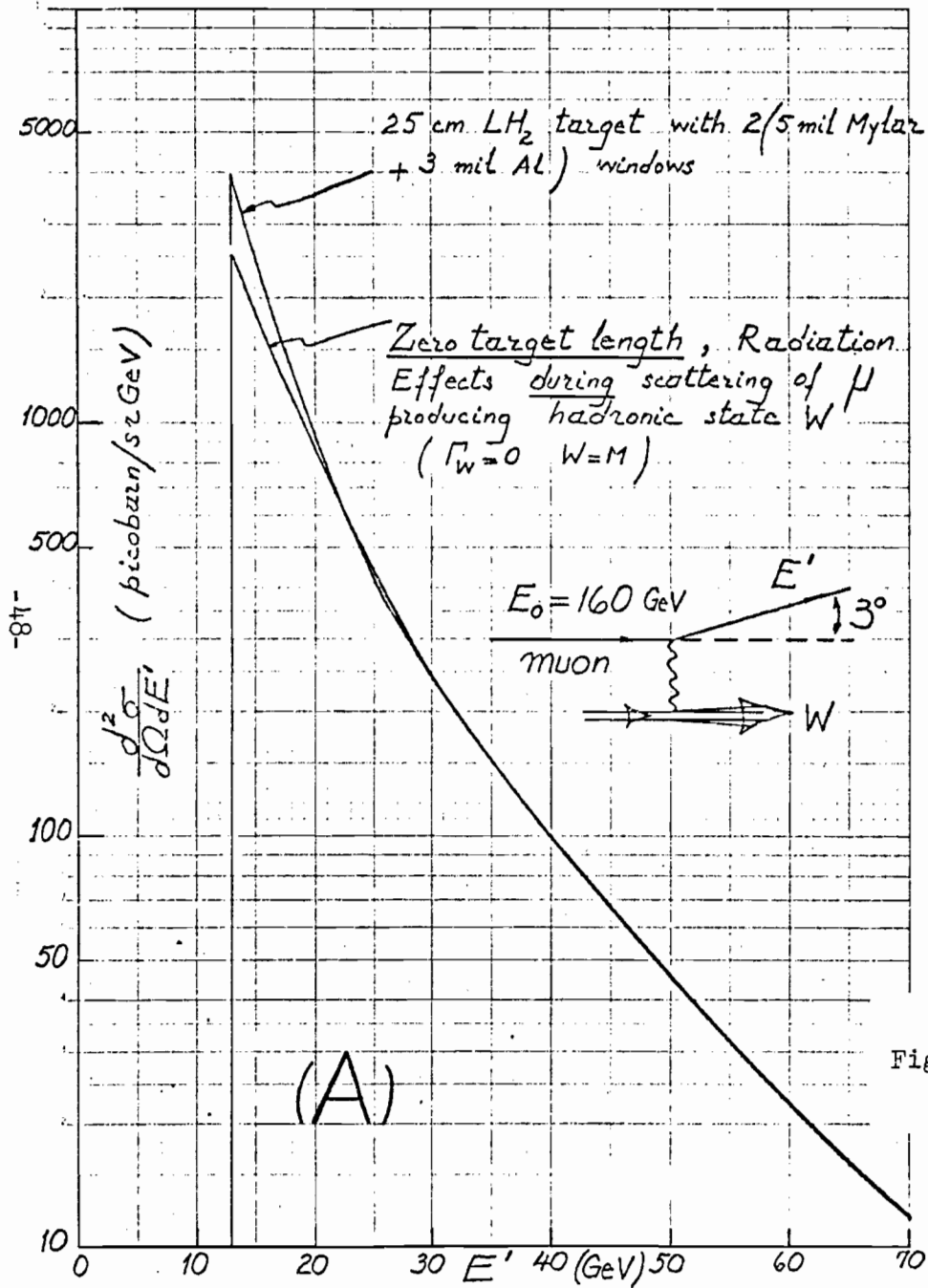


Figure 15

perimental resolution. In fact the full width at half maximum of peaks for all practical purposes, are not affected by the size of our target. This is true in both the "elastic" treatment and the inelastic continuous treatment given below. The position of several such peaks can be observed with good resolution detectors at various kinematical conditions. The natural resonant widths can be unfolded, by well known radiative effect procedures, from the observed line shapes. We have been careful in choosing a target length such that line shape radiative corrections would be due to almost entirely to the natural radiation caused by the scattering process itself.

In Fig. 16 (a) and (b) we present the result of computations for the radiative corrections of deep inelastic scattering cross sections in the continuum. Again, all four cases are given; with e-p and μ -p inelastic scattering (in the continuum) and with 25 cm LH_2 target and null thickness target. The radiative corrections for electron beam experiments at NAL are of the same order of magnitude as the radiative corrections for muon beam experiments. Basically, also the 25 cm LH_2 target produces very little difference. Most of the difference caused lies in the kinematical region of low energy scattered electrons where the radiative tail from elastic scattering dominates. In the regions where the corrections differ they are both calculable are not important (because of small rates in such regions) and do not affect the resolution.

B. BEAM PION IMPURITY CORRECTIONS

We show that corrections due to pion impurities in an electron beam are negligible and irrelevant in e-p experiments at NAL, if we use electrons from the beam which is designed and described in Appendix I.

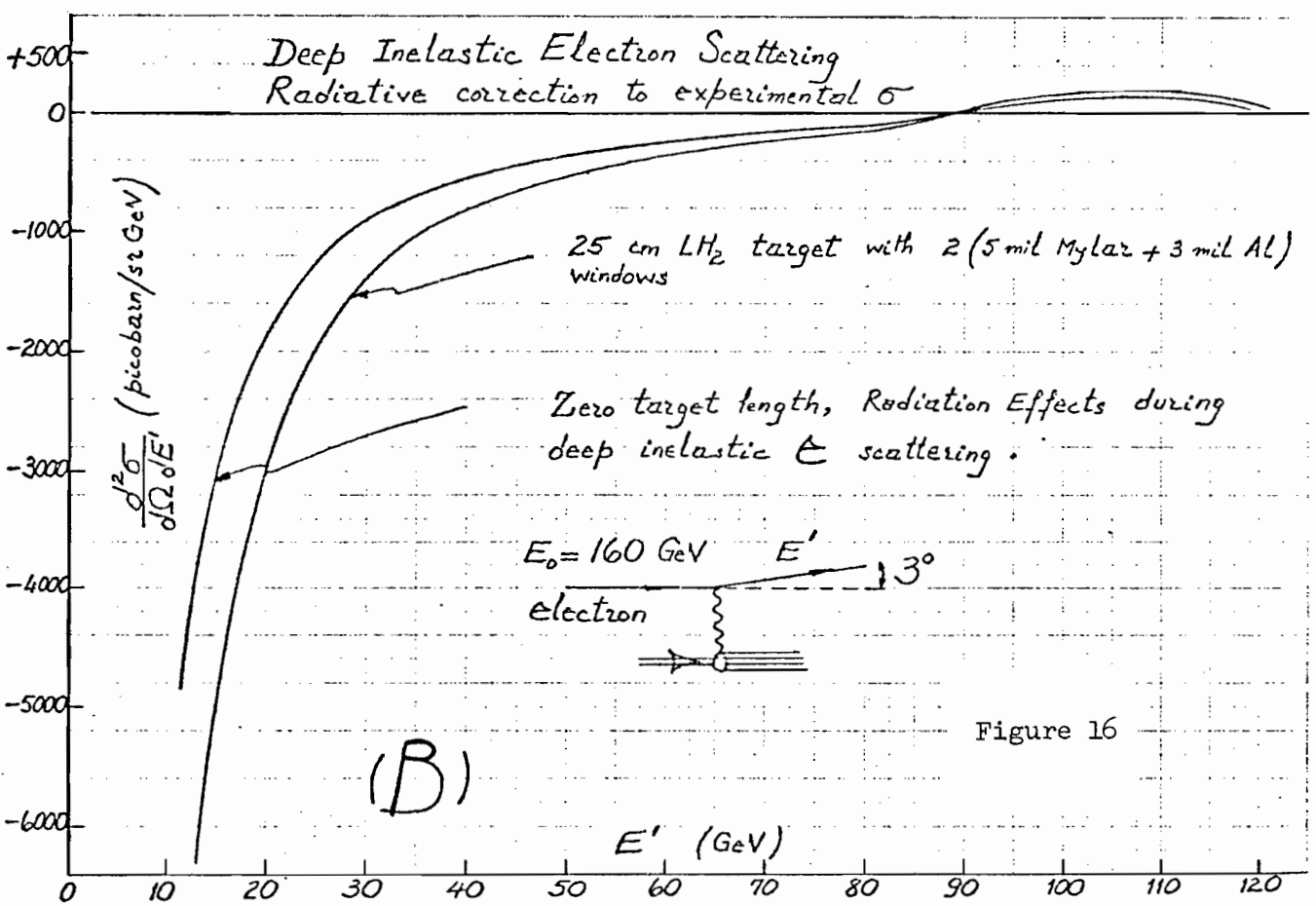
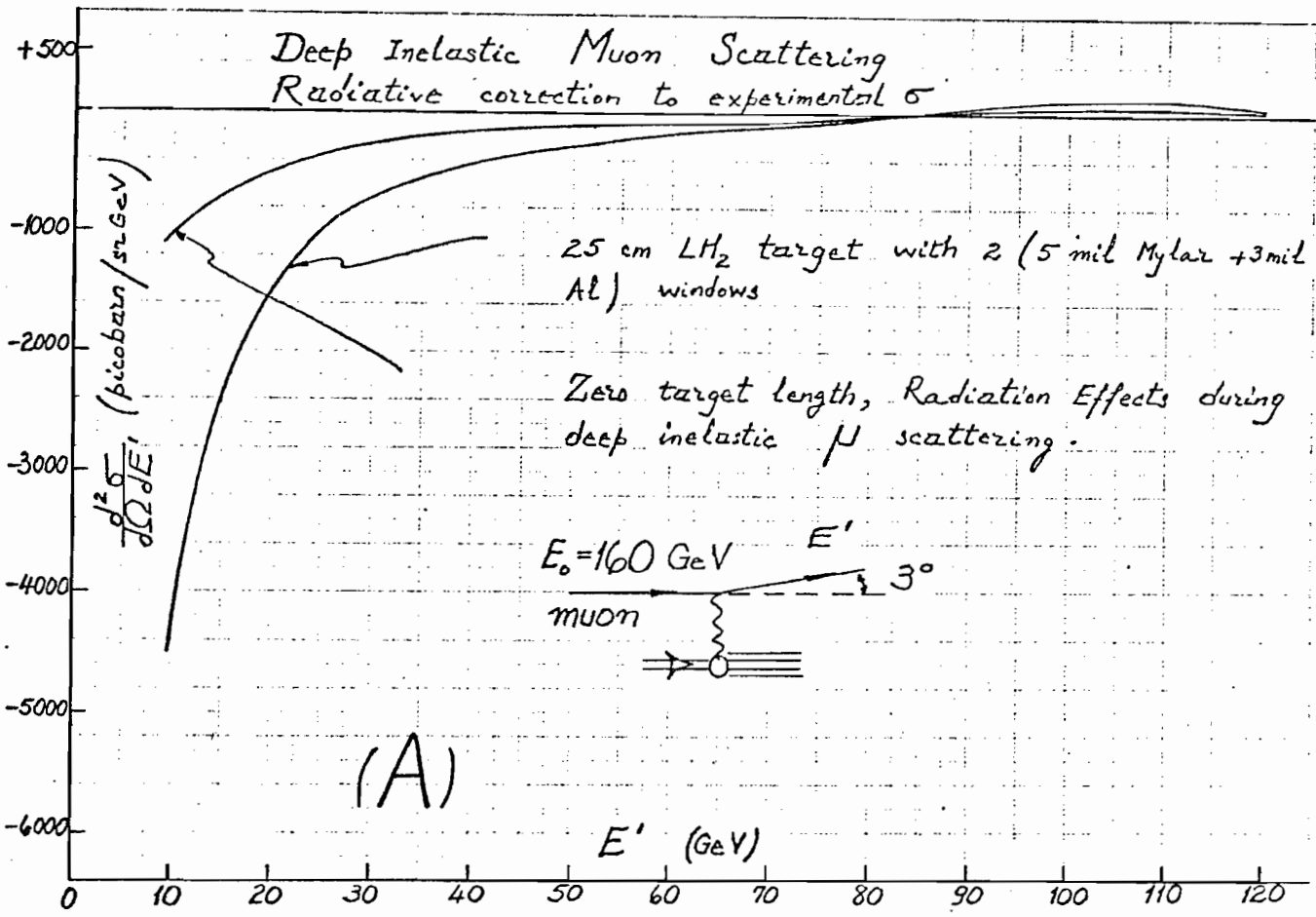
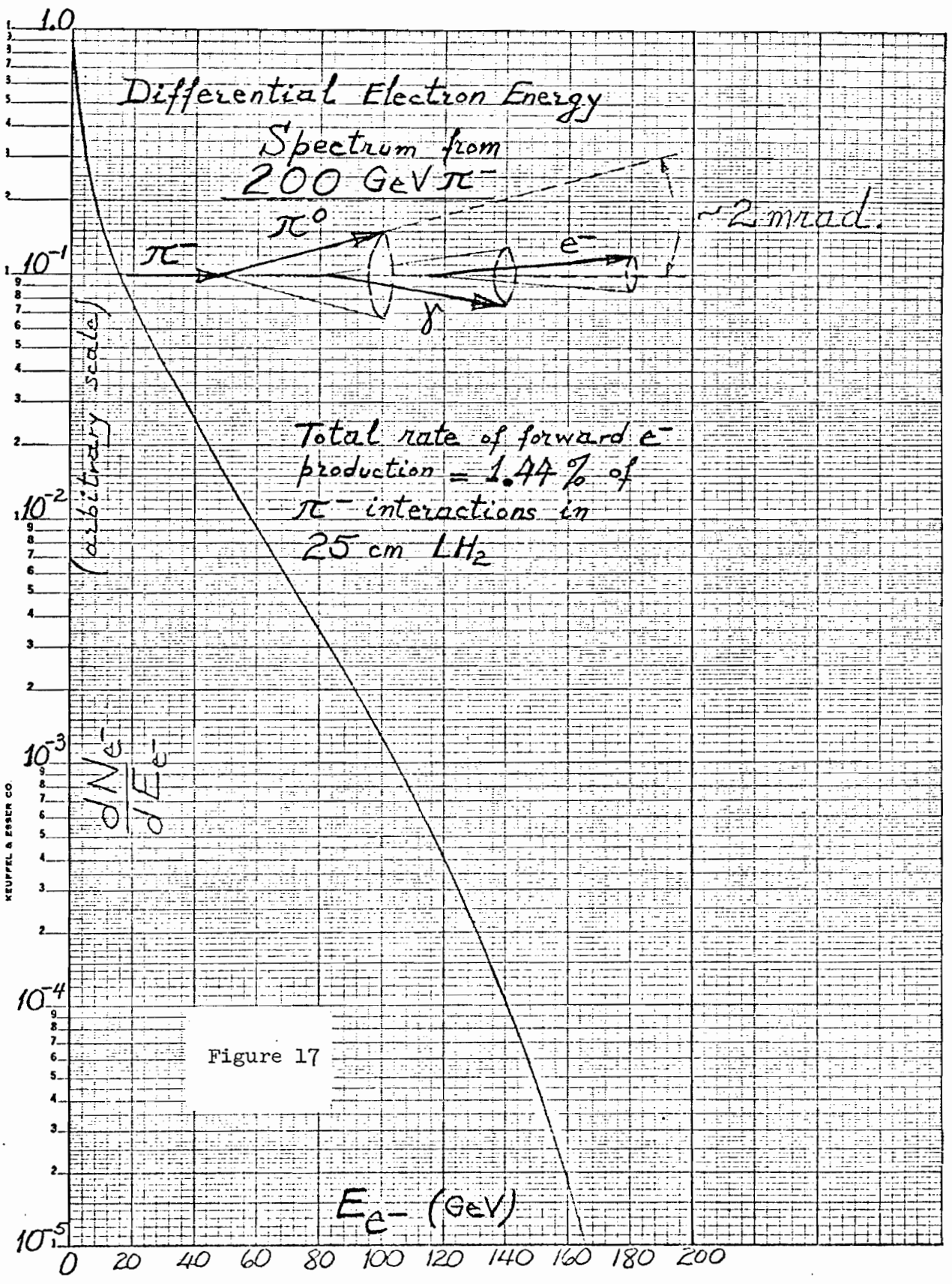


Figure 16

The final figures for the pion impurity in the electron beam are presented in Table III of this appendix. At 100 GeV the π/e ratio is 5×10^{-5} ; at 150 GeV it is 1.7×10^{-5} at 160 GeV and beyond the π/e ratio is null. This high electron purity level is achieved by 1) the geometrical qualities of this beam design, 2) the synchrotron radiation of electrons throughout the beam transport system and our "radiation compensated" beam tuning method, and 3) the use of a 3.3 m LD₂ filter at the front end neutral stage of the beam.

We develop the following arguments by assuming an average π/e ratio of 10^{-5} in the electron beam which is incident on our 25 cm LH₂ experimental target. The ratio of π -N cross sections to e-N cross sections at high energies is about 10^3 . Thus, a fraction of 2.7×10^{-2} of beam impurity pions will interact in the target, primarily producing hadrons ($\pi \rightarrow h$) . A fraction of 2.7×10^{-5} of beam electrons (at a rate of 10^8 e/pulse) will interact, primarily producing a final scattered electron ($e \rightarrow e'$) . Therefore the electron interaction rate is $10^8 \times 2.7 \times 10^{-5} = 2700$ and the pion interaction rate is $10^8 \times 10^{-5} \times 2.7 \times 10^{-2} = 27$; the electron to hadron singles ratio in our electron detector will be 100:1 . Earlier, we have shown (see 164-II) that with our detectors the probability of hadrons being identified as electrons is less than 0.3% , if the momentum of particles is known to 3% . Thus, 1 in 30,000 of scattered and detected electrons is really a hadron. We call these "simulated electrons."

There is another effect originating from the beam's pion impurity that was thought to be detrimental to our experiment: interacting beam impurity pions produce electrons by first producing π^0 's . The



π^0 decays in the target, produce Dalitz pair electrons or pair-produce electrons in two steps - $\pi^0 \rightarrow \gamma\gamma$, $\gamma \rightarrow e^+e^-$. The latter is the dominant effect. We demonstrate that this concern is inconsequential in our electron experiment. In Fig. 17 the result of a computation is shown. The differential electron energy spectrum from the above two step process is given, initiated by 200 GeV π^- beam impurities. The total rate of electron production by pions, the integral of this spectrum, is also given. We find that 1.44% of interacting pions will produce electrons having energies distributed according to the spectrum of Fig. 17. Thus, a fraction of $2.7 \times 10^{-2} \times 1.44 \times 10^{-2} = 4 \times 10^{-4}$ beam pions will produce forward electrons, mostly with energies below 20 GeV. This is a rate of $4 \times 10^{-4} \times 10^3 = 0.4/\text{pulse}$; 1 in 7,000 of small angle and low energy scattered and detected electron is really an electron from beam pion interactions. Similarly, about 1 in 70,000 of larger angle and higher energy scattered electron is "false."

C. 20 kgauss SUPERCONDUCTING DIPOLE MAGNET

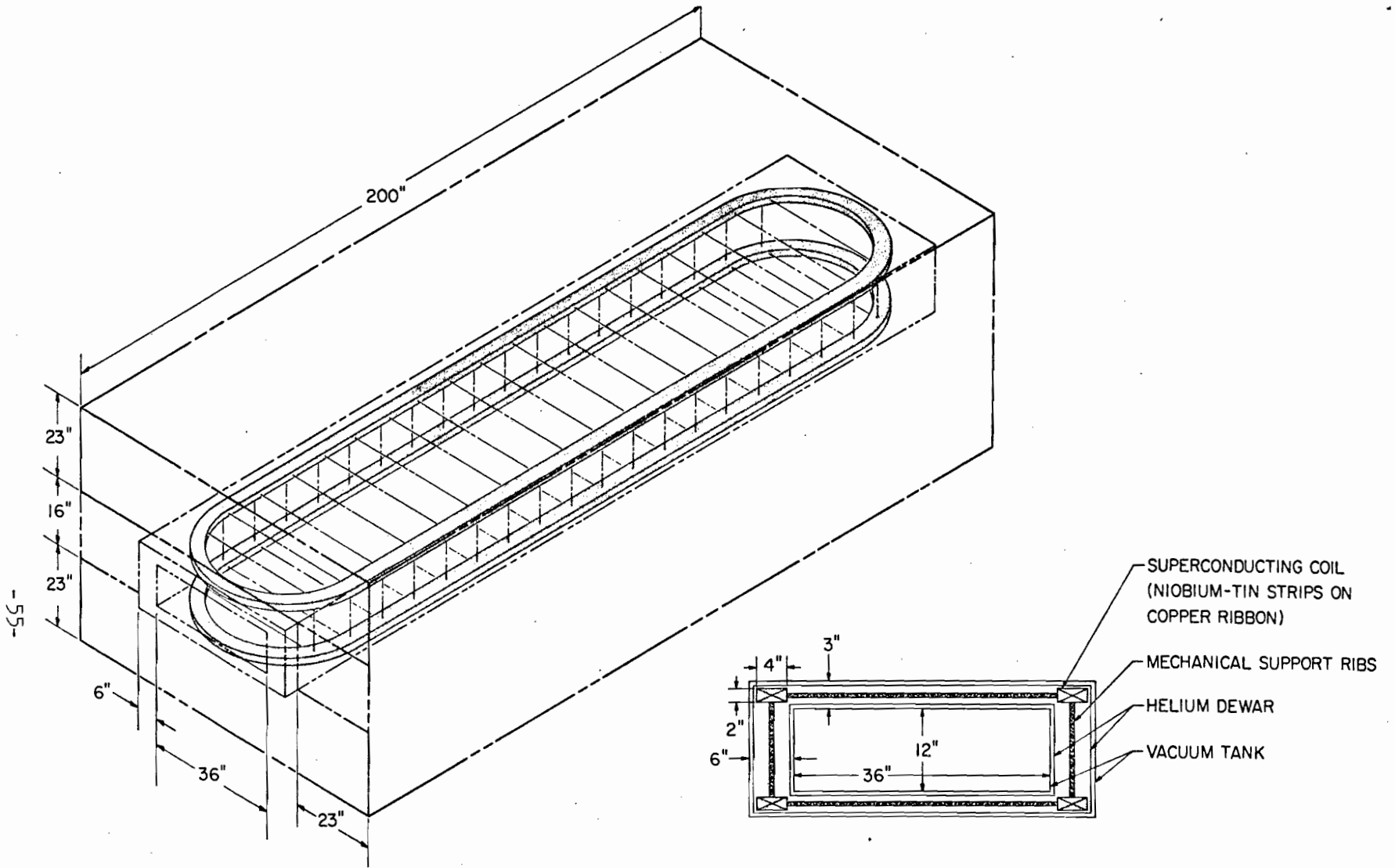
For both our proposed pion and electron experiments at NAL a 20 kgauss analysing dipole magnet is required. The magnet will have a length of 15 ft and a useful aperture of 3 ft in width and 1 ft gap. The analyzing magnet discussed in our original proposal No. 164 has now been redesigned and modified so that it will have superconducting coils. Following our feasibility studies we present a preliminary design of this magnet. An equivalent 18 kgauss magnet with conventional copper coils will consume 1.07 Mwatt power and is

estimated to cost \$ 180 K . The cost estimate of this superconducting 20 kgauss magnet is about \$ 150 K , exclusive of the cryogenic refrigeration system.

Among recent advances in the manufacture of superconductors, a search was made to select a superconductor configuration providing reliable and safe operation. Presently we favor the following available superconductor: a continuous copper ribbon, 1/16" thick and 2" wide with embedded Niobium-Tin superconducting strips. This material conducts adequately 1000 A in a magnet at 30 kgauss.

The dipole magnet design is shown in Fig. 18. Superconducting coils with mechanical supporting ribs are shown inside a helium dewar. This is a 500 liter dewar and is heat shielded by layers of super-insulation, a nitrogen shield, again super-insulation and vacuum. The dewar fits inside a window frame iron magnet. The total ampere-turns are 722,000 AT. A current density of 20,000 A/cm² is made available in a coil cross section area of 50 cm². In each turn a current of 1000 A will be conducted, for a total of 722 turns in each coil. The weight of this magnet is 140 tons. The magnet will be built in sections which will make it easier to assemble or dismantle for shipment to NAL. For the final coil configuration we intend to make calculations with available computer programs, to gradate the current density in the coils and thus achieve a high magnetic field uniformity inside the useful aperture.

We propose to build this magnet for NAL, using our own facilities at HEPL. We have the manpower and equipment to complete this important task. We are presently building an iron magnet approximately eight times as massive as the one described above.



B = 20 kG
 J = 20,000 A/cm²
 SC COIL = 650,000 A-TURNS
 Fe RETURN = 72,000 A-TURNS
 WEIGHT = 140 TON

20 KG SUPERCONDUCTING DIPOLE MAGNET
 (15ft x 3ft x 1ft)

Figure 18

D. EXPERIMENTAL CONFIGURATIONS AND ACCEPTANCES OF THE SPECTROMETER SYSTEM

The makeup of our spectrometer system is simple and modular. Briefly, the central idea is this. With a pion or electron beam, a target and a beam monitor, an analyzing magnet is used together with two large acceptance spectrometer arms to do coincidence measurements. One of these arms is always used to trigger candidate events. This arm will make measurements in singles, on inclusive reactions. The second arm is placed essentially at three different locations to provide coincidence measurements selectively.

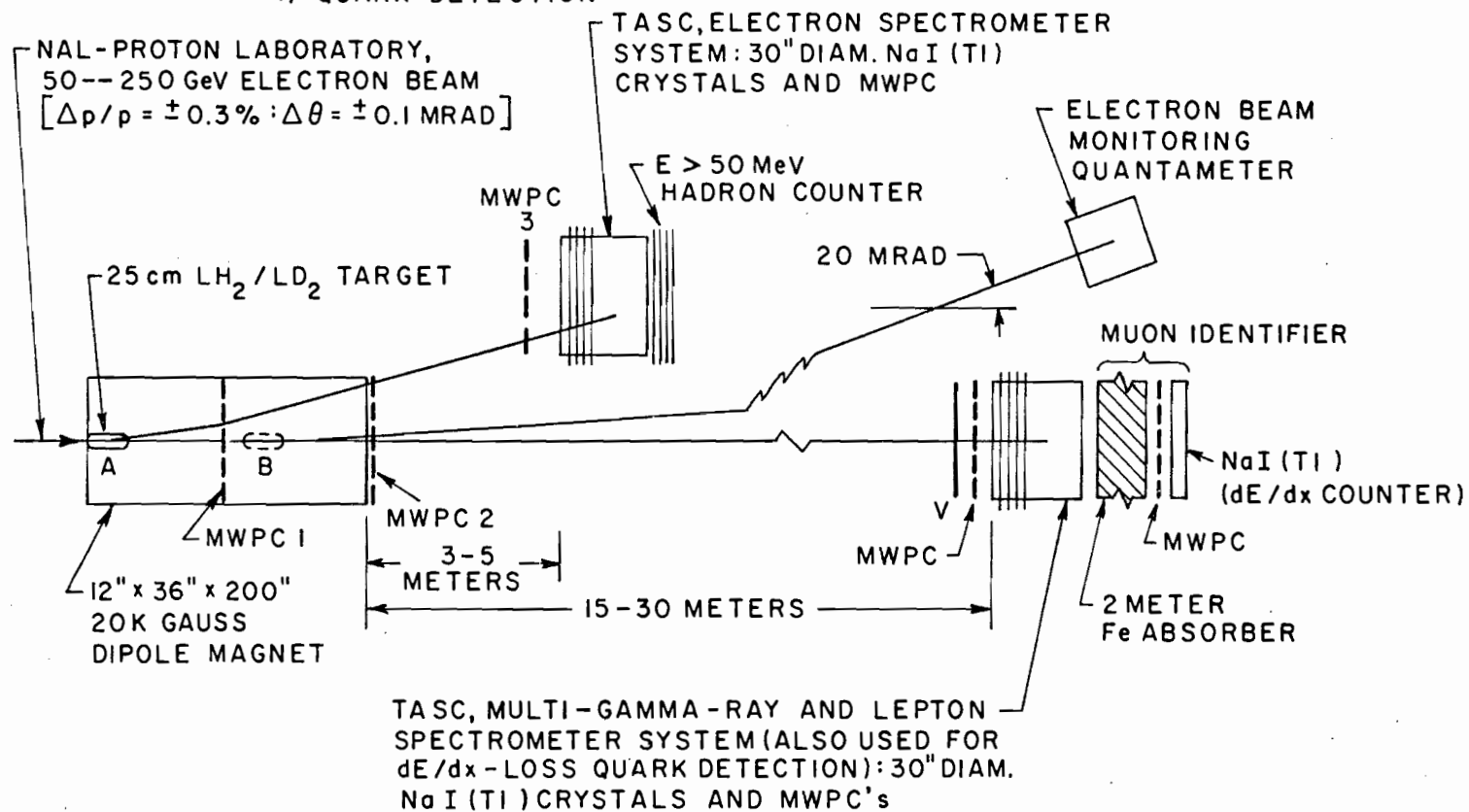
Using these as building blocks, we have devised specific spectrometer configurations which favor in each case the observation of a few processes among several ongoing reactions. In our original proposal 164, the design principles, the function of individual components and the qualities of spectrometer modules were described in detail. We have modified the composition of spectrometer modules to include muon identifiers. Thus, a modified and improved spectrometer is now obtained which has the capability of observing multi-gamma-ray or multi-lepton final states.

In Fig. 19 the first configuration is shown. This is designed for the purpose of observing the processes mentioned therein. In this and other configurations, the experimental target is placed inside the magnet. It is desired 1) to achieve a large acceptance in production angles and in momenta and also 2) to provide good resolution in the measurements of angles and momenta. These economical and efficient spectrometer features are made possible only by

CONFIGURATION ①

DESIGNED FOR FOUR FUNCTIONS

- 1) DEEP INELASTIC ELECTRON SCATTERING
- 2) ELECTRON-MULTI-GAMMA-RAY COINCIDENCE
- 3) TRIDENTS WITH LARGE MASS TIME-LIKE VIRTUAL PHOTONS
- 4) QUARK DETECTION



SCHEMATIC EXPERIMENTAL SETUP

(NOT TO SCALE)

Figure 19

(a)

PHI/ZPI IN PERCENT
ACCEPTANCE OF MAGNET/NAI(TL) CRYSTAL/MWPC COMBINATION.
SCATTERING ANGLE THETA (MRAD)
MOMENTUM (GEV/C) 8.0 16.0 24.0 32.1 40.1 48.1 56.1 64.1 72.1 80.2 88.2 96.2 104.2 112.2 120.2 128.3 136.3 144.3 152.3 160.3

11.0	7	5	9	7	7	6	9	8	10	9	7	8	7	4	5	3	4	1	3	0
21.0	100	99	94	87	87	83	48	22	7	6	2	0	0	0	0	0	0	0	0	0
31.0	100	100	99	92	75	57	38	30	22	15	1	0	0	0	0	0	0	0	0	0
41.0	100	97	80	62	55	43	38	33	21	24	10	8	0	0	0	0	0	0	0	0
51.0	98	71	50	48	47	41	40	30	24	25	20	18	2	0	0	0	0	0	0	0
61.0	76	57	49	32	46	35	31	28	28	23	18	18	3	0	0	0	0	0	0	0
71.0	38	42	50	33	46	33	28	35	26	20	21	15	8	8	0	0	0	0	0	0
81.0	12	32	38	30	39	30	27	31	26	20	18	22	12	11	0	0	0	0	0	0
91.0	5	35	37	36	33	35	32	33	25	24	21	18	15	11	0	0	0	0	0	0
101.0	0	25	31	33	32	36	27	29	25	21	18	16	18	11	0	0	0	0	0	0
111.0	0	15	33	30	30	33	25	31	24	24	18	15	14	11	0	0	0	0	0	0
121.0	0	11	32	29	30	32	29	27	23	19	24	17	16	9	0	0	0	0	0	0
131.0	0	9	29	30	30	29	31	28	27	23	20	17	17	10	7	0	0	0	0	0
141.0	0	8	32	25	34	27	34	29	18	21	19	16	17	7	10	0	0	0	0	0
151.0	0	8	31	23	33	27	40	29	25	19	17	18	13	9	13	0	0	0	0	0

INITIAL EVENTS=100000 FINAL EVENTS= 15819

0.0	3.000	3.000	0.0	0.150	0.150	0.457	0.457													
1.000	0.325	0.0	0.0	151.000	-1.000	0.0	20.000													
0.15233	0.15233	0.15233	0.05000	0.05000	0.05000	0.01192	0.0	0.16033	0.06364	0.45364	0.0									

Table IV

(b)

PHI/ZPI IN PERCENT
ACCEPTANCE OF MAGNET/NAI(TL) CRYSTAL/MWPC COMBINATION.
SCATTERING ANGLE THETA (MRAD)
MOMENTUM (GEV/C) 9.6 19.2 28.5 38.5 48.1 57.7 67.3 77.0 86.6 96.2 105.8 115.4 125.1 134.7 144.3 153.9 163.5 173.2 182.8 192.4

11.0	26	24	16	15	14	11	7	8	2	3	3	2	2	0	2	0	0	0	1	0
21.0	56	66	75	64	41	18	17	7	0	0	0	0	0	0	0	0	0	0	0	0
31.0	10	20	25	36	32	23	30	20	9	16	0	0	0	0	0	0	0	0	0	0
41.0	0	0	8	24	21	22	26	17	16	21	4	3	0	0	0	0	0	0	0	0
51.0	0	0	0	3	18	14	19	12	16	23	7	17	0	0	0	0	0	0	0	0
61.0	0	0	0	0	15	20	14	15	19	20	7	9	0	0	0	0	0	0	0	0
71.0	0	0	0	0	10	14	14	19	16	17	9	17	0	0	0	0	0	0	0	0
81.0	0	0	0	0	15	11	14	18	14	16	10	14	1	2	0	0	0	0	0	0
91.0	0	0	0	0	3	4	11	13	23	10	17	12	6	5	0	0	0	0	0	0
101.0	0	0	0	0	0	6	14	13	20	11	16	7	10	4	0	0	0	0	0	0
111.0	0	0	0	0	0	9	16	11	27	11	17	7	14	6	0	0	0	0	0	0
121.0	0	0	0	0	0	9	19	15	24	13	20	6	16	5	0	0	0	0	0	0
131.0	0	0	0	0	0	8	10	15	19	12	18	4	19	2	0	0	0	0	0	0
141.0	0	0	0	0	0	7	12	20	16	10	21	6	14	0	0	0	0	0	0	0
151.0	0	0	0	0	0	11	9	18	12	14	17	6	16	0	0	0	0	0	0	0

INITIAL EVENTS=100000 FINAL EVENTS= 7364

0.0	2.500	5.000	0.0	0.150	0.150	0.457	0.457													
1.000	0.325	0.300	0.0	151.000	-1.000	0.0	20.000													
0.18280	0.18280	0.18280	0.06000	0.06000	0.06000	0.00993	0.0	0.19239	0.07209	0.76209	0.0									

having an incident beam spot size of dimensions no greater than ± 2 mm. This spot size quality is achieved with the beam in our design. In the bending plane, the transverse coordinate of track origins is anchored by the beam spot size definition. Three other coordinates are measured on charged particle tracks by multiwire proportional chambers. The orbit of tracks is defined with a long lever arm, as shown in this figure.

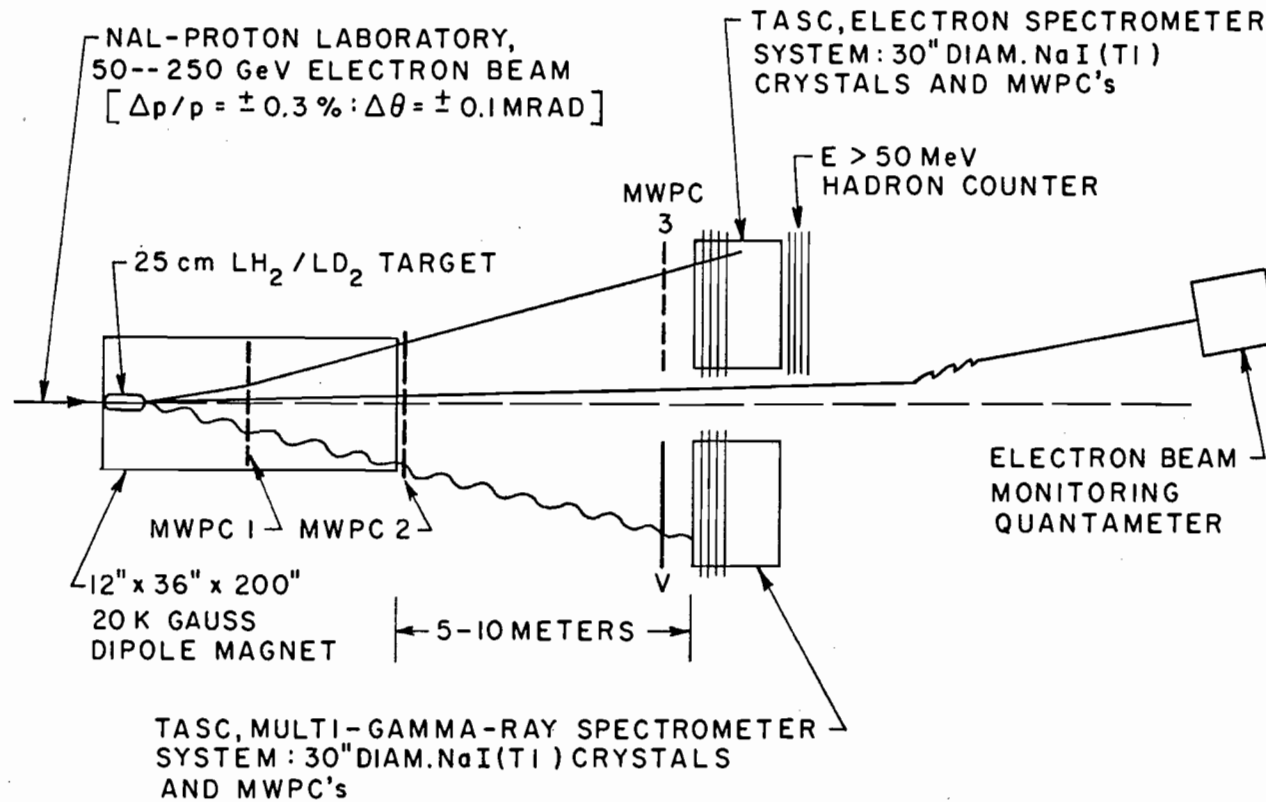
In Table IV the results of Monte Carlo acceptance calculations are shown for two spectrometer module locations. It is clear that by changing the target position inside the analyzing magnet and by setting the spectrometer modules at various locations several acceptance regions are defined selectively. We have used a Monte Carlo program to map out extensively the acceptance regions of the spectrometer system and to define those regions which are of interest to the physics considerations. In terms of the correlated quantities p and θ (momentum and production angle of produced particles) the acceptance calculations are given in bins of p and θ . The percentage of azimuthal angle accepted in a cell defined by Δp and $\Delta\theta$ is stated. The cases in Table IV (a) and (b) apply to the spectrometer module settings for the observation of deep inelastic scattered electrons. The other spectrometer arm is positioned to observe the production of forward going gamma-rays or leptons in coincidence with scattered electrons. This and the following tables are generated for the case of an incident beam of 150 GeV/c.

The second configuration shown in Fig. 20 differs from the first primarily only in the setting of one of the spectrometer arms. In this case, the second arm is moved away from the forward position,

CONFIGURATION II

DESIGNED FOR TWO FUNCTIONS

- 1) DEEP INELASTIC ELECTRON SCATTERING
- 2) WIDE ANGLE BREMSSTRAHLUNG



SCHEMATIC EXPERIMENTAL SETUP

(NOT TO SCALE)

Figure 20

(a)

PHI/2PI IN PERCENT
 ACCEPTANCE OF MAGNET/NAI(TL) CRYSTAL/MWPC COMBINATION
 MOMENTUM SCATTERING ANGLE THETA (MRAD)
 (GEV/C) 4.8 9.6 14.4 19.2 24.0 28.8 33.7 38.5 43.3 48.1 52.9 57.7 62.5 67.3 72.1 77.0 81.8 86.6 91.4 96.2

11.0	0	0	0	0	8	14	25	19	19	20	21	17	17	15	14	8	11	0	0	0
21.0	0	0	0	0	7	17	27	19	20	20	21	17	17	15	14	8	9	0	0	0
31.0	0	0	0	0	7	16	24	17	22	22	21	17	17	15	13	10	10	0	0	0
41.0	0	0	0	0	9	14	25	15	22	22	21	17	17	15	14	12	8	0	0	0
51.0	0	0	0	0	12	16	24	17	23	22	21	17	17	15	14	11	9	0	0	0
61.0	0	0	0	0	10	20	14	19	22	22	21	17	17	15	13	12	5	0	0	0
71.0	0	0	0	0	14	20	11	24	21	21	21	17	17	15	14	12	6	0	0	0
81.0	0	0	0	0	13	22	13	26	18	21	21	17	17	15	14	12	5	0	0	0
91.0	0	0	0	0	17	17	20	27	21	21	21	17	17	15	14	12	2	0	0	0
101.0	0	0	0	1	14	15	16	25	22	20	21	17	17	15	14	12	0	1	0	0
111.0	0	0	0	0	17	13	14	25	23	20	21	17	17	15	14	11	1	5	0	0
121.0	0	0	0	0	13	16	22	25	21	21	21	17	17	15	14	10	5	4	0	0
131.0	0	0	0	0	11	15	22	20	22	22	21	17	17	15	14	10	7	5	0	0
141.0	0	0	0	0	2	13	22	21	23	20	21	17	17	15	14	10	9	2	0	0
151.0	0	0	0	0	6	16	25	20	21	21	21	17	17	15	14	6	11	1	0	0

INITIAL EVENTS=100000 FINAL EVENTS= 11025

0.0	5.000	5.000	0.0	0.150	0.150	0.457	0.0			
1.000	0.325	0.0	0.0	151.000	1.000	0.0	0.0			
0.09140	0.09140	0.0	0.03000	0.03000	0.03000	0.0	0.0			
							0.09620	0.01000	-0.51400	0.0

Table V

(b)

PHI/2PI IN PERCENT
 ACCEPTANCE OF MAGNET/NAI(TL) CRYSTAL/MWPC COMBINATION.
 MOMENTUM SCATTERING ANGLE THETA (MRAD)
 (GEV/C) 4.8 9.6 14.4 19.2 24.0 28.9 33.7 38.5 43.3 48.1 52.9 57.7 62.5 67.3 72.1 77.0 81.8 86.6 91.4 96.2

11.0	0	0	0	0	0	0	0	0	0	0	0	0	0	0	0	0	0	0	0	0
21.0	0	0	0	0	1	1	1	5	3	6	6	10	8	7	9	7	9	5	6	1
31.0	48	51	47	41	42	35	34	27	22	24	18	16	9	7	4	0	1	0	0	0
41.0	100	100	100	97	89	75	44	24	10	4	0	0	0	0	0	0	0	0	0	0
51.0	100	100	100	100	98	85	52	17	2	0	0	0	0	0	0	0	0	0	0	0
61.0	100	100	100	91	66	58	43	32	27	14	0	0	0	0	0	0	0	0	0	0
71.0	100	100	87	67	51	44	39	32	25	21	10	3	0	0	0	0	0	0	0	0
81.0	100	90	68	57	47	34	38	29	25	22	21	12	0	0	0	0	0	0	0	0
91.0	95	65	49	53	48	28	31	31	25	23	20	14	1	0	0	0	0	0	0	0
101.0	75	55	43	41	43	30	32	31	27	25	24	14	12	3	0	0	0	0	0	0
111.0	28	47	38	39	41	32	32	31	25	21	17	15	17	6	0	0	0	0	0	0
121.0	9	33	29	33	36	32	33	27	29	25	21	19	18	6	0	0	0	0	0	0
131.0	0	20	29	35	32	26	32	34	24	20	19	20	20	5	0	0	0	0	0	0
141.0	0	11	32	27	33	34	38	33	25	23	21	17	16	5	8	0	0	0	0	0
151.0	0	8	28	23	33	24	34	28	26	18	22	20	15	10	11	0	0	0	0	0

INITIAL EVENTS=100000 FINAL EVENTS= 20888

0.0	5.000	5.000	0.0	0.150	0.150	0.457	0.457			
1.000	0.325	0.0	0.0	151.000	-1.000	0.0	20.000			
0.09140	0.09140	0.09140	0.03000	0.03000	0.03000	0.01987	0.0			
							0.09620	0.15901	0.54901	0.0

and is set to one side, such that wide angle gamma-rays can be observed in coincidence with scattered electrons. In Table V (a) the acceptance of gamma-rays in this spectrometer module is displayed. Table V (b) shows the acceptance of charged particles in a spectrometer module placed symmetrically, as it is seen in Fig. 20.

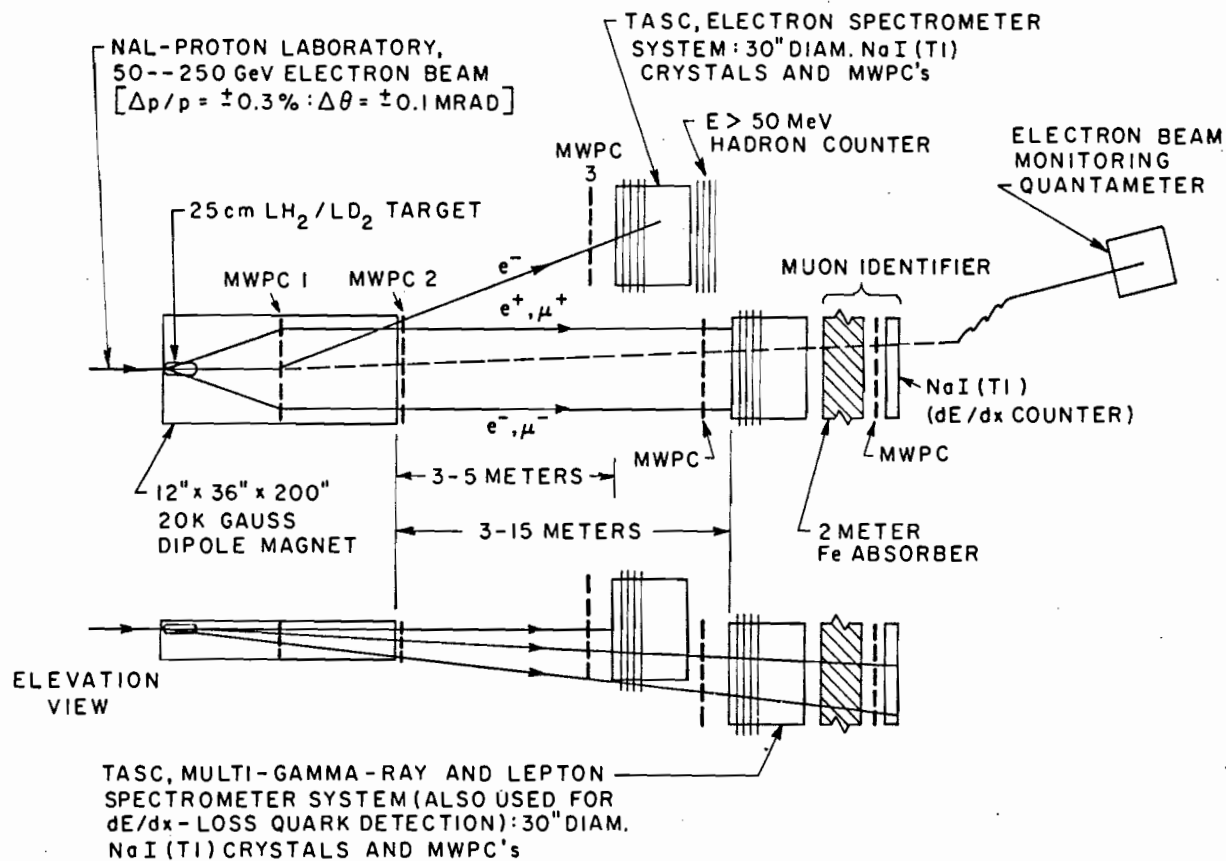
The third configuration differs from the previous ones in two ways. 1) The beam line and target position are displaced vertically inside the magnet (for example, the magnet is lowered by about 6 inches). 2) One of the spectrometer modules is placed in the forward direction, below beam line and the other is set on beam line and to one side. This configuration provides the following benefits: a) it restricts the acceptance of scattered electrons to small angles, such that these electron in fact signal the production of high energy real or virtual photons and tag the energy of these photons; b) irrespective of this point, it increases the acceptance of a spectrometer module which is placed in the forward direction and below beam line. Thus, the observation of high energy and large angle lepton production is enhanced. Low energy charged particles are not seen by the forward spectrometer arm. These features are demonstrated in Fig. 21 and in Table VI.

Configuration III is designed for the physics interests which are stated in Fig. 21. In Table VI (a) the acceptance of the forward spectrometer is depicted for positively charged particles, emerging at large angles and with high energies from the target. Table VI (b) is the same for negatively charged particles. It is seen that both positively and negatively charged particles, emerging at large angles and with high energies, are accepted symmetrically and equally as well. The

CONFIGURATION III

DESIGNED FOR FOUR FUNCTIONS

- 1) HEAVY LEPTON AND INTERMEDIATE BOSON SEARCH
- 2) HEAVY PHOTON AND NEUTRAL LEPTON SEARCH
- 3) SMALL ANGLE INELASTIC ELECTRON SCATTERING
- 4) ELECTRON TRIDENTS



SCHEMATIC EXPERIMENTAL SETUP

(NOT TO SCALE)

Figure 21

(a)

PHI/2PI IN PERCENT
ACCEPTANCE OF MAGNET/NAI(TL) CRYSTAL/MWPC COMBINATION.
MOMENTUM SCATTERING ANGLE THETA (MRAD)

(GEV/C)	5.2	10.4	15.6	20.8	26.0	31.3	36.5	41.7	46.9	52.1	57.3	62.5	67.7	72.9	78.1	83.3	88.6	93.8	99.0	104.2	
11.0	0	0	0	0	0	0	0	0	0	0	0	0	0	0	0	0	0	0	0	0	0
21.0	0	0	0	0	0	0	0	0	0	0	0	0	0	0	0	0	0	0	1	0	0
31.0	0	0	0	0	0	0	0	0	0	0	4	0	7	3	10	4	7	9	0	0	1
41.0	0	0	0	0	0	0	0	1	14	4	22	7	16	7	13	6	8	6	0	1	1
51.0	0	0	0	0	0	3	15	12	17	12	24	7	14	6	11	4	3	3	0	0	0
61.0	0	0	0	0	6	14	15	23	13	20	24	7	16	1	10	2	0	0	0	0	0
71.0	0	0	0	6	13	25	15	26	14	26	20	6	16	0	7	0	0	0	0	0	0
81.0	0	0	0	8	20	30	15	34	18	21	18	4	17	0	2	0	0	0	0	0	0
91.0	0	0	0	14	21	30	17	34	13	26	13	2	10	0	0	0	0	0	0	0	0
101.0	0	0	8	21	20	34	19	40	15	27	15	2	10	0	0	0	0	0	0	0	0
111.0	0	0	13	22	24	30	20	35	13	26	11	3	9	0	0	0	0	0	0	0	0
121.0	0	0	19	26	30	26	21	33	14	34	9	7	5	0	0	0	0	0	0	0	0
131.0	0	3	25	22	29	27	22	37	14	33	8	6	4	0	0	0	0	0	0	0	0
141.0	0	4	28	22	33	25	28	27	17	28	5	9	3	0	0	0	0	0	0	0	0
151.0	0	6	25	22	34	21	31	25	24	27	4	9	1	0	0	0	0	0	0	0	0

INITIAL EVENTS=100000 FINAL EVENTS= 7769

0.0	5.000	5.000	0.0	0.250	0.050	0.457	0.457														
1.000	0.325	0.0	0.0	151.000	1.300	0.0	20.000														
0.09140	0.09140	0.09140	0.05000	0.05000	0.01000	0.01987	0.0	0.10418	0.15901	0.0											-0.380

Table VI

(b)

PHI/2PI IN PERCENT
ACCEPTANCE OF MAGNET/NAI(TL) CRYSTAL/MWPC COMBINATION.
MOMENTUM SCATTERING ANGLE THETA (MRAD)

(GEV/C)	5.2	10.4	15.6	20.8	26.0	31.3	36.5	41.7	46.9	52.1	57.3	62.5	67.7	72.9	78.1	83.3	88.6	93.8	99.0	104.2	
11.0	0	0	0	0	0	0	0	0	0	0	0	0	0	0	0	0	0	0	0	0	0
21.0	0	0	0	0	0	0	0	0	0	0	0	0	0	0	0	0	0	0	1	1	0
31.0	0	0	0	0	0	0	0	0	0	0	4	1	5	9	3	15	0	7	0	0	0
41.0	0	0	0	0	0	0	0	2	12	3	23	9	16	13	5	14	0	12	0	0	0
51.0	0	0	0	0	0	6	5	14	17	16	23	7	19	7	9	5	0	5	0	0	0
61.0	0	0	0	0	5	21	21	18	23	16	22	7	15	2	9	0	0	0	0	0	0
71.0	0	0	0	0	14	19	19	15	29	17	17	9	14	0	7	0	0	0	0	0	0
81.0	0	0	0	5	13	31	19	29	25	16	10	14	9	0	4	0	0	0	0	0	0
91.0	0	0	4	14	15	36	15	33	15	18	7	19	3	2	0	0	0	0	0	0	0
101.0	0	0	7	25	19	33	15	37	17	28	3	15	0	1	0	0	0	0	0	0	0
111.0	0	0	19	19	24	32	23	33	17	30	8	14	0	1	0	0	0	0	0	0	0
121.0	0	0	19	21	28	24	28	29	19	28	13	10	0	1	0	0	0	0	0	0	0
131.0	0	1	23	17	37	23	29	24	23	24	14	3	0	2	0	0	0	0	0	0	0
141.0	0	0	19	23	33	18	31	24	25	20	15	2	2	0	0	0	0	0	0	0	0
151.0	0	1	18	24	36	19	35	17	30	15	14	0	1	0	0	0	0	0	0	0	0

INITIAL EVENTS=100000 FINAL EVENTS= 7687

0.0	5.000	5.000	0.0	0.250	0.050	0.457	0.457														
1.000	0.325	0.0	0.0	151.000	-1.000	0.0	20.000														
0.09140	0.09140	0.09140	0.05000	0.05000	0.01000	0.01987	0.0	0.10418	0.15901	0.0											-0.380

Monte Carlo calculation of Table VI is made with the target placed just at the entrance of the analyzing magnet. The forward spectrometer is assumed to be set 5 meters away from the magnet exit. It is clear that larger angles and higher momenta can be accepted by moving the target position forward and/or moving the forward spectrometer arm further away.

Thus, a versatile facility is provided at NAL by our modular configurations.

1. Detection of Showers Induced by Electrons and Gamma-Rays

The spectrometer modules, in both our pion and electron experiments, are designed a) to observe several individual showers induced by electrons and gamma-rays, b) to provide a high rejection factor for hadrons and c) to observe and identify muons. Briefly, the detection system is based on the addition of multi-wire proportional chambers (MWPC), having unique encoding and readout properties, to large NaI(^{Tl}) crystals which are segmented in an especial arrangement.

We demonstrate the results of our recent tests and continuing development effort on MWPC's with electromagnetic delay line readout. Multi-tapped delay lines are used with fixed (5 - 10 nsec delay per tap) time delays between each chamber wire pairs. An intercepted shower induces signals over several wires. The overall sum signal of a shower propagates to the end of the delay line with a chosen and fixed speed (20 - 40 nsec/cm). These signals describe the shape of intercepted showers. They contain information on the space location of showers and shower electron multiplicities. In Fig. 22 the shape of 10 GeV electron induced showers is shown at several shower depth positions.

10 GeV ELECTRON SHOWERS
 ENCODED BY MWPC DELAY LINE AT 40 nsec/cm

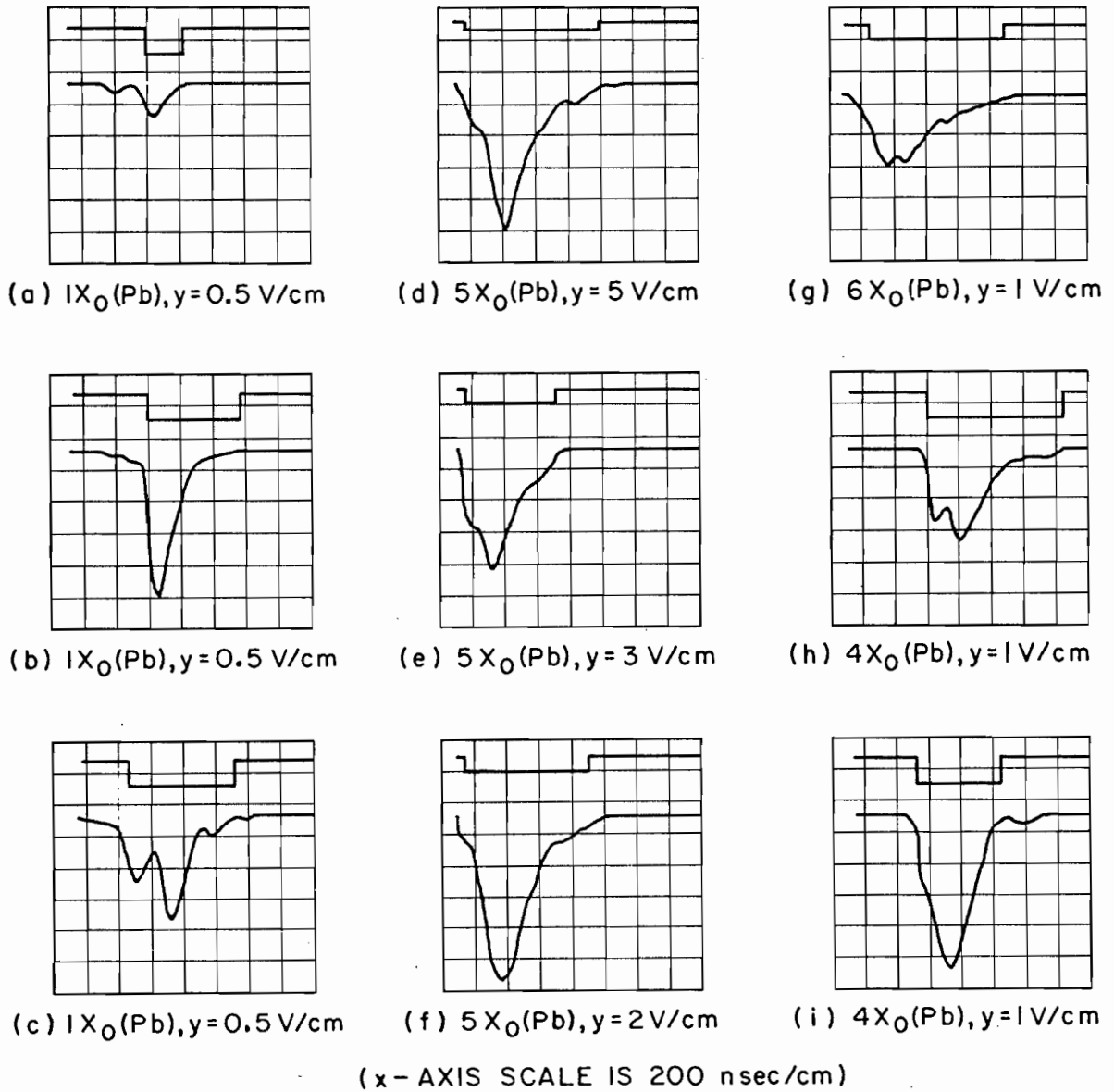


Figure 22

In Fig. 22 (a,b,c) the individual signals are induced by electron showers generated by $1 X_0$ (radiation length) of lead. The statistical fluctuations in shower multiplicities are evident in these representative samples. At 10 GeV the showers reach the maximum electron multiplicities in lead at about $5 X_0$. These are depicted in Fig. 22 (d,e,f). A shower signal with $6 X_0$ Pb is shown in Fig. 22(g) and those with $4 X_0$ Pb are in Fig. 22 (h,i). Several thousands of individual showers were observed in recent tests at SLAC. These signals are encoded with an electronics system which measures both the position of the center-of-charge and the amount of total charge. Both analog and digital information are made available by the electronics. The regions of individual shower signals are defined by time-over-threshold discriminator gates. These are also shown above in Fig. 22.

These results make it convincing that our continuing development effort will be successful in producing a working system for the observation of multi-gamma-ray and multi-lepton final states at NAL. The pair resolution of induced signals, up to $10-12 X_0$ shower depths, is limited only by the natural widths of showers. At NAL energies these widths are narrowing (2-3 cm) and the electron multiplicities in showers are increasing (several hundreds of electrons at shower maxima). Therefore, the task of observing multi-gamma-ray and multi-lepton final states in a single large detector becomes easier at NAL than in the above tests carried out at SLAC.

2. Muon Identifiers

Muon identifiers will be included in our spectrometer modules. These are necessary in both of our electron and pion experiments.

A simple muon identification method will be used, based on the total absorption of hadrons and electromagnetic showers: 30 radiation lengths of NaI(Tl) crystals and about 10 pion collision length of iron. The attenuation length of pions in iron is measured⁽³¹⁾ to be 21 cm so that a 2 meter iron absorber is sufficient to attenuate hadrons down [together with about 4 collision lengths in NaI(Tl)] to a level of below 10^{-6} . Muons are transmitted through the overall spectrometer module thickness and suffer ionization energy loss. Their trajectories are displaced by Coulomb multiple scattering. The energy loss is 2.7 GeV and the rms displacement of trajectories is about 0.4 cm for 50 GeV muons. The source of muon production is well defined by the small target volume and the small spot size of the incident beam.

Multi-wire proportional chambers are placed before and after the iron absorber. A 2 inch thick scintillator element is the last detector in the spectrometer modules. This is used to observe the average ionization energy loss signal of transmitted particles. Thus, muons are identified and their trajectory is measured by the muon identifier elements shown in the figures of the experiment configurations.

3. Errors

Well known formalisms and precise computations are used to arrive at the measurement uncertainties in our spectrometer configurations. The total errors are estimated for the determination of momentum p and production angle θ of produced charged particles. These errors are due to space coordinate measuring accuracy and Coulomb multiple scattering. In space coordinate measurements, conservatively a 0.5 mm uncertainty is assumed for each of the MWPC planes. The dominant

effect due to beam spot size is also investigated. These are very relevant to our experiment for the spectrometer configurations we have discussed.

We demonstrate the improvement obtained with small beam spot size, in the accuracy of p and θ measurements. In Fig. 23 the total uncertainty in momentum measurements is shown, as a function of p , using the ± 2 mm spot size of our proposed beam. Also shown is the result with a ± 12 mm beam spot size which is representative of another beam. The measurement method is pictorially demonstrated in the insert of this figure. Similarly in Fig. 24, the total uncertainty in scattering angle measurements is shown, as a function of p . Both p and θ measurements and errors are correlated. In this figure, the improvement derived from a small beam spot size definition is evident.

We argue that improvements in errors are made possible because additional information is available in our experimental spectrometer configurations. The new information comes from the precise energy determination in the case of electrons (and also gamma-rays). The information is obtained from the observed pulse heights from signals induced in the NaI(Tl) crystals of our spectrometer modules. During the analysis phase of our experiments, produced charged particles are grouped in selected momentum bins. Momentum bin sizes are set by the above uncertainties for $\Delta p/p$. For each momentum bin, the spectrum of pulse heights from the NaI(Tl) crystals is examined. As we already know, each spectrum will show a clear and separated electron peak. Thus, electrons are identified. Moreover,

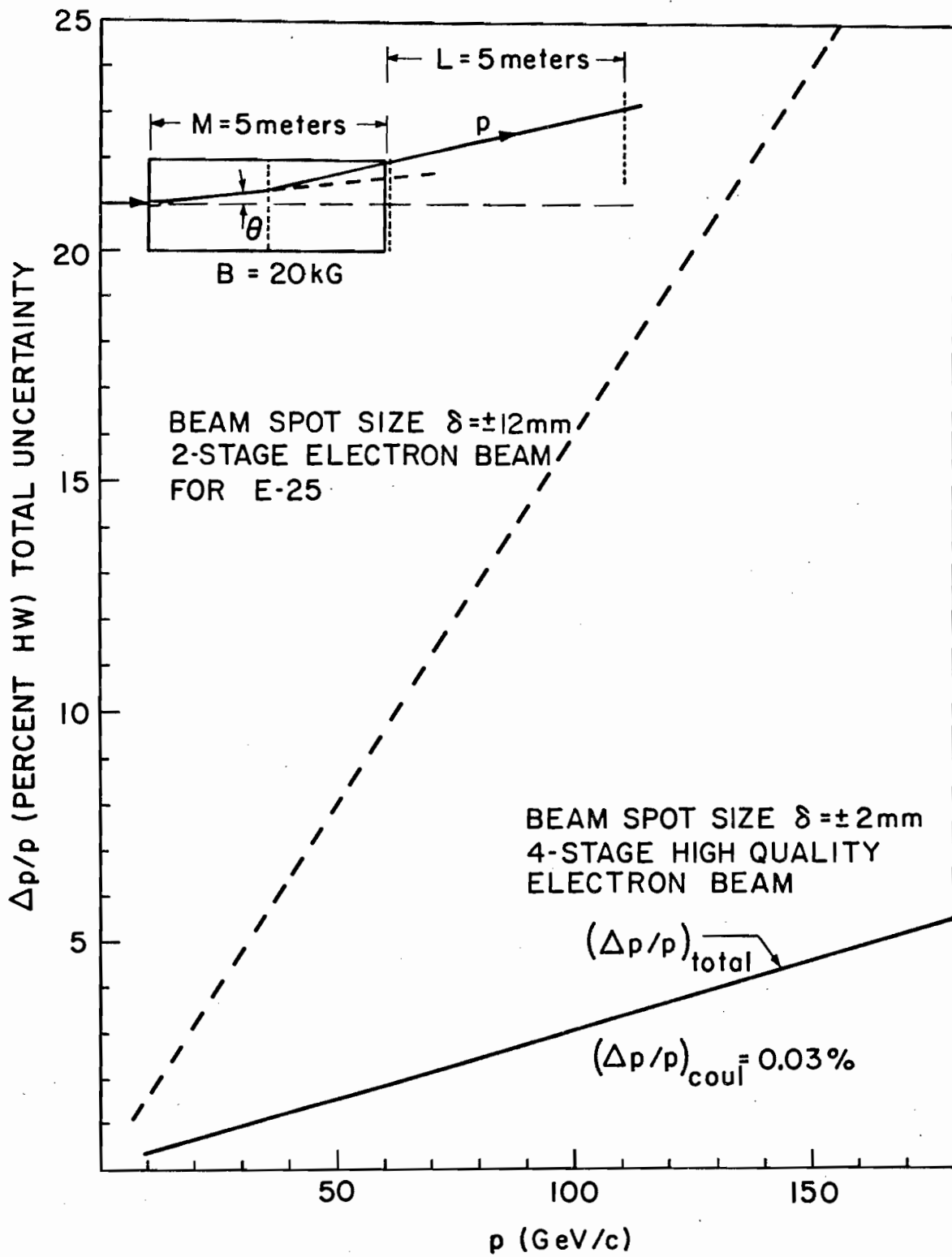


Figure 23

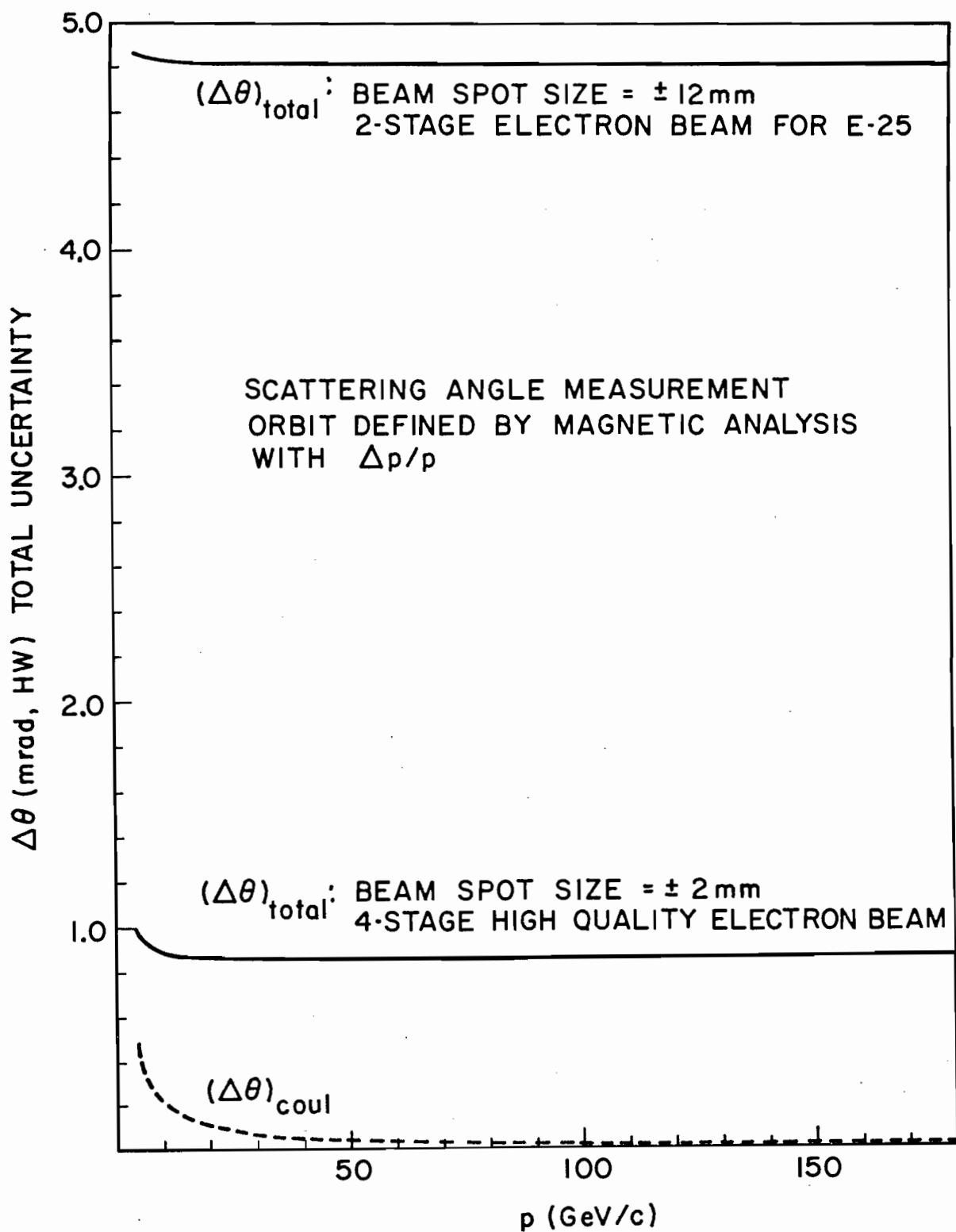
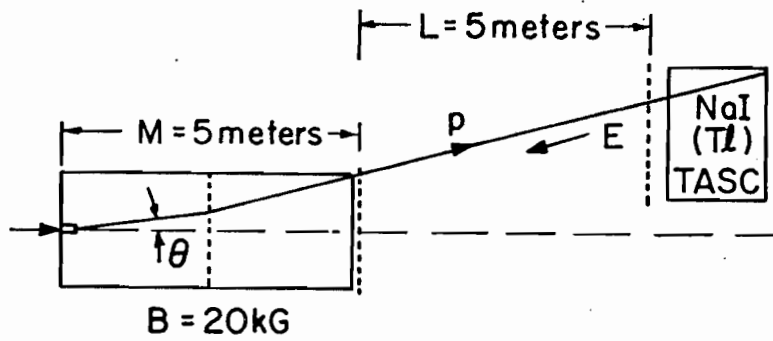


Figure 24

a precise energy measurement is now available from the observed pulse height values. Using this precise energy measurement of identified electrons we will improve the errors in θ by means of the well known (E, θ) correlations. This improvement is demonstrated in Fig. 25. Therefore, in the case of observed electrons in our spectrometer modules, the final error in θ , will be $\Delta\theta \simeq 0.1$ mrad. The same error values also apply for gamma-rays. In this case there are no (p, θ) correlations and the θ_γ errors are determined only by space coordinate uncertainties.

Finally, the resulting uncertainties in the quantities Q^2 and W are calculated. These are shown in Fig. 26. An average of 1% uncertainty will be found in Q^2 and W in our proposed experiment.



SCATTERING ANGLE MEASUREMENT

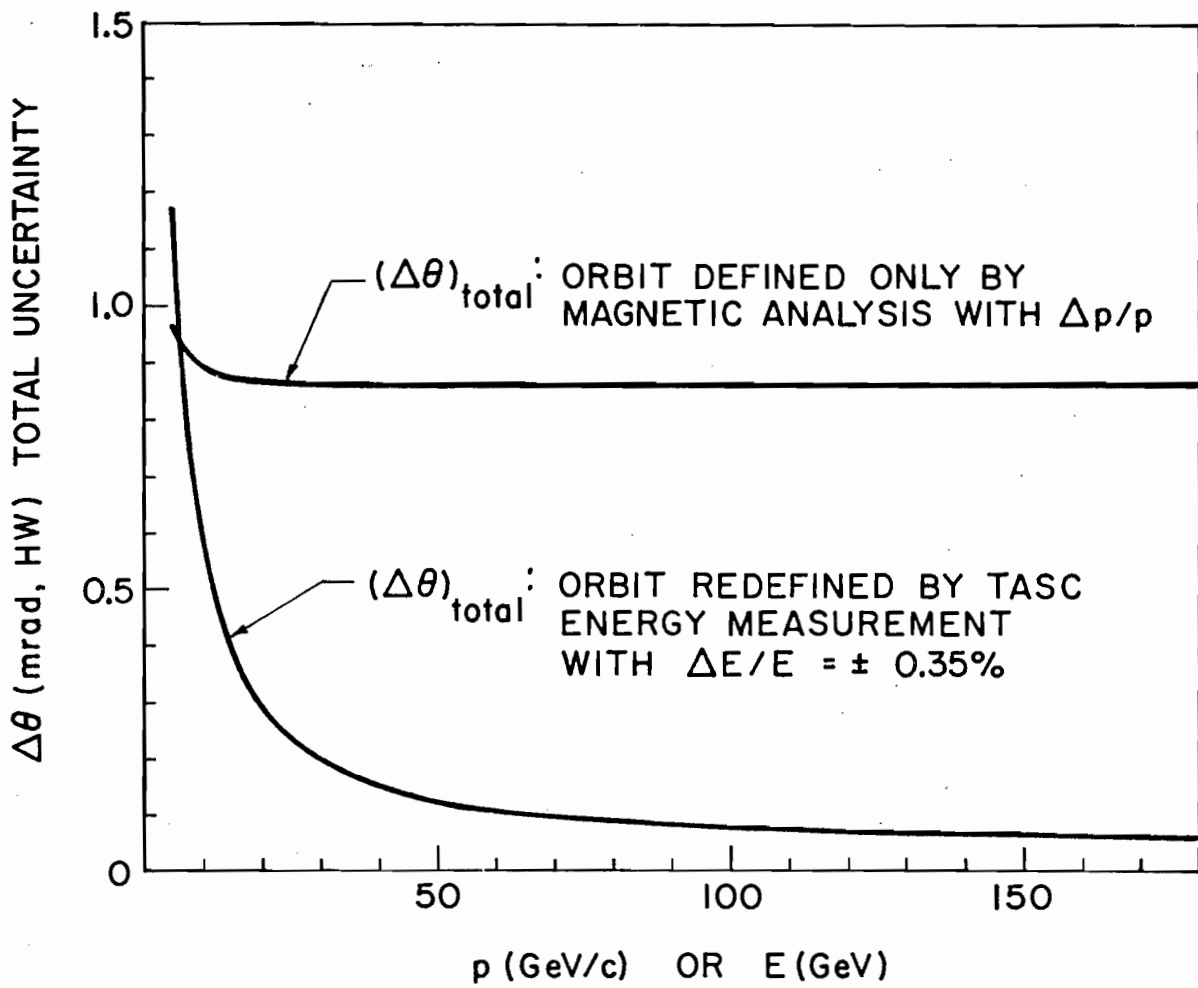


Figure 25

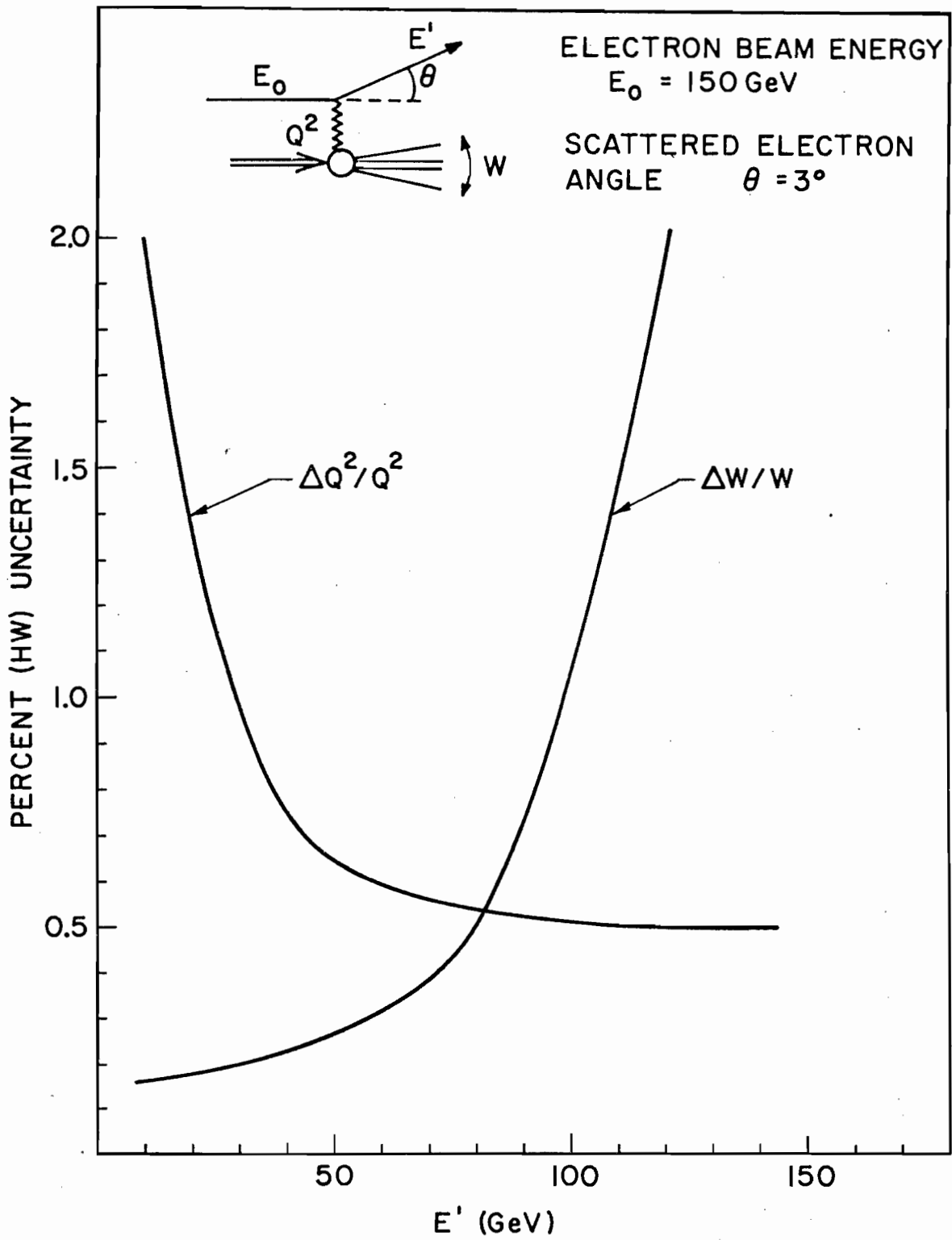


Figure 26

SUMMARY OF PROPOSAL REQUIREMENTS

1. This experiment requires no more than an external proton beam of 10^{12} protons/pulse incident on a secondary beam Be target.
2. 2200 hours of running time are required to complete the physics planned for this proposal. An additional 200 hours of equivalent beam time is estimated, for the purposes of experiment setup and equipment checkout, during a period of 2 months.
3. To accomplish the proposal goals, the group of experimenters making this proposal will be augmented by three postdoctoral physicists and several graduate students. Other interested physicists are invited to join the group as collaborators.
4. The experimental equipment designated in this proposal requires a development and preparation time of a minimum of 20-22 months. Due to the commonality of experimental equipment in both the proposed electron and pion experiments, this preparation time will suffice for both proposals.
5. Other desired requirements to implement this experiment are discussed in the proposal. These are connected with beams at NAL and the cryogenic system for our targets and a superconducting magnet.

REFERENCES

1. T. W. Aitken, R. W. Clifft and E. Gabathuler, "A High Intensity Muon Beam Design for CERN II", Report No. DNPL/P 131, Daresbury July 1972.
2. a) R. W. Brown, A. K. Mann and J. Smith, Phys. Rev. Lett. 25, 257 (1970); b) R. W. Brown and J. Smith, Phys. Rev. D3, 207, (1971); c) R. W. Brown, R. H. Hobbs and J. Smith, Phys. Rev. D4, 794 (1971).
3. Particle Physics With Positron-Electron-Proton Colliding Beams,(PEP) Report No. SLAC-146/LBL-750, April 1972.
4. K. O. Mikaelian, Phys. Rev. D5, 70 (1972).
5. H. W. Fearing, M. Pratap and J. Smith, Phys. Rev. D5, 177 (1972).
6. F. A. Berends, G. B. West, Phys. Rev. D1, 122 (1970) and Phys. Rev. D3, 262 (1971). A more complete calculation is given by:
H. W. Fearing, M. Pratap and J. Smith, Phys. Rev. D5, 158 (1972).
7. Kwang Je Kim and Yung-Su Tsai: a) Phys. Letters 40B, 665 (1972), b) SLAC - PUB - 1105 (September 1972), c) SLAC - PUB - 1106 (September 1972) to be published in Rev. Mod. Phys. See also d) Yung-Su Tsai, Phys. Rev. D4, 2821 (1971).
8. The real photon flux is obtained from eq. (IV. 14) of reference 7(b). The virtual photon flux is obtained by first calculating an angle θ_{\max} , derived by E' and the low Q^2 limit and evaluating the equivalent radiator formula $N(E, E', \theta_{\max})$. This formula can be found as eq. (3.10) of reference 9.

9. S. J. Brodsky, T. Kinoshita and M. Terazawa, Phys. Rev. D4, 1532 (1971).

$$\begin{aligned}
 N(\omega) &= \frac{\alpha}{2\pi^2} (2\pi) \int_{-1}^1 d\cos\theta' \frac{2\omega^2 E'}{E} \left(\frac{1}{k^2}\right)^2 \left(-\frac{1}{2}k^2 + \frac{E^2 E'^2}{k^2} \sin^2\theta'\right) \\
 &= \frac{\alpha}{\pi} \left[\frac{E^2 + E'^2}{E^2} \left(\ln \frac{E}{m_e} - \frac{1}{2}\right) + \frac{(E - E')^2}{2E^2} \left(\ln \frac{2E'}{E - E'} + 1\right) + \frac{(E + E')^2}{2E^2} \ln \frac{2E'}{E + E'} \right] \\
 N(\omega, \theta_{\max}) &= \frac{\alpha}{\pi} \left[\frac{E^2 + E'^2}{E^2} \left(\ln \frac{E \theta_{\max}}{2m_e} - \frac{1}{2}\right) \right. \\
 &\quad \left. + \frac{(E - E')^2}{2E^2} \left(\ln \frac{2E'}{E - E'} + 1\right) \right. \\
 &\quad \left. + \frac{(E + E')^2}{2E^2} \ln \frac{2E'}{[(E - E')^2 + EE' \theta_{\max}^2]^{1/2}} \right],
 \end{aligned}$$

10. a) Martin L. Perl, SLAC - PUB - 1062 (July 1972); see also
 b) M. L. Perl; PHYSICS TODAY, 24/7,34 (1971); and c) SLAC-PUB-982 (November 1971); d) T. J. Braunstein, W. L. Lakin, F. Martin, M. L. Perl, W. T. Toner, T. F. Zipf, Phys. Rev. D6, 106 (1972).
11. J. D. Bjorken and C. M. Llewellyn Smith, SLAC - PUB - 1107 (September 1972) to be published in Phys. Rev.
12. Description and Physics Program of the Proposed Recirculating Linear Accelerator (RLA), SLAC-139 (Revised) February 1972.
13. S. M. Berman, J. D. Bjorken and J. B. Kogut, Phys. Rev. D4, 3388 (1971).
14. J. B. Kogut, Phys. Rev. D5, 1152 (1972).
15. G. Miller, E. D. Bloom, G. Buschhorn, D. H. Coward, H. DeStaebler, J. Drees, C. L. Jordan, L. W. Mo, R. E. Taylor, J. I. Friedman, G. C. Hartmann, H. W. Kendall and R. Verdier, Phys. Rev. D5, 528 (1972).

16. a) T. D. Lee and G. C. Wick, Phys. Rev. D2, 1033 (1970); D3, 1046 (1971); b) T. D. Lee, Phys. Rev. Letts. 25, 1144 (1970); c) T. D. Lee, Phys. Rev. Letts. 26, 801 (1971) and Physics Today, 25/4, 23 (1972); see also d) P. M. Fishbane and J. D. Sullivan, Phys. Rev. D4, 2516 (1971) and D6, 1813 (1972).
17. a) S. Weinberg, Phys. Rev. Letts. 19, 1264 (1967); and 27, 1688 (1971); b) S. Weinberg, Phys. Rev. D5, 1412 (1972); and D5, 1962 (1972).
18. W. B. Atwood and G. B. West, SLAC-PUB-1081 (August 1972), to be published in Phys. Rev.
19. A. Bodek, M. Breidenbach, D. L. Dubin, J. E. Elias, J. I. Friedman, H. W. Kendall, J. S. Poucher, E. M. Riordan, M. R. Sogard and D. H. Coward. M. R. Sogard presentation at the XVI International Conference on High Energy Physics, Chicago-NAL September 1972.
20. S. J. Brodsky, private communication and PEP-NOTE-15 (1972), see also reference 9, (above) Fig. 4.
21. Theoretical considerations of the trident process are made in a) J. D. Bjorken and M. C. Chen, Phys. Rev. 154, 1335 (1967); b) G. R. Henry, Phys. Rev. 154, 1534 (1967); c) D. C. Ehn and G. R. Henry, Phys. Rev. 162, 1722 (1967).
22. Experimental considerations and calculations of the trident process are discussed in a) S. J. Brodsky and S. C. C. Ting, 145, 1018 (1966); b) M. J. Tannenbaum 167, 1308 (1968); c) L. M. Lederman and M. J. Tannenbaum in Advances in Particle Physics, vol I, edited by R. L. Cool and R. E. Marshak (Interscience Publishers, New York), 1968.

23. J. J. Russell, R. C. Sah, M. J. Tannenbaum, W. E. Cleland, D. G. Ryan and D. G. Stairs, Phys. Rev. Letts. 26, 46 (1971).
24. a) R. Linsker, CO-3067(2)-2, Columbia University (preprint) 1972;
b) R. Linsker, Phys. Rev. D5, 1709 (1972); and c) Phys. Rev. Letts. 27, 167 (1971).
25. F. E. Low, Phys. Rev. Letts. 14, 238 (1965).
26. a) S. J. Brodsky, J. F. Gunion and R. L. Jaffe, SLAC-PUB-1064 (July 1972), to be published in Phys. Rev.; b) S. J. Brodsky, F. E. Close and J. F. Gunion, Phys. Rev. D6, 177 (1972); and c) Phys. Rev. D5, 1384 (1972).
27. M. Bott-Bodenhausen, D. O. Caldwell, C. W. Fabjan, C. R. Gruhn, L. S. Peak, L. S. Rochester, F. Sauli, U. Stierlin, R. Tirler, B. Weinstein and Z. Zahniser, Phys. Letters, 40B, 693, (1972).
28. Yung-Su Tsai, "Radiative corrections to electron scattering," SLAC-PUB-848 (January 1971), to be published in Electron Scattering and Nuclear Structure, edited by B. Bosco (Gordon and Breach, N.Y.). This paper contains better and improved derivations of radiative corrections to electron scattering, including the effects of straggling due to the bremsstrahlung emission, the ionization loss and the Landau straggling of electrons.
29. We have used a computer program, originally formulated by L. W. Mo based on reference 30, and modified by Y. S. Tsai incorporating the improvements in reference 28.
30. L. W. Mo and Y. S. Tsai, Rev. Mod. Physics 41, 205 (1969).
31. F. A. Harris, S. I. Parker, V. Z. Petersen, D. E. Yount, and M. L. Stevenson, Nucl. Inst. Meth. 103, 345 (1972).

(To be submitted to Nucl. Instr.
and Methods)

HEPL 677

NAL-75

OCTOBER, 1972

Appendix

I

A HIGH QUALITY ELECTRON/PHOTON BEAM FOR NAL^{*}

Z. G. T. Guiragossian and R. E. Rand

High Energy Physics Laboratory

W. W. Hansen Laboratories of Physics

Stanford University

Stanford, California 94305

* Work supported by the National Science Foundation, Grant No. GP 28299

ABSTRACT

A design for a secondary electron beam suitable for electron scattering experiments at the National Accelerator Laboratory is presented. Using standard NAL beam transport magnets it will operate at up to 300 GeV/c with the following properties: Acceptance 9.5 μ ster $\% \Delta p/p$ (FW), momentum bite $\pm 2\%$, momentum resolution of momentum hodoscope $\Delta p/p = \pm 0.30\%$ (HW at base), final spot size $\leq \pm 3.0 \text{ mm} \times \pm 5.5 \text{ mm}$ (HW at base). Hodoscopes are also included for measuring the angles at which electrons pass through the experimental target with resolutions in both planes of better than $\pm 0.1 \text{ mr}$. These properties are achieved by a periodic beam structure which includes correction of second order aberrations by means of sextupoles. The yield of electrons is estimated to be $\sim 10^8/10^{13}$ incident protons when the energy of the electrons is about one half the energy of the protons. It is emphasized that synchrotron radiation by electrons in the beam transport magnets is very significant in reducing pion contamination of the final beam spot. It is shown that superconducting magnets to enhance this effect are superfluous. Pion impurity is $\leq 0.01\%$ at every energy and may be made essentially zero at energies greater than 160 GeV. The beam is designed with four focussing stages, the first two of which provide a beam spot of sufficient quality for tagged photon experiments.

I. INTRODUCTION

The electron scattering experiments proposed¹⁾ at the National Accelerator Laboratory require an electron beam of high purity with very fine energy and angular resolution. At the same time it is important that these qualities are not achieved at the expense of electron intensity, a valuable commodity at NAL. The beam must also be compatible with providing a tagged photon facility for which the electron beam specification is not so stringent. It has been suggested²⁾ that to meet these requirements, the beam should be constructed in two phases, the first of which (2 stages) would provide the photon beam while the second phase (total 4 stages) would constitute the high quality electron beam. The present design meets these requirements which are translated into quantitative terms in section 2 and Table I. Figure 1 shows a schematic layout of the beam. The functions³⁾ of the 4 focussing stages are as follows:

(1) Electron production [protons produce π^0 's in primary target of low Z material: Be or deuterium, (Be is used for practical reasons), sweeping magnets remove protons and other charged particles from neutral stage of beam; photons from π^0 decays pair-produce electrons in a high Z radiator, (Pb or U)], primary defining apertures, horizontally (x) dispersed focus (F1) to define momentum bite cleanly, vertical (y) focus ($F\frac{1}{2}$) with slit to reduce π^- contamination. (The primary target is the virtual object of the beam optics.)

(2) Magnet after F1 to clean up beam, achromatic focus at F2. This focus is used for the tagged photon beam (Phase I) or with a horizontal slit to further eliminate pions in the 4 stage beam (Phase II).

(3) Dispersed focus at F3 with momentum hodoscope.

(4) Angle hodoscopes at first foci of last set of quadrupoles.

These measure directly the angles (θ horiz., ϕ vert.) at which an electron passes through the experimental target located at the achromatic focus F4.

The beam is designed for a maximum momentum of 300 GeV/c. Careful attention was paid to the desirability of using standard NAL transport magnets throughout. Components are described in Table II.

II. SPECIFICATION OF BEAM QUALITY

In order for the electron beam to be suitable for scattering experiments, it is essential that it meet the following specifications which result from a realistic assessment of the experimental requirements and possible beam performance.

(a) Beam intensity of $\sim 10^8$ electrons/pulse from 10^{12} - 10^{13} incident protons, requiring⁴⁾ an acceptance of at least 8 μ ster % $\Delta p/p$ (full width). In practice this means $\Delta p/p \simeq 4\%$ (FW) and $\Delta \Omega \simeq 2 \mu$ sterad.

(b) Maximum momentum 300 GeV/c.

(c) Well defined momentum bite, i.e. momentum resolution at the first dispersed focus (F1), $\Delta p/p \leq \pm 0.5\%$ at base of distribution.

(d) Momentum resolution at third focus (F3), $\Delta p/p \leq \pm 0.3\%$ at base of distribution.

(e) Momentum hodoscope at F3 to take full advantage of this resolution.

(f) Angle measuring hodoscopes (both planes) in the last stage with a resolution of ≤ 0.1 mrad.

(g) Achromatic beam spot at final focus F4 $\leq \pm 2.5$ mm \times $\leq \pm 7.5$ mm at base of distribution.

(h) Low energy contamination (halo) of final beam spot $< 0.001 \%$.

(i) Electron purity: π/e ratio $\leq 3 \times 10^{-4}$ (Pions are produced by neutrons which interact in the Pb/U radiator). It is emphasized that electron purity is strongly influenced by the optical quality of the beam design, since electrons lose energy by synchrotron radiation throughout the beam transport system and thus may be separated from pions provided that the final beam spot is small and free from aberrations. μ/e ratio $\leq 10^{-6}$ (Muons from pion decay and other sources are transmitted mainly through the earth shielding of the beam which is about 5 meters below ground level).

(j) Suitable optics (achromatic beam spot and space which could accommodate the photon tagging apparatus at the second focus (F2)). Here the electron purity is not so critical and no beam hodoscopes are required before this point. The specification for a tagged photon beam has been discussed by Halliwell et al.⁵⁾

The following sections describe a design which meets this specification.

III. ELECTRON PRODUCTION

The design of a "front end" or electron production stage has been fully discussed elsewhere.⁵⁾ The parameters of this part of the beam are largely dictated by necessary functions and little freedom is available for variations in design. The main components are illustrated in the schematic layout, Fig. 1, and discussed below.

The angle of incidence of the proton beam at the primary target may be varied by a set of bending magnets. This enables one to use production angles other than 0° , so that, at the sacrifice of some intensity, one may

improve the final π/e ratio if at all necessary. The primary target itself should be of a material which maximises the ratio of π^0 production to photon attenuation. Deuterium is the optimum choice for this condition but for practical reasons would probably not be used. Beryllium is the most reasonable alternative. There is an optimum target thickness for which the maximum number of photons (from π^0) are produced. This thickness is ~ 1.13 interaction lengths for beryllium as shown below. The n/γ ratio (π^-/e ratio) decreases monotonically with target thickness but is expected to be sufficiently small at this optimum thickness.

An estimate of the electron yield to be expected is made as follows. Recent results from the ISR show⁶⁾ that the cross section for inclusive π^0 production from pp collisions is equal to the average of the cross sections for π^- and π^+ . The latter have been measured at BNL and CERN and are well described by a multiperipheral model.⁷⁾ This model has been used to calculate π^0 production and hence the electron yield to be expected.

The number of decay photons from π^0 's produced in the target is obtained by integrating:

$$\frac{dN_\gamma(k)}{dk d\Omega} = 2 \int_k^{P_0} \frac{T}{\lambda} \frac{\epsilon}{\sigma_a(pp)} \frac{d\tau_{\pi^0}}{dp_{\pi^0} d\Omega} \frac{dp_{\pi^0}}{P_{\pi^0}}$$

where T = target length,

λ = hadronic interaction length in the target

$$\epsilon = \frac{1}{T} \left[\frac{\exp\left(-\frac{7}{9} \frac{T}{x_0}\right) - \exp\left(-\frac{T}{\lambda}\right)}{\frac{1}{\lambda} - \frac{7}{9} \frac{1}{x_0}} \right] \quad \text{is an effective target efficiency,}$$

x_0 = radiation length in the target
 $\sigma_a(pp)$ = 31 mb⁸⁾ (absorption cross section)
 p_0, p_{π^0} = proton and π^0 momenta

and the differential cross section is obtained from

$$\frac{d\sigma_{\pi^0}}{dp_{\pi^0} d\Omega} = \frac{1}{2} \left[\frac{d\sigma_{\pi^-}}{dp d\Omega} + \frac{d\sigma_{\pi^+}}{dp d\Omega} \right]$$

The target efficiency is maximised at an optimum target length of $\frac{T}{\lambda} = \frac{c}{c-1} \ln c$, where $c = \frac{9}{7} \frac{x_0}{\lambda}$. Using the measured⁹⁾ value of $\lambda = 35.7$ cm for beryllium and $x_0 = 35.7$ cm, one obtains $\frac{T}{\lambda} = 1.13$, i.e. $T = 40.3$ cm.

This formula gives an exact energy spectrum for the photons because of the isotropic decay distribution in the π^0 center of mass. But the angular distribution of photons is approximate since only the π^0 production angle is included. The approximation is good to angles of order $\frac{m_{\pi^0}}{E_{\pi^0}}$. It is assumed that production of photons by other processes is negligible.

Between the primary and secondary targets a set of 4 bending magnets (13.1 m \times 14 kg) separate the protons and other charged particles from the neutral components of the beam. This is sufficient to handle primary momenta up to 500 GeV/c. The proton beam is dumped in the vicinity of the first electron beam quadrupole, below the beam line level.

The second target or radiator consists of a high Z material such as lead or uranium which has a high ratio of collision length to radiation length. Elsewhere⁵⁾ it has been shown by a Monte Carlo calculation

that the optimum thickness for the radiator is approximately 0.5 radiation lengths. The yield of electrons is now obtained from the approximate formula.¹⁰⁾

$$\frac{dN_e(p)}{dp d\Omega} \approx \left[1 - \exp \left(- \frac{7}{9} \cdot \frac{\ell}{x_0} \right) \right] \int_p^{p_0} \frac{dN_\gamma(k)}{dk d\Omega} \frac{dk}{k}$$

where ℓ is the radiator thickness.

The position of the secondary target or radiator is not critical but should be as close to the primary target as possible. This will minimise the effective source size at the primary target, due to multiple scattering of electrons in the radiator. A primary to secondary target separation of 22.8 m is chosen.

In Figs. 2(a) - 2(e) are shown the calculated electron yields for the present beam design and for primary proton momenta of 200, 300, 400 500 and 1000 GeV/c respectively. The dependence of the yield on production angle is also shown. It is evident that the energy of the primary proton beam is a more important factor than the intensity. For example, 10^{12} protons/pulse at 400 GeV/c produce more high energy electrons than 10^{13} protons/pulse at 200 GeV/c.

IV. ELECTRON BEAM OPTICS

It would be impossible to meet the specifications detailed in section II without correcting the main chromatic aberrations in the beam. Any beam design of this length (600 m) and moderately large acceptance, with magnetic elements of no higher order than quadrupole, would be expected to suffer from second order chromatic aberrations of several times first order effects. From the start, the beam optics were designed therefore to be compatible with sextupole correction of second order terms.

This feature is essential to the proposed electron scattering experiments for without it, it would not be possible to achieve the necessary momentum and angular resolutions and especially the small spot size and high electron purity. The latter parameter is directly affected by the size of the electron beam envelope at F2 where a horizontal collimator is used to define a pion spot. This feature is important not only because it removes pions from the beam at F2, but because it enhances the π -e separation at F4, caused by synchrotron radiation by electrons in the beam bending magnets.

Experience has shown that sextupole magnets can only be successfully used in a beam line by locating them as optically conjugate pairs with equal strengths, i.e. the transfer matrix between the sextupoles must be identically \pm unity. This ensures that even order geometrical aberrations introduced by the sextupoles cancel outside the pairs. Sextupole pairs cannot be interlaced without introducing serious third order aberrations. For each pair, the strength can be chosen to cancel exactly only one second order chromatic aberration of the beam. (Higher multipole magnets are not considered here). These conditions imply that the number of stages between fully corrected foci in a beam line must be at least two for correction in one plane and three for both planes. Exact correction of the electron beam is not therefore possible, but the following acceptable compromise has been attained. The design is based on the exact correction of the main chromatic aberration term $\langle x | x'_0 \varepsilon \rangle^{11}$ in the horizontal bending plane (x) at F2 and F4. This is done in such a way that the geometric aberrations (mainly $\langle x | x'_0 x'_0 \rangle$ inevitably introduced at F1 and F3) are tolerable. Worsening of the chromatic aberration in y is avoided by locating the sextupoles at y foci where they have negligible effect. A small spot size in y at each x focus (between the true y foci) is obtained by locating an angle

focus waist ($\langle y|y_0 \rangle = \langle y'|y'_0 \rangle = 0$) at these positions. This arrangement also ensures that chromatic aberrations in y at all x foci are negligible. (There are aberrations in y' however).

The first y focus, where pions are removed from the beam, is therefore inside the first stage ($F \frac{1}{2}$) where chromatic aberrations are small. Location of the sextupole pairs at conjugate points requires that the beam-structure be periodic from $F \frac{1}{2}$ to $F3 \frac{1}{2}$. However, the design of the first quadrupole doublet need not form part of this structure and has been chosen to produce a magnification in the first stage of 2.4 in x and 3.0 in y . This increases the acceptance of the periodic part of the beam and enables one to use a reasonable focal length for the quadrupoles (24.4m). It also helps to reduce the geometric aberration introduced by the first sextupole at $F1$ and the third at $F3$. Similarly the last half of the last stage ($F3 \frac{1}{2} - F4$) does not form part of the periodic structure and is designed purely to obtain the required beam spot size and to provide suitable locations for the θ and ϕ hodoscopes.

At the sextupoles the dispersions $\langle x|\delta \rangle$ are equal and optimized so that $\langle x|x'_0 \rangle > x'_0$ is just less than $2 \langle x|\delta \rangle \delta$ where $\delta \equiv \Delta p/p$. This ensures that the acceptance is maximized, the sextupole strength is minimised and that the geometric aberrations at $F1$ and $F3$ are much less than the original chromatic aberrations at $F2$ and $F4$. This condition also implies, however, that $\langle x|x'_0 \rangle > x'_0$ is only 2/3 of the available aperture. Hence the use of sextupoles inevitably leads to a reduction in acceptance. This arrangement is also a compromise between correcting $\langle x|x'_0 \delta \rangle$ at $F1$ and $F3$ (which requires $\langle x|\delta \rangle$ at the odd sextupoles greater than $\langle x|\delta \rangle$ at the even ones) and correcting $\langle x|\delta \delta \rangle$ at $F2$ and $F4$ (which requires the

opposite). Even so these terms are not significant.

Magnet positions and strengths were calculated using the computer program TRANSPORT¹²⁾. Rays were traced through the final system, using the program TURTLE¹³⁾ to evaluate the performance of the beam transport and the effect of synchrotron radiation by electrons. The performance which appears to satisfy all electron scattering and tagged photon experiment requirements is shown in Table I. Also shown there are the electron yields calculated both by the method outlined in section III and by a Monte Carlo calculation¹⁴⁾ based on the Hagedorn-Ranft model. π/e ratios are also based on this model, but depend strongly on the effects of synchrotron radiation described in section V. Magnetic components of the beam are listed in Table II.

Figure 3 shows the layout of the beam, the TRANSPORT matrix elements and beam envelopes.

Figures 4-9 show TURTLE generated histograms at the various foci both with and without sextupole correction. These results are correct to all orders in the optics. Calculations were performed with an effective primary electron spot size of ± 2.5 mm in both planes, the value expected at 100 GeV/c. The main effect contributing to this spot size is multiple scattering in the radiator. A primary aperture slit of $x = \pm 15$ mm and $y = \pm 30$ mm at the first quadrupole is used in all calculations. However the acceptance ($9.5 \mu\text{ster } \% \Delta p/p \text{ FW}$) quoted in Table I is for a y slit of ± 37.5 mm. The only effect of this larger slit is to increase the vertical spot sizes at F2 and F4 proportionally. It causes no significant change in beam losses or purity.

Imperfections in the quadrupole fields as found in actual measurements¹⁵⁾ were included in the ray tracing calculations by using a higher order multipole expansion. It is interesting to note that in this type of periodic beam structure, such imperfections have virtually no effect because of cancellations at conjugate lens positions.

Figure 4 shows the vertical beam profile at the first y focus where a slit is used to effect the primary removal of pions from the beam. Pions, which are generated mostly by neutrons in the lead radiator, are produced with a much greater spread of angles than are electrons so that the effective pion spot size at the primary target is much larger than that for electrons as shown in Table I. The π/e ratio in the whole beam may therefore be improved by locating "scrapers" or slits at the x and y foci. The π/e ratio at F2 quoted in Table I is the value obtained after vertical scraping at $F \frac{1}{2}$, only. Horizontal slits at F2 serve to further improve this ratio at F4 as described in section V. Very few electrons are lost at these scrapers.

The momentum resolution and acceptance at the first dispersed focus F1 are shown in Fig. 5. Here the slight asymmetry of the beam profiles due to the geometric aberrations introduced by the single sextupole SX1 may be seen. The resolution is sufficient to ensure a very sharp cutoff of the momentum spectrum.

Figure 6 shows the beam profiles at the achromatic focus F2 where tagged photon experiments may be performed. Sextupole correction of the chromatic aberrations at this point is seen to be essential to the subsequent properties of the beam. In the region of F2, the beam envelope (with quadrupoles 11 and 12 omitted) is confined to ± 12.5 mm in both dimensions over a length of 50 m at 100 GeV/c. At higher momenta it is narrower still. This condition

is adequate for several tagged photon experiments.¹⁶⁾ More complex spot requirements¹⁷⁾ have been obtained by the addition of two extra quadrupoles on either side of bending magnets 11 and 12.

The momentum resolution at F3 is shown in Fig. 7. This may be slightly improved by an appropriate slit at F2 as shown in Table I without significant loss of intensity. The centroid displacement for the rays of nominal momentum (p_0) is due mainly to the transport matrix element $\langle x | x'_0 \ x'_0 \rangle$ while at $1.016 p_0$ additional effects due to $\langle x | \delta\delta \rangle$ are seen. This implies that the momentum hodoscope calibration will not be exactly linear.

The angular resolutions at the angle hodoscopes are shown in Fig. 8 and numerically in Table I. In spite of the impossibility of placing the θ hodoscope where the dispersion is exactly zero and the ϕ hodoscope exactly at the appropriate focus, the intrinsic angular resolutions are easily adequate for the experimental requirements. Greater spread is introduced by the finite size of the hodoscope elements (section VI).

Finally Figs. 9 and 10 show the electron and pion beam profiles at F4 where the experimental target will be located. The spot sizes easily satisfy the experimental requirements. The separation of the electron and pion beam spots by synchrotron radiation is discussed below (section V).

An important property in a secondary electron beam is cleanness in momentum. That is, it should not be possible for a significant number of electrons with momenta outside the nominal limits to pass through the experimental beam spots at F2 and F4. The periodic beam structure described here performs well in this respect. Between F1 and F2, only 0.3% of the electrons are lost. Furthermore, it is impossible for electrons of momenta

less than $0.865 p_0$ to pass through the beam spot at F2. In stage 4, losses only occur (inevitably) at the hodoscope. In each case it is possible to place a veto shower counter where it may detect photons radiated by an electron in the hodoscope elements as discussed in section VI.

V. ELECTRON BEAM PURITY AND SYNCHROTRON RADIATION

The permissible level of pion contamination of the electron beam is determined primarily by the pion rejection capability of the experimental electron detectors. A secondary consideration is that in a 25 cm liquid hydrogen target for instance, 1.4% of all interacting pions would produce electrons via π^0 production followed by $\pi^0 \rightarrow \gamma\gamma$ and $\gamma \rightarrow e^+e^-$. These electrons are produced mainly at low energies and do not constitute a significant background.

The electron detectors¹⁾ under development in this laboratory consist of several large NaI(Tl) crystals interleaved with multi-wire proportional chambers. Tests with these detectors have shown that at 10 GeV, the probability of a pion being identified as an electron is $< 0.3\%$ if the momentum is known to 3% . There is reason to expect this uncertainty to drop to 0.1% at NAL energies. Now the ratio of the total cross sections for π^-p to e^-p interactions is typically 10^3 . Hence the probability of confusing a hadron from a π^- interaction, with a scattered electron is conservatively 0.09% for a π/e contamination ratio of 3×10^{-4} . Such a systematic error is certainly less than other experimental errors, systematic or statistical. The numbers in Tables I and III show that such an electron purity is attainable in the present beam design at the final focus F4. At F2, however, the pion contamination is unacceptable. The same would be true in a 4-stage beam not corrected for second order aberrations.

The flux of pions which remains within the electron beam spot at F4 depends on several factors, the most important of which are production mechanisms at the primary target, beam optics and synchrotron radiation. It has not been generally realized that this last effect - synchrotron radiation of electrons in the conventional beam bending magnets - is very significant.

This may be seen as follows. The fractional loss in momentum of an electron of energy $E(\text{GeV})$ passing through a uniform magnetic field $B(\text{kgauss})$ of length L (meters) is given by

$$\frac{\Delta p}{p} = 1.26 \times 10^{-8} E B^2 L$$

Hence for a 200 GeV electron in a field of 14 kgauss of length 3.05 m, $\Delta p/p = 0.15\%$. This is a small effect but the deviation due to this momentum loss is $4.8 \mu\text{rad}$. Again this is a small angle but in each phase of the beam there are about 10 magnets with an average lever arm of ~ 100 m. Hence if the magnet settings are not compensated for this effect, the electron beam spot will be shifted ~ 5 mm, more than the total spot size. If however the magnet settings are "radiation compensated" as in Table II, the electron beam spot will be on axis with a separate pion beam spot off axis by ~ 5 mm. Thus the pion contamination can be reduced almost to zero (Table III) by a suitable scraper or veto counter.

This effect is illustrated by the beam profiles in Fig. 10 which are due to exact ray tracing calculations using the program `TURTLE`.

(The momentum and deviation of each ray were suitably offset after each bending magnet.) In Fig. 10 all beam profile distributions are normalized arbitrarily to have equal heights. The magnet settings used were those shown in Table II. At energies less than 300 GeV, magnet settings within each group of magnets are optional provided the integral $\int B d\ell$ is correct and B does not exceed 14 kgauss. They have been chosen as follows. For energies greater than 200 GeV, it is sufficient to use a minimum number of the available magnets with power distributed equally between them, to achieve almost complete separation of pions and electrons. At lower energies the effect of synchrotron radiation may be optimised by using all available magnets with reversed fields where necessary so that the integral $\int B^2 d\ell$ is maximized but the beam line geometry is preserved. This procedure is illustrated at 100 and 150 GeV in Table II and Fig. 10. It provides a substantial reduction in pion contamination which would become zero at about 160 GeV.

Synchrotron radiation will also be responsible for some reduction in beam quality due to the statistical fluctuations of the process. It is estimated that these effects will cause an additional beam spot spread of ~ 0.5 mm at F4 at ~ 200 GeV and a momentum spread of $\sim 0.2\%$. Both of these figures make negligible contributions when folded quadratically with the respective geometrical values.

It has been suggested¹⁸⁾ that synchrotron radiation be used to enhance electron beam purity by placing a "chicane" of superconducting magnets at the intermediate focus of the beam (F2). Thus the electron momenta would be shifted by a large amount at this point and with the second phase of the beam tuned accordingly, pions could be eliminated. However it is now

seen that the distributed effect of synchrotron radiation along the beam line is sufficient to reduce pion contamination to an acceptable level in the present beam design and application.

The "chicane" thus appears to be of limited usefulness in this beam design. If, however, it is desired to produce a completely pure electron beam so that less discriminating detectors may be used in other experiments a superconducting chicane of 70 kgauss \times 3.2 m would shift the electron momenta $\sim 2\%$ at 100 GeV, sufficient to cause all pions to be lost at F3. The device would be redundant above 160 GeV.

A more economical way of enhancing the electron beam purity consists of filtering out the neutron and K^0 components at the neutral stage of the beam. This may be achieved by placing a liquid deuterium filter inside a bending magnet in front of the lead radiator. Such a filter 3.3 m long would remove 63% of the hadronic neutrals and transmit 72% of the photons. The pion contamination would thus be reduced by a factor of 2.0 to a level of $\pi/e \lesssim 10^{-5}$ at F4. The electron to hadron singles ratio in the detector would then be $\sim 100:1$. A beryllium primary target followed by a deuterium filter would appear to be a more economical arrangement than a simple deuterium primary target.

Muons produced by decay of pions, and other processes from the primary target may cause some contamination of the electron beam especially at F2. These high energy muons are transmitted mainly through the earth shielding of the underground beam line. Calculations¹⁹⁾ have shown however that in this design such contamination is negligible.

VI. BEAM INSTRUMENTATION

While specific details of beam instrumentation would be worked out under practical operating conditions, the general requirements may be defined as follows. Small high resolution multi-wire proportional chambers could be used at low intensities to obtain beam profiles at various locations during commissioning of the beam. At high intensities and during actual operation, these would be replaced by small traversing plastic scintillation counters, located especially at all x and y foci. Remotely controlled beam slits would be placed in front of the first quadrupole QP1 and at the foci: $F \frac{1}{2}$ and $F2$.

To define the momenta and angles of electrons passing through the experimental target at F4, 8 or 16 element plastic scintillator hodoscopes would be set up at the appropriate locations as shown in Fig. 3. At beam rates of $> 10^8$ /sec special timing techniques would be necessary in using these hodoscopes. It is suggested that selected events at the experiment itself could be used to generate a gate of about 10 nsec duration, during which the timing pulses from all hodoscope elements could be digitized in parallel. Currently available gated time digitizers have an inherent resolution of 400 psec. True coincidences would be recognized by means of an on-line computer.

Veto shower counters, to detect photons radiated by beam electrons at the p , θ and ϕ hodoscopes, should be placed next to the beam transport elements QP16, BM25 and QP20 respectively. These counters need not be large since it is only necessary, for instance, to detect photons of energy $k > 300$ MeV to maintain a momentum resolution of better than 0.3% at 100 GeV/c.

This mode of operation is possible since each hodoscope is followed by a bending magnet which sweeps the electron beam away from the veto counters. A "beam-halo" veto located just in front of F₄ would also be necessary especially to discriminate against pions. Other veto counters would be placed along the beam as necessary. Calculations indicate that the main veto counter rates would not exceed 1% of the beam rate.

Finally in the third and fourth stages, the beam design includes two drift spaces of about 40 meters each which can accommodate beam pipes instrumented to operate as low pressure threshold Cerenkov counters. These counters would serve the important function of monitoring the pion contamination of the electron beam. They would also be essential if the system were used as a high quality hadron beam.

VII. CONCLUSIONS

It has been demonstrated in detail that it is possible to produce a very high quality electron beam from the new generation of proton accelerators operating at 400 to 500 GeV. Electron fluxes of more than 10^8 /pulse with a beam spot only a few millimeters across are feasible. Furthermore, momenta and directions of the electrons passing through the target may be determined with good resolution and high beam purity is possible without special devices. Finally it should be pointed out that such a beam line will operate equally well for hadrons and will in fact constitute a very versatile facility.

VIII. ACKNOWLEDGEMENTS

The authors would like to thank the many people who have contributed to the successful completion of this design study. They are especially indebted to Dr. J. J. Murray and Professor D. D. Reeder who were their main inspiration. Thanks also are due to A. L. Read, K. L. Brown, T. Nash and D. Carey for many clarifying discussions and much practical help. Professor R. Hofstadter has provided much encouragement and guidance throughout this effort. Finally, the authors are grateful to Professor R. R. Wilson and Professor E. L. Goldwasser for their continuous interest and support.

TABLE I

ELECTRON BEAM PERFORMANCE

Optical properties are calculated using the program TURTLE.¹³⁾

Yield calculations are described in the text. See Figs. 3 - 9. (A 1 mm radius proton beam spot is assumed.)

Electron Beam Momentum	100 GeV/c	200 GeV/c	Experimental Requirements
Electrons: effective source size at F0	2.5 mm rad	1.5 mm rad	-
Pions: effective source size at F0	10.0 mm rad	8.7 mm rad	-
Acceptance: μ ster % $\Delta p/p$ FW	9.5	9.5	≥ 8
Electron Yield at F4/10 ¹³ p at 500 GeV/c			
Multiperipheral model:	6.2×10^8	1.9×10^8	10^8
Hagedorn-Ranft model:	2.2×10^8	0.47×10^8	
π/e ratio at F2	6.0×10^{-4}	1.2×10^{-3}	
π/e ratio at F4 ^(a)	1.0×10^{-4}	4.6×10^{-6}	3×10^{-4}
Momentum Bite at F1 (HW at base)	$\begin{cases} + 2.4\% \\ - 2.1\% \end{cases}$	$\begin{cases} + 2.4\% \\ - 2.1\% \end{cases}$	-
(HWHM)	$\begin{cases} + 2.2\% \\ - 1.9\% \end{cases}$	$\begin{cases} + 2.2\% \\ - 1.9\% \end{cases}$	$\pm 2\%$
Momentum Resolution at F1 (HW at base)	$\pm 0.39\%$	$\pm 0.30\%$	$\leq \pm 0.5\%$
Momentum Resolution at F3 (HW at base)	$\pm 0.30\%$ (± 5 mm slit at F2)	$\pm 0.26\%$ (± 4 mm slit at F2)	$\leq \pm 0.3\%$
Spot Size at F2 (HW base)	± 6.0 mm \times ± 8.5 mm	± 3.8 mm \times ± 8.5 mm	-
Spot Size at F4 (HW base)	± 3.0 mm \times ± 5.5 mm	± 2.0 mm \times ± 5.5 mm	$\leq \pm 2.5$ mm \times ± 7.5
θ Resolution at θ hodoscope (HWHM)	± 0.035 mr	± 0.035 mr	$\leq \pm 0.1$ mr
ϕ Resolution at ϕ hodoscope (HWHM)	± 0.027 mr	$< \pm 0.027$ mr	$\leq \pm 0.1$ mr

(a) Electron purity due to beam optics, production cross sections, and synchrotron radiation throughout the beam. See Table III for details.

TABLE II

BEAM LINE COMPONENTS AND MAGNET SETTINGS

The settings for electrons are Radiation Compensated. For electrons at 100 and 150 GeV/c, magnet settings are optimized to maximize ΣB^2 (with the limit $B \leq 14$ kgauss.).

All quadrupoles (QP): 3.81 cm rad \times 3.048 m long (NAL # 3-Q-120)
 All bending magnets (BM): 1.905 cm gap \times 3.048 m long (NAL # 5-1.5-120)
 All sextupoles (SX): 5.08 cm rad \times 0.762 m long (NAL # 4-S-30)

Component	Position Front End (m)	Field Values at Pole (kgauss)				
		300 GeV/c hadron beam	300 GeV/c electron beam	200 GeV/c electron beam	150 GeV/c electrons max ΣB^2	100 GeV/c electrons max ΣB^2
Radiator	22.8					
Aperture (± 15 mm \times 37.5 mm)	30.0					
QP1, 2	30.48	- 6.564	- 6.564	- 4.376	- 3.282	- 2.188
QP3,4	37.19	5.402	5.402	3.601	2.701	1.801
BM 1	55.32	10.792	10.763	7.189	- 3.204	- 6.799
BM 2	58.67	"	"	"	13.983	13.987
BM 3	62.03	"	"	"	"	"
BM 4	65.38	"	"	"	- 3.204	- 6.799
QP 5	94.49	2.451	2.438	1.632	1.223	0.816
Y Slit ($F \frac{1}{2}$) (± 9.0 mm)	97.84					
SX1	97.84	2.308	2.296	1.536	1.151	0.768
QP 6	118.87	- 5.297	- 5.269	- 3.526	- 2.642	- 1.763
F 1	167.64					
QP 7	167.64	5.297	5.269	3.526	2.642	1.763
BM 5	170.99	13.042	12.947	8.676	6.504	4.339
BM 6	174.35	"	"	"	"	"
QP 8	192.02	- 5.297	- 5.249	- 3.522	- 2.641	- 1.762
BM 7	230.73	12.025	11.885	7.989	13.940	12.973
BM 8	234.09	"	"	"	- 9.920	-13.958
BM 9	237.44	"	"	"	13.940	12.973
QP 9	240.79	5.297	5.223	3.517	2.634	1.759
SX 2	244.15	2.308	2.275	1.532	1.147	0.766
BM 10	245.21	12.025	11.845	7.981	5.978	3.992
QP 10	265.18	- 5.297	- 5.214	- 3.515	- 2.633	- 1.759
BM 11	278.74	14.000	13.748	9.390	6.957	4.647
BM 12	282.09	"	"	"	"	"
F 2 (γ expt)	313.94					

TABLE II (cont.)

BEAM LINE COMPONENTS AND MAGNET SETTINGS

The settings for electrons are Radiation Compensated. For electrons at 100 and 150 GeV/c, magnet settings are optimized to maximize ΣB^2 (with the limit $B \leq 14$ kgauss.).

All quadrupoles (QP): 3.81 cm rad \times 3.048 m long (NAL # 3-Q-120)
 All bending magnets (BM): 1.905 cm gap \times 3.048 m long (NAL # 5-1.5-120)
 All sextupoles (SX): 5.08 cm rad \times 0.762 m long (NAL # 4-S-30)

Component	Position Front End (m)	Field Values at Pole (kgauss)				
		300 GeV/c hadron beam	300 GeV/c electron beam	200 GeV/c electron beam	150 GeV/c electrons max ΣB^2	100 GeV/c electrons max ΣB^2
X slit	313.94	-	4.1 mm	4.1 mm	4.8 mm	6.1 mm
QP 11	313.94	5.297	5.190	3.510	2.631	1.758
QP 12	338.33	- 5.297	- 5.190	- 3.510	- 2.631	- 1.758
BM 13	359.30	12.589	12.267	0	13.872	12.509
BM 14	362.65	"	"	12.467	- 9.033	-13.911
BM 15	366.00	"	"	"	13.872	13.911
BM 16	369.36	"	"	"	13.872	13.911
BM 17	372.71	"	"	"	- 9.033	-13.911
BM 18	376.06	"	"	0	13.872	12.509
QP 13	387.10	5.297	5.134	3.485	2.617	1.751
SX 3	390.45	1.580	1.531	1.039	9.781	0.522
QP 14 (Cerenkov Counter)	411.48	- 5.297	- 5.134	- 3.485	- 2.617	- 1.751
F 3 (p hodoscope)	460.25	-	-	-	-	-
QP 15	460.25	5.297	5.134	3.485	2.617	1.751
BM 19	463.60	10.874	10.524	7.150	5.372	3.594
BM 20	466.95	"	"	"	"	"
QP 16 (Cerenkov Counter)	484.63	- 5.297	- 5.120	- 3.482	- 2.617	1.751
ϕ Hodoscope	528.48	-	-	-	-	-
BM 21 bend = .156°	528.98	8.925	8.622	5.865	4.408	2.950
SX 4	532.33	1.580	1.526	.1038	0.780	0.522
QP 17	533.40	6.829	6.594	4.488	3.366	2.257
BM 22	536.75	14.000	13.457	9.187	0	- 4.623
BM 23	540.11	"	"	"	13.813	13.869
BM 24	543.46	"	"	"	"	"
BM 25	546.81	"	"	"	0	- 4.623
θ Hodoscope	550.62	-	-	-	-	-
QP 18	551.38	- 7.000	-6.698	- 4.587	- 3.450	- 2.310
QP 19	554.74	- 2.899	-2.774	- 1.900	- 1.429	- 0.956
BM 26 bend = .244°	558.09	14.000	13.382	9.172	6.898	4.619
QP 20	568.36	7.000	6.683	4.584	3.449	2.310
F 4 (Electron expt)	577.51	-	-	-	-	-
Final central momentum (GeV/c) -		300.0	286.4	196.5	147.8	99.0

TABLE III

 π/e RATIOS AND EFFECTS OF SYNCHROTRON RADIATION

Energy GeV	Beam mode	π/e Ratio ^(a) after slit at F2	Fractions of pions ^(b) in e spot at F2 which remain in e spot at F4	π/e Ratio at F4	π/e Ratio with D ₂ filter ²
300	all magnets	not available	0	0	0
200	min magnets	2.7×10^{-4} (c)	.017	4.6×10^{-6}	2.3×10^{-6}
150	all magnets max ΣB^2	2.2×10^{-4} (d)	.16	3.4×10^{-5}	1.7×10^{-5}
100	all magnets max ΣB^2	1.7×10^{-4} (c)	.56	1.0×10^{-4}	5×10^{-5}

(a) Pion decay before F4 is allowed for.

(b) With synchrotron radiation compensated settings.

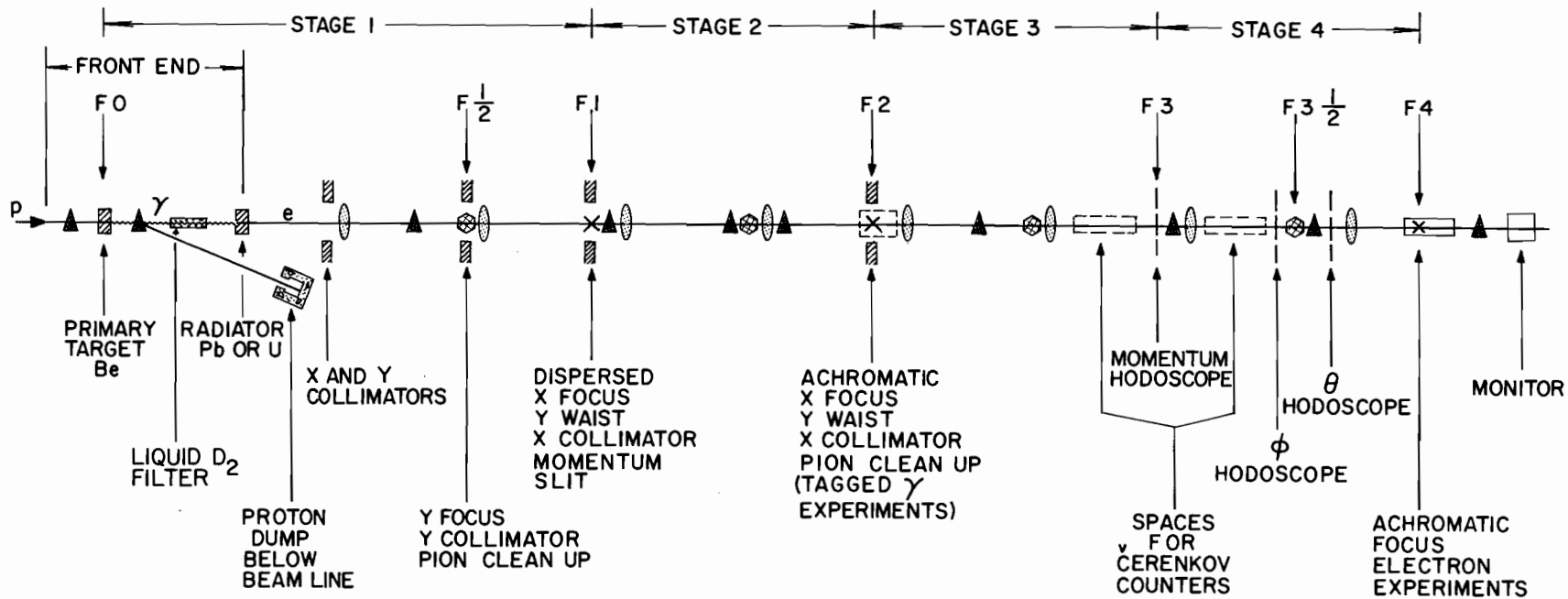
(c) Hagedorn-Ranft model.

(d) Interpolated.

FIGURE CAPTIONS

- Fig. 1 Schematic Layout of Electron Beam.
- Fig. 2 Electron yields calculated from a multiperipheral model⁷⁾ for the present beam line ($\Delta p/p$) $\Delta\Omega = 9.5 \mu\text{ster } \% \Delta p/p$, Beryllium target 40.3 cm, 0.5 rad. length lead radiator. Number of electrons/ 10^{13} incident protons at various production angles θ and momenta: (a) 200 GeV/c, (b) 300 GeV/c, (c) 400 GeV/c, (d) 500 GeV/c, (e) 1000 GeV/c - See Text.
- Fig. 3 Electron beam layout and optics.
(a) Arrangement of magnetic elements. Each symbol may represent several physical components as indicated. Positions of bending magnets and sextupoles are displaced where necessary for clarity. For exact locations see table II.
(b) First order matrix elements in horizontal (x) plane ($\delta = \Delta p/p$).
(c) First order matrix elements in vertical (y) plane.
(d) Second order beam envelopes as calculated by TRANSPORT¹²⁾ for $\Delta p/p = 0$ and $\pm 2\%$ and primary aperture slits $x = \pm 15$ mm and $y = \pm 30$ mm.
- Fig. 4 Vertical (y) beam profile ($\Delta p/p = \pm 3\%$) at first y focus ($F \frac{1}{2}$), showing size of slit for primary pion clean up. Histograms in figures 4-10 are calculated using the Monte Carlo ray tracing program TURTLE¹³⁾, based on effective primary spot size expected at 100 GeV/c. Effects of imperfections in the quadrupole fields, as actually measured¹⁵⁾ are taken into account. First order magnitudes as calculated by TRANSPORT¹²⁾ indicated where appropriate. Ordinate scales are linear and arbitrary.
- Fig. 5. Momentum resolution and acceptance at F1.
(a) Resolution with sextupole adjusted to correct aberrations at F2. The slight asymmetry is due to the term $\langle x | x_o' | x_o' \rangle$
(b) Resolution without sextupoles.
(c) Acceptance with sextupoles. Note the sharp cut off and the asymmetry.
(d) Acceptance without sextupoles.
- Fig. 6 Beam profiles at F2.
(a) Horizontal profile with optimised sextupole settings. Note that the beam spot is almost entirely within the first order limits.
(b) Vertical profile. This occurs at a waist (not a focus) in the beam envelope and is unaffected by the sextupoles.
(c) Horizontal profile without sextupoles. The wings of this distribution would cause serious losses in subsequent stages.

- Fig. 7 Momentum Resolution at F3 for primary beam spot ± 2.5 mm and no slit at F2. Resolution is shown for the nominal momentum p_0 and for $1.016 p_0$. The centroid displacements are due to the aberrations $\langle x | x_0' x_0' \rangle$ and $\langle x | \delta \delta \rangle$.
- Fig. 8 Resolutions at angle hodoscopes.
 (a) Horizontal (x) distributions for rays which pass through the experimental target at $\theta = 0$ and 0.5 mr. The finite distribution widths are mainly due to the small dispersion at the hodoscope, calculated for $\Delta p/p = \pm 2\%$.
 (b) Vertical (y) distributions for rays which pass through the experimental target at $\phi = 0$ and 0.5 mr. The hodoscope cannot be located exactly at the primary vertical focus of the last quadrupole set, so that the finite widths are due to the vertical beam spot size.
- Fig. 9 Electron beam profiles at experimental target focus F4 at 100 GeV/c.
 (a) Horizontal (x)
 (b) Vertical (y).
- Fig. 10 Electron and pion horizontal beam profiles at F4 showing the effect of synchrotron radiation in a radiation compensated beam.
 (a) 100 GeV/c, (b) 150 GeV/c. At these two momenta all the magnets in the beam line are used, some with reversed polarity, to maximize ΣB^2 and enhance the e, π separation.
 (c) 200 GeV/c, (d) 300 GeV/c. At these higher momenta, only the necessary number of bending magnets consistent with $B \leq 14$ kgauss are used. See table II.



LEGEND

- X = HORIZONTAL (BENDING PLANE) DISPLACEMENT
- Y = VERTICAL DISPLACEMENT
- ▲ SET OF BENDING MAGNETS
- ◉ SET OF QUADRUPOLES
- ⊗ SEXTUPOLE

FIG.1 SCHEMATIC LAYOUT OF ELECTRON BEAM

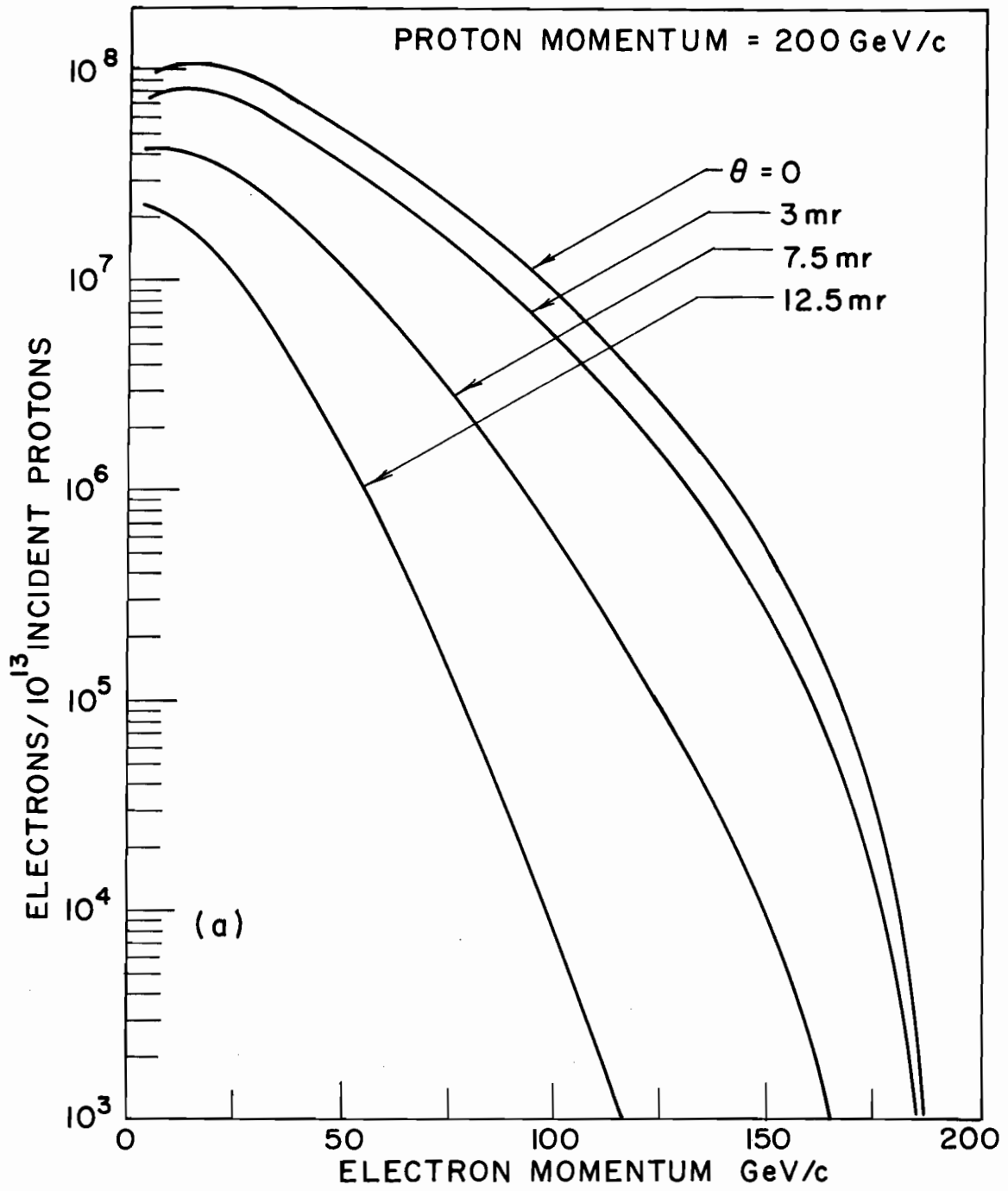


FIG. 2(a)

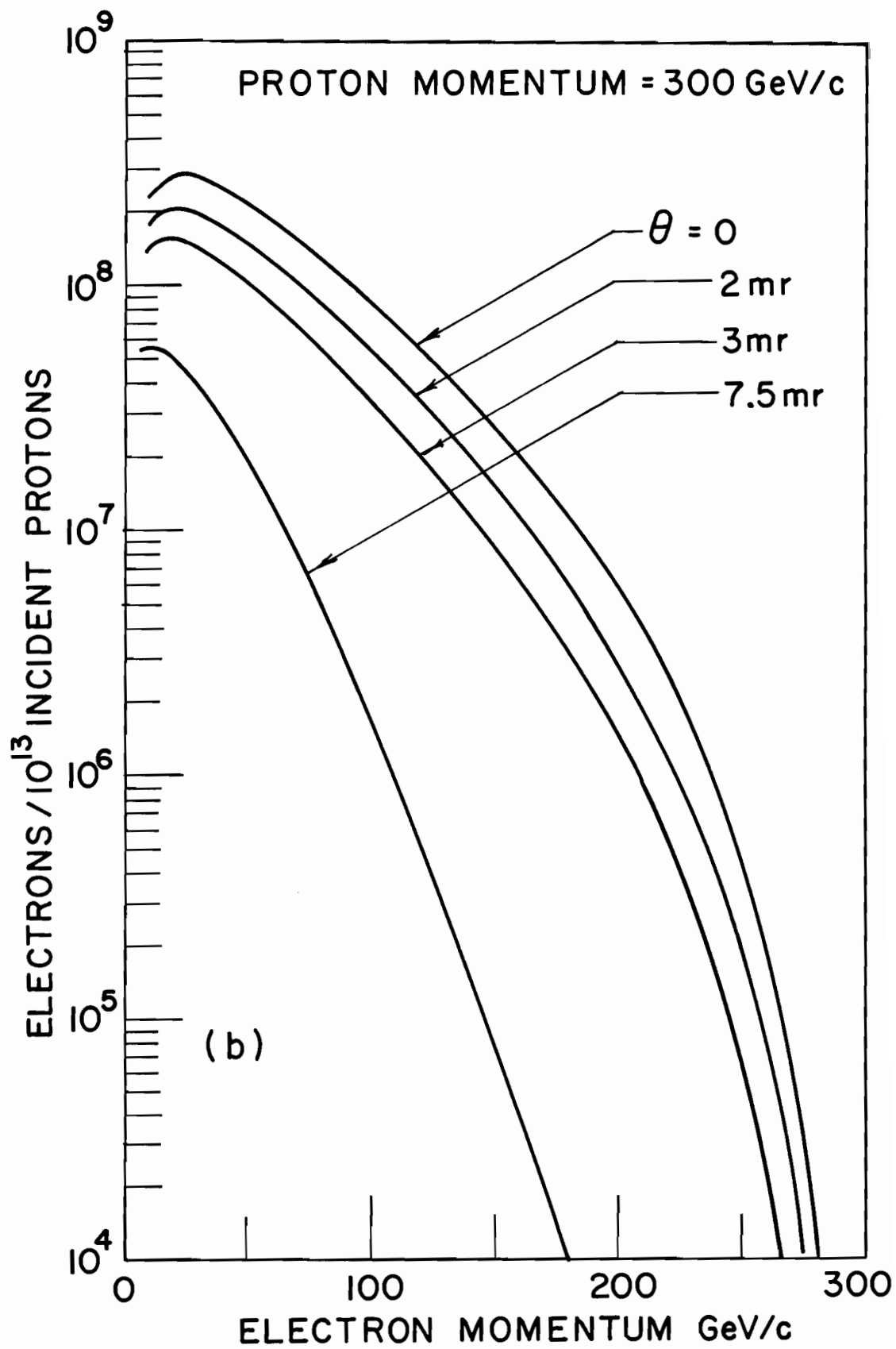


FIG. 2(b)

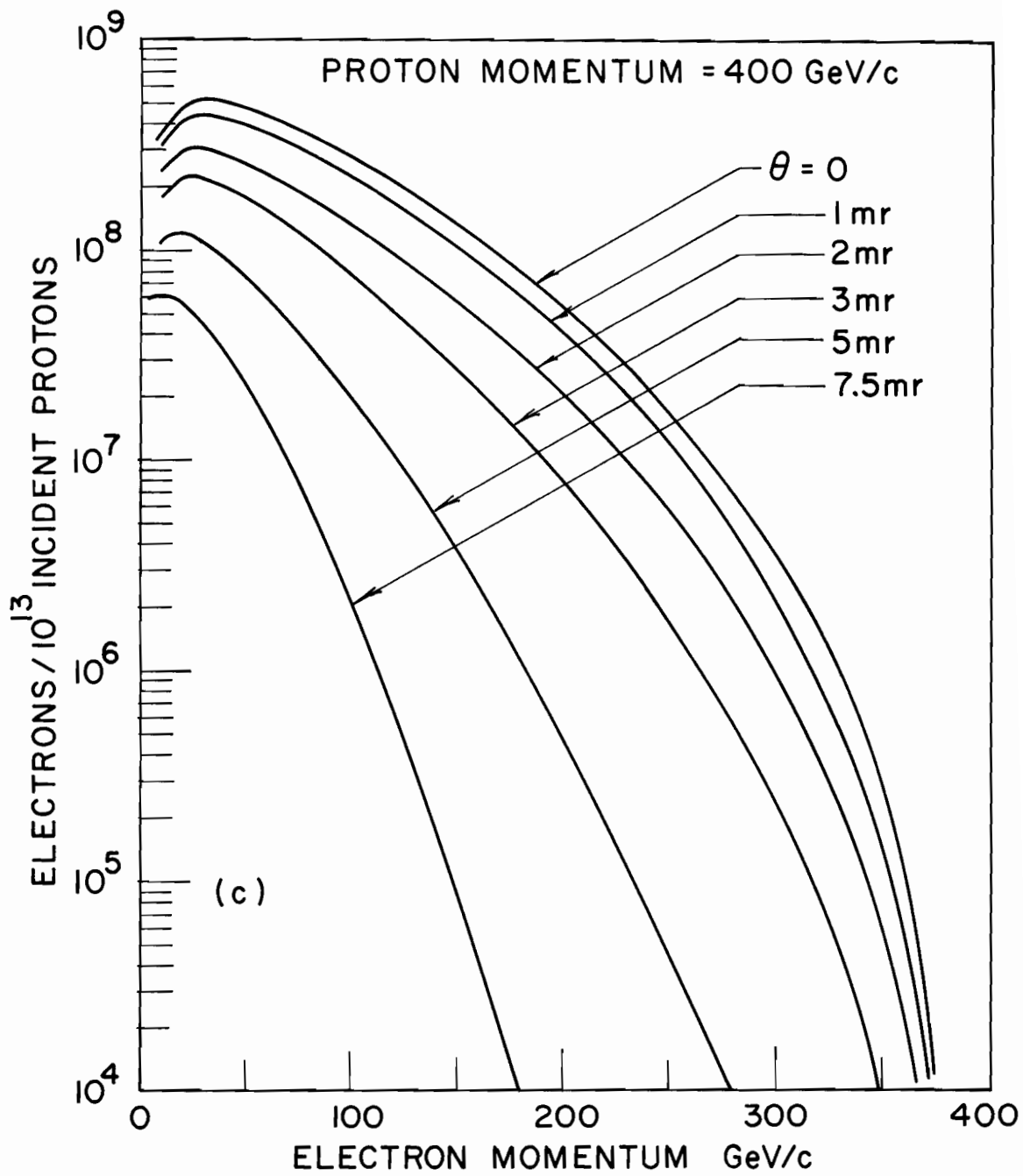


FIG. 2(c)

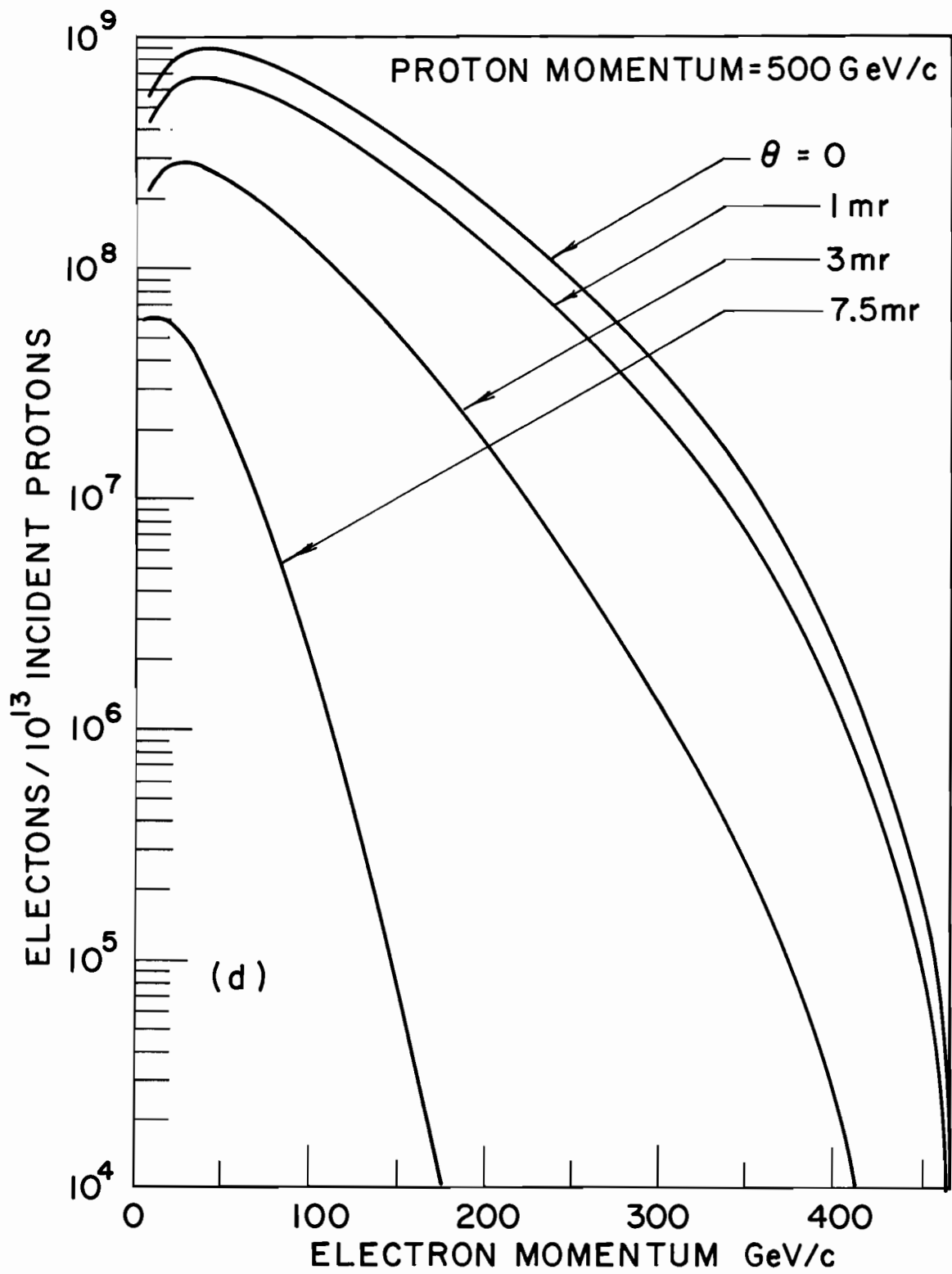


FIG. 2(d)

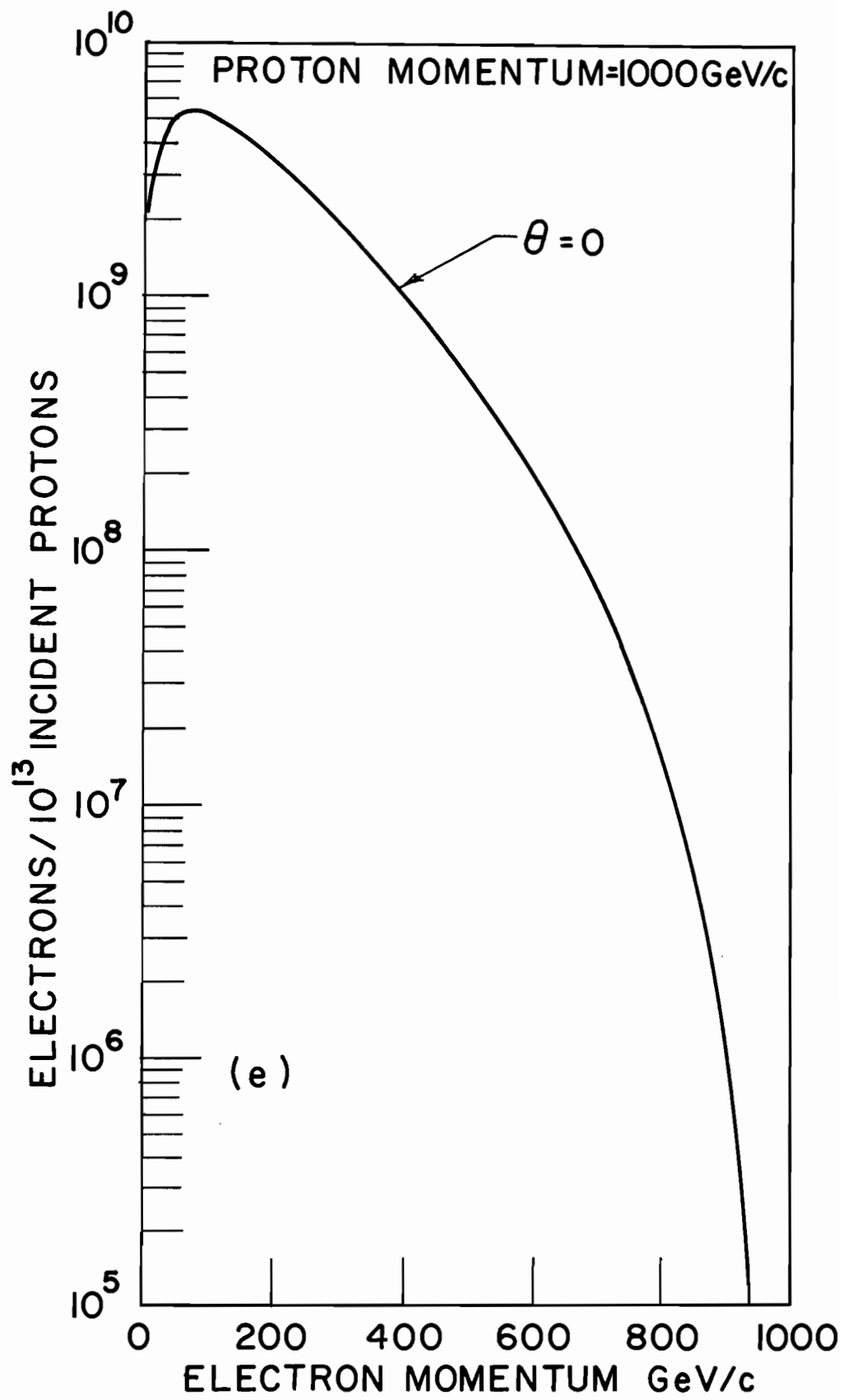


FIG. 2(e)

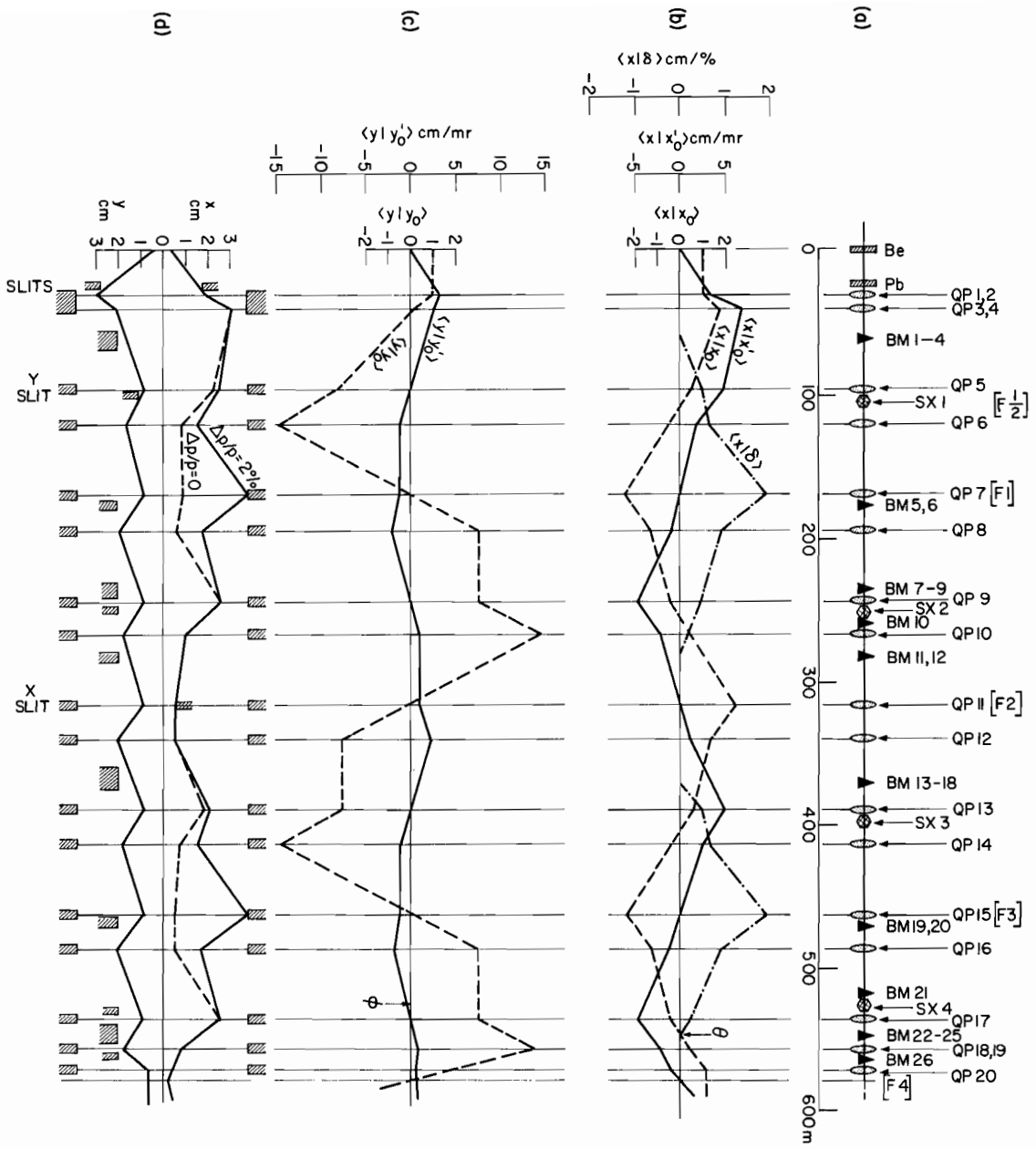


FIG. 3 ELECTRON BEAM LAYOUT AND OPTICS

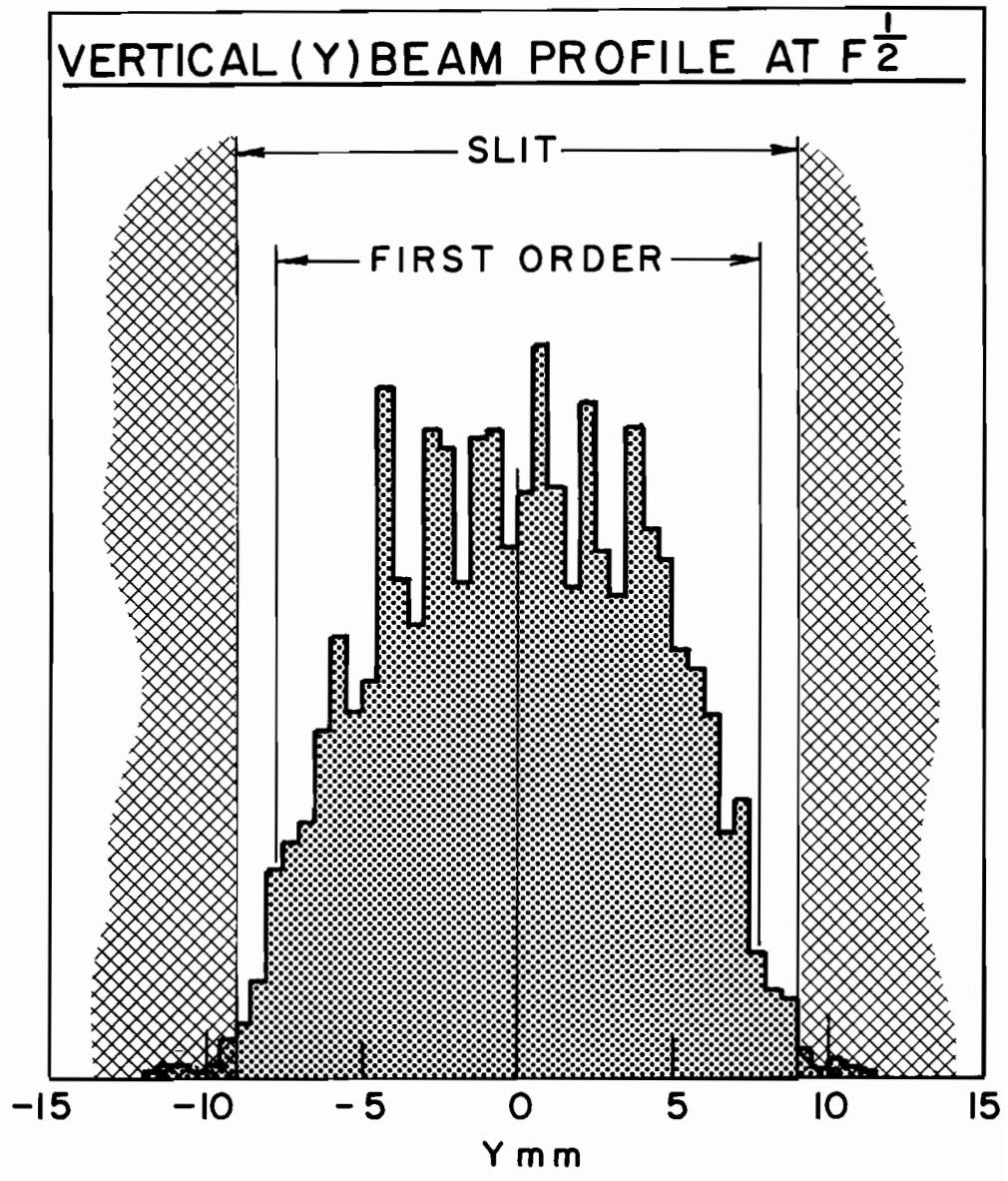


FIG. 4

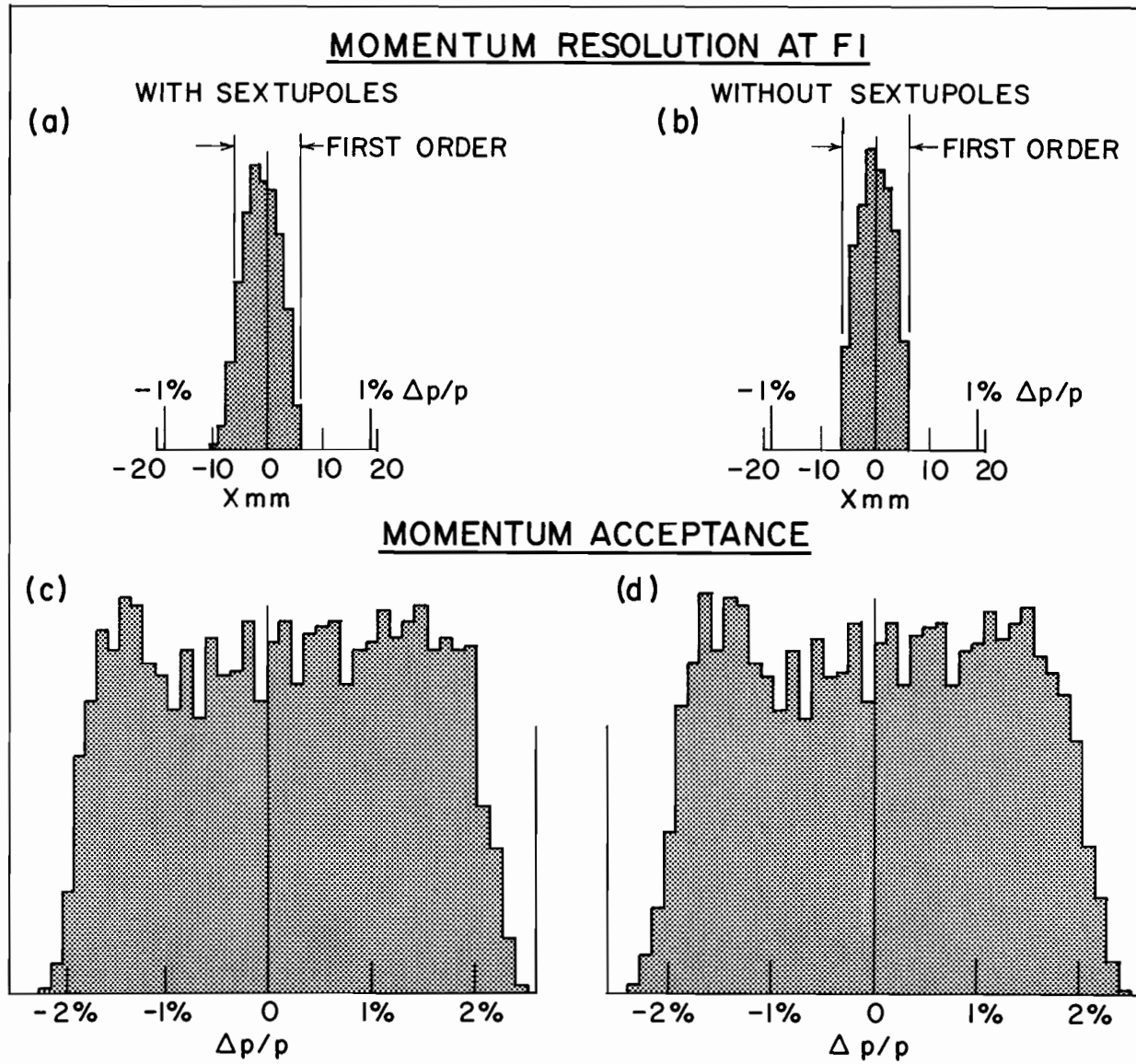


FIG. 5

BEAM PROFILES AT F2

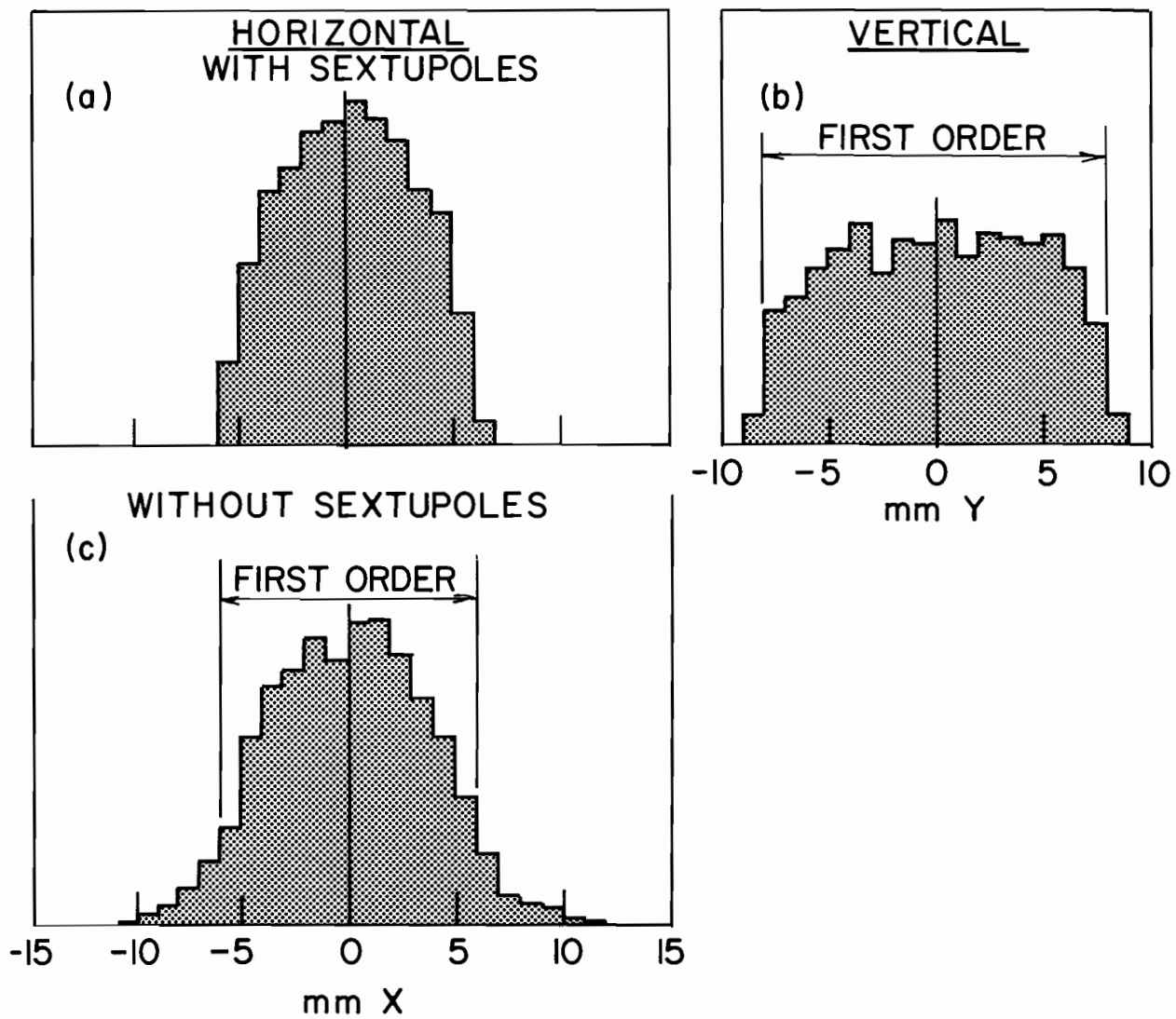


FIG. 6

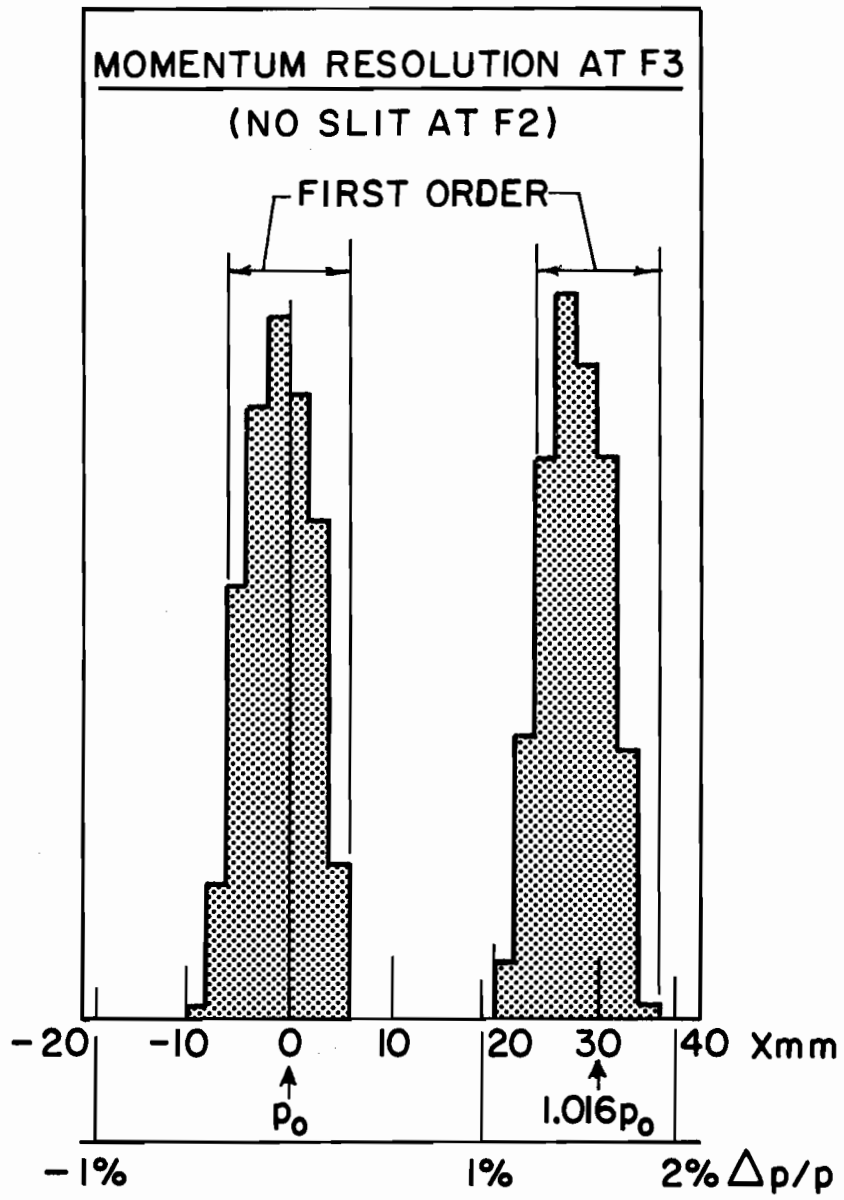


FIG. 7

RESOLUTION AT ANGLE HODOSCOPIES

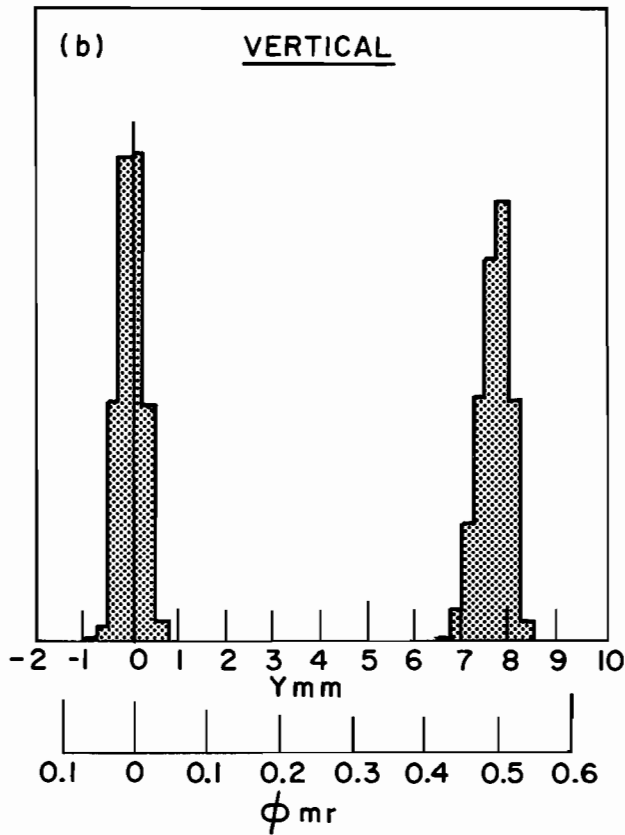
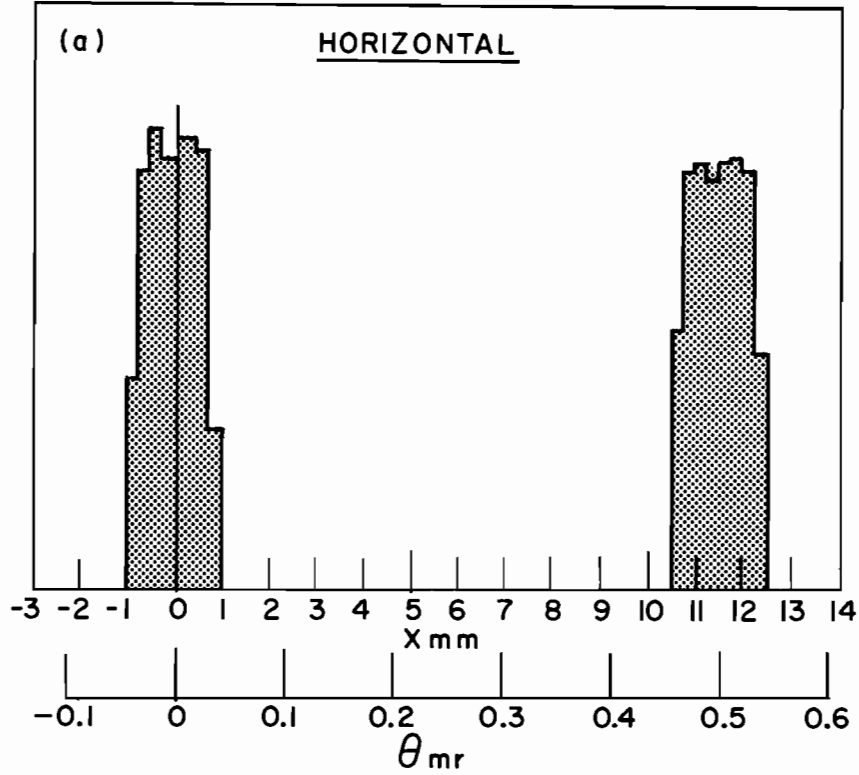


FIG. 8

BEAM PROFILES AT F4 AT 100 GeV/C

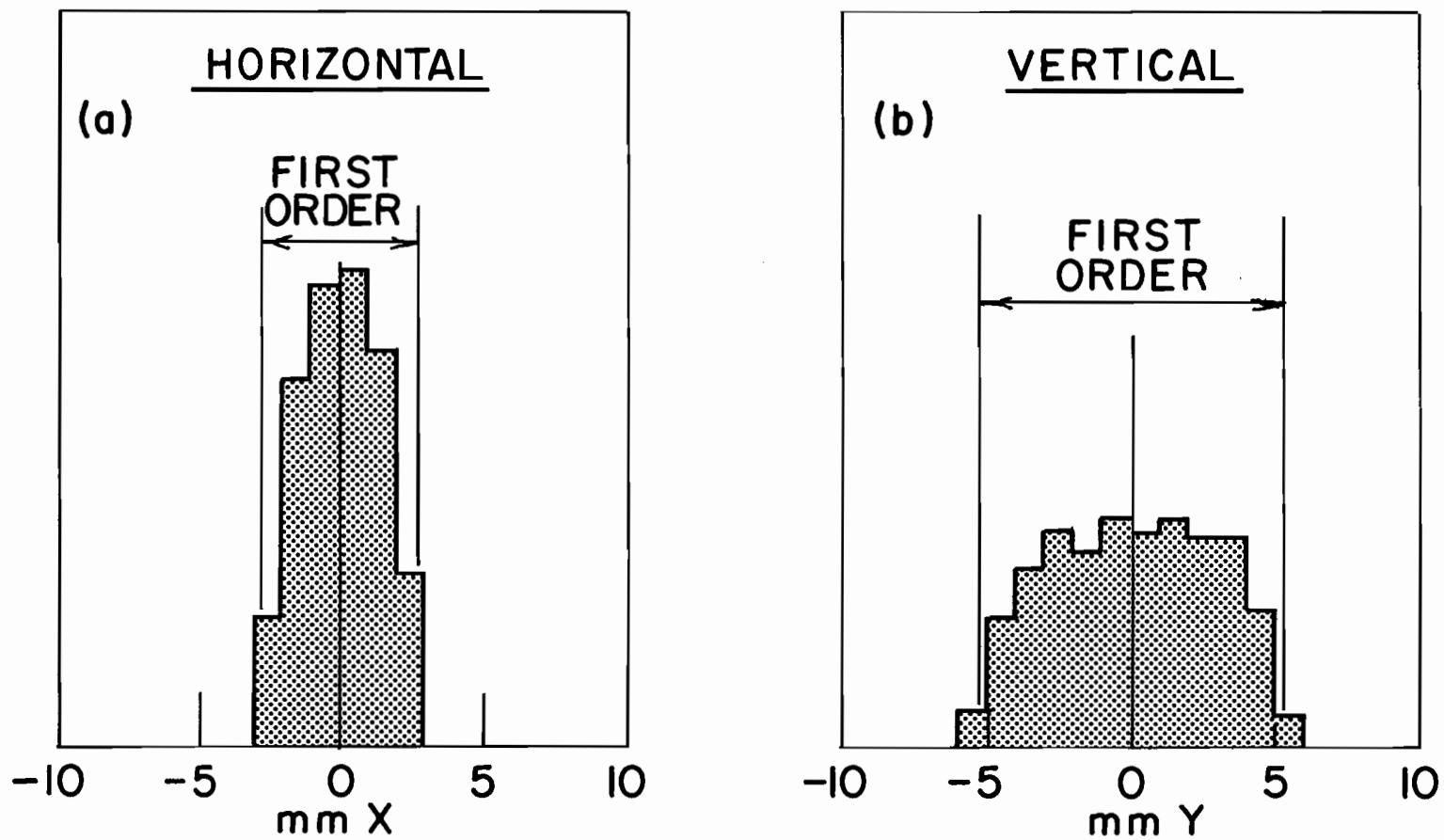


FIG. 9

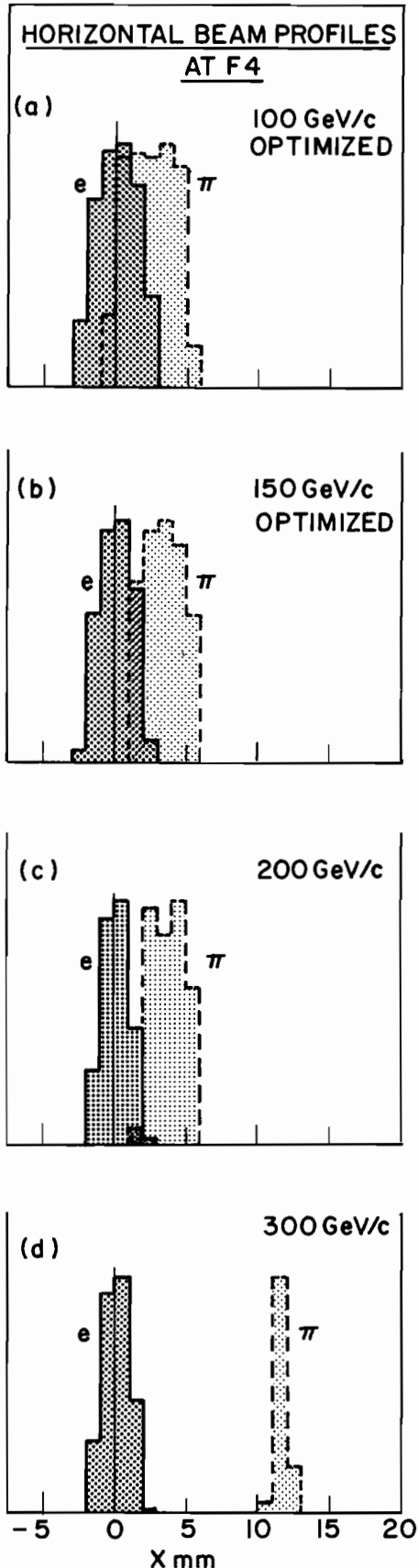


FIG. 10

REFERENCES

- 1) J. F. Crawford, Z. G. T. Guiragossian, R. Hofstadter, E. B. Hughes
R. E. Rand, R. F. Schilling, M. R. Yearian, E. V. Hungerford III,
G. S. Mutchler, G. C. Phillips and B. W. Mayes, NAL Proposal No. 164.
- 2) J. J. Murray, (SLAC) private communication.
A. L. Read, (NAL) private communication.
D. D. Reeder (University of Wisconsin) private communication
- 3) General references on e beams at NAL
A. L. Read, Design Study, 200 BeV Accelerator, Vol. 1, UCRL-16830, 1966.
C. A. Heusch, Design Study, 200 BeV Accelerator Vol. 3, UCRL-16830, 1966.
W. T. Toner, 1968 NAL Summer Study, Vol. 2.
C. A. Heusch, Ibid.
R. Diebold and L. Hand, 1969 NAL Summer Study, Vol. 1.
C. A. Heusch, Ibid.
Z. G. T. Guiragossian and F. Villa, Ibid., Vol. 3 .
R. Morrison, K. Pretzl and A. L. Read, 1970 NAL Summer Study.
A. Mischke et al, Ibid.
R. Morrison et al, Proc. Int. Conf. on Instrumentation for H.E.P.,
Dubna, 1970.
A. L. Alikanian et al, IHEP 70-105, 1970. (Electron beam at Serpukhov)
- 4) This number is based on yield estimates calculated using a multiperipheral
model (Ref. 7) and the Hagedorn-Ranft model, Suppl. Nuovo Cim. I, 6, 169,
1968.
- 5) C. Halliwell, P. J. Biggs, W. Busza, M. Chen, J. Nash, F. Murphy,
G. Luxton and J. D. Prentice, Nuc. Inst. and Meth. 102, 51, 1972 .

- 6) G. R. Charlton and G. H. Thomas, Phys. Letts., 40B, 378, 1972.
- 7) L. Caneschi and A. Pignotti, Phys. Rev. Letts., 22, 1219, 1969.
- 8) Particle Data Group, UCRL-20000 NN, August 1970.
- 9) D. Dekker et al, Phys. Rev. 137, B962, 1965.
- 10) W. Heitler, The Quantum Theory of Radiation, 3rd Ed., Oxford, 1954, p. 259 et seq.
- 11) K. L. Brown, SLAC-75.
- 12) TRANSPORT, K.L. Brown and S. K. Howry, SLAC-91.
- 13) TURTLE, D. Carey, NAL-64, 1971. F. Rothacker (SLAC) is to be thanked for assistance in running both programs, TRANSPORT and TURTLE.
- 14) T. Nash (NAL) private communication.
- 15) J. Cobb (SLAC) is to be thanked for providing this information and for elucidating the technique of the multipole expansion.
- 16) F. Murphy (UCSB) private communication.
- 17) B. Margolis, P. M. Patel, W. Ross, D. G. Stairs, L. Bird, C. Halliwell, R. Morrison, J. Walters, E. Coleman, T. Fesesse, Y. Makdisi, U. J. Becker, P. Biggs, W. Busza, M. Chen, T. Nash, H. F. W. Sadrozinski, S. C. C. Ting, S. L. Wu, T. T. Wu, NAL Proposal No. 144.
- 18) F. J. M. Farley, E. Picasso and L. Bracci, CERN NP Int. Rep. 71-11, 1971 and Nucl. Inst. and Meth. 103, 325, 1972.
- 19) P. J. Biggs (MIT) and J. Prentice (Univ. of Toronto) private communications.

Professor Robert R. Wilson

23 January 1973

TECHNICAL ATTACHMENT I

Signal Shaping of Large NaI(Tl) TASC Spectrometers for #192 and #193.

Our current NaI(Tl) crystal optics and signal shaping method was used in a Mark III accelerator test with 580 MeV electrons. This is described in the attached Fig. 1(a). In this configuration light is trapped by diffuse reflectors to make the energy response mostly insensitive to particle entrance coordinates. The "raw" (unclipped) signals from the crystal are shown in Fig. 2 together with the energy resolution response at 580 MeV. In Fig. 3 it is seen that the signals are shaped and their zero base-line is restored by our clipping method. The anode pulses from all photomultipliers are mixed directly and the clipping line variable impedance is set to restore a zero base-line on the trailing edge. We find that the signals have 360 nsec full-width at base and the energy resolution is hardly degraded. In Fig. 4 we have achieved a signal of 210 nsec full-width at base with good and only slightly different energy resolution. Any further reduction in pulse width sharply degrades the energy resolution due to the fact that the pulse heights are reduced and fewer photoelectrons are sampled. This effect is demonstrated in Fig. 5. I should remark that this sensitivity to photoelectron statistics in #192 and also in #193 becomes less important at NAL since our signals will be 100-400 times larger. In all of the above cases, energy is measured by our signal peak detection electronics which have also post-pile-up rejection. Thus, only signal pulse heights are used to derive these energy resolution curves. In

all cases we have confirmed that pulse-height and energy are linearly correlated.

1) We can now definitely say that without making any modifications to the present optics of our crystals (diffuse reflection light collection optics), signals can be shaped which have 200 nsec full-width at base without any degradation of energy resolution at NAL energies.

2) The observed 10%-to-90% rise time, t , of these pulses is 80 nsec and good signal shaping requires a pulse width of $2.5 \times t$. Typically, this 80 nsec can be explained by three effects: (a) 10-20 nsec are due to the mixing of signals from 12 photomultipliers, each of which is set to have equal gain but slightly different high voltage value. This effect can be removed by accurate timing compensation prior to mixing signals, which we have not done; (b) 20-30 nsec are due to the actual rise-time property of inexpensive photomultipliers and we can reduce this to about 5 nsec using faster photomultipliers; (c) 50-60 nsec are due to the total transit time of trapped light by the present diffuse reflection optics where typically, several tens of traversals occur in the crystal before light reaches a photocathode surface and each traversal has a transit time of about 5 nsec.

(3) With a smaller NaI(Tl) crystal (4" x 4" x 10"), without the use of Al_2O_3 light diffusing reflectors and with a fast photomultiplier, we have in fact observed a signal rise time of $t = 10$ nsec.

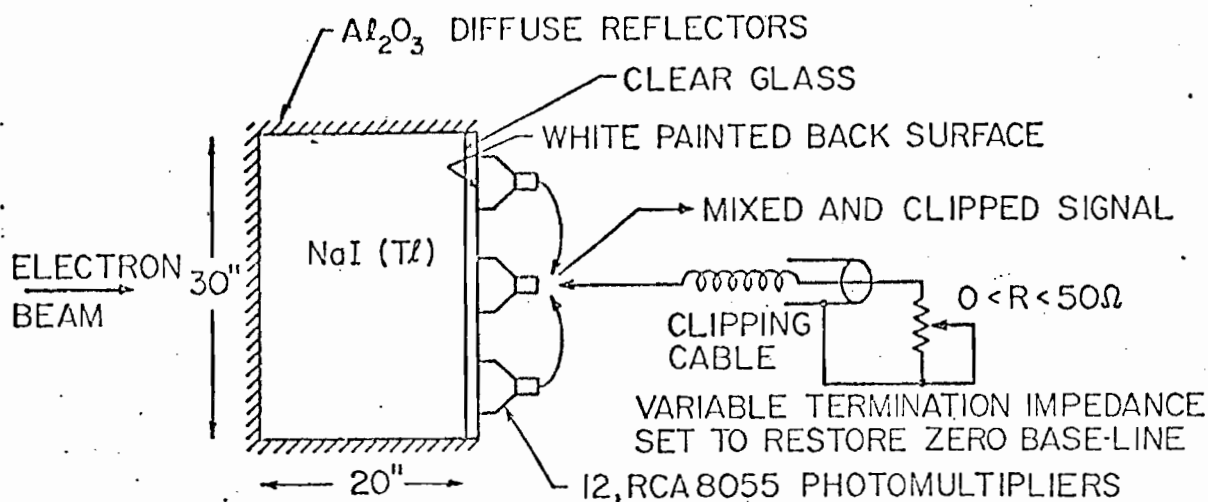
4) Therefore, I believe that we can make further improvements:
(a) By modifying the light collection optics and using faster photomultipliers we should achieve a signal rise time of $t \leq 20$ nsec or

equivalently , a signal shaped to have 50 nsec full-width at base with good energy resolution; (b) I also expect and will test that instead of our present use of 12 slow photomultipliers, a single large and fast photomultiplier would suffice, after a suitable air light-guide separation. We can only afford to do these at NAL energies. In #192/#193 the light intensity will be so large in these crystals that we will be able to collect a smaller fraction of the light and yet have enough photo-electron statistics to provide us with an energy resolution limit of $\pm 0.2\%$. The information from multi-wire proportional chambers, in our proposed spectrometer modules, will take care of a possible smooth variation in TASC signal response, as a function of particle entrance position. This response function will be carefully mapped and stored in our on-line computer system. I plan to test this idea soon by a minor modification of our existing crystal optics, in the manner shown in Fig. 1(b).

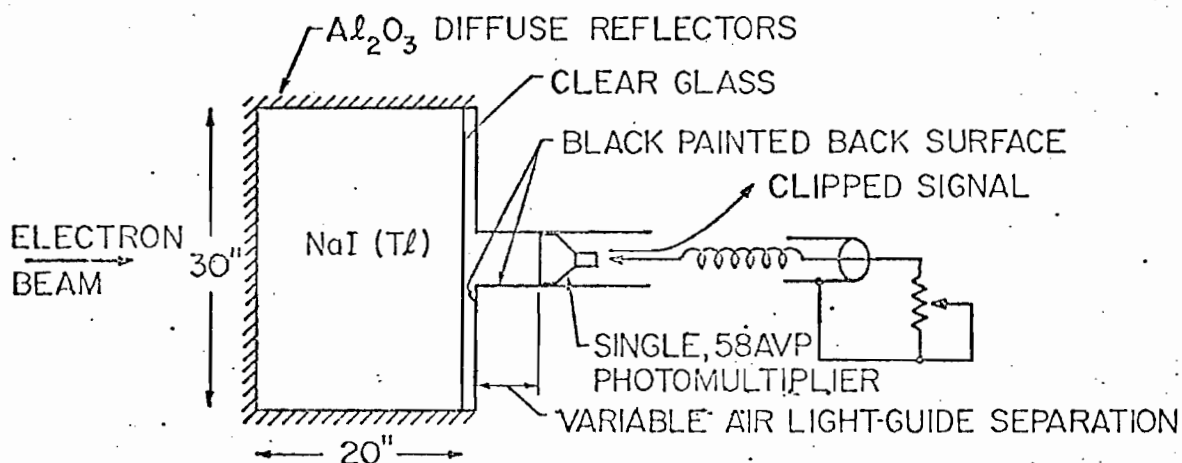
5) Using an extensive Monte Carlo optics program, we are now attempting to design a new crystal assembly. Our aim is to match the available fast NaI(Tl) signal rise time with the best energy resolution and with the best energy response as a function of space coordinates of incident particles. The most likely final configuration is shown in Fig. 1(c).

6) After this study is completed, we would plan to re-encapsulate our crystal to have this new and improved optical configuration and be ready to make the forthcoming test at NAL. At beam energies of 150-300 GeV, I expect to be able to handle 10^9 pions or protons/pulse on a 1 meter long LH₂ target, at production angles of 70 mrad. and beyond.

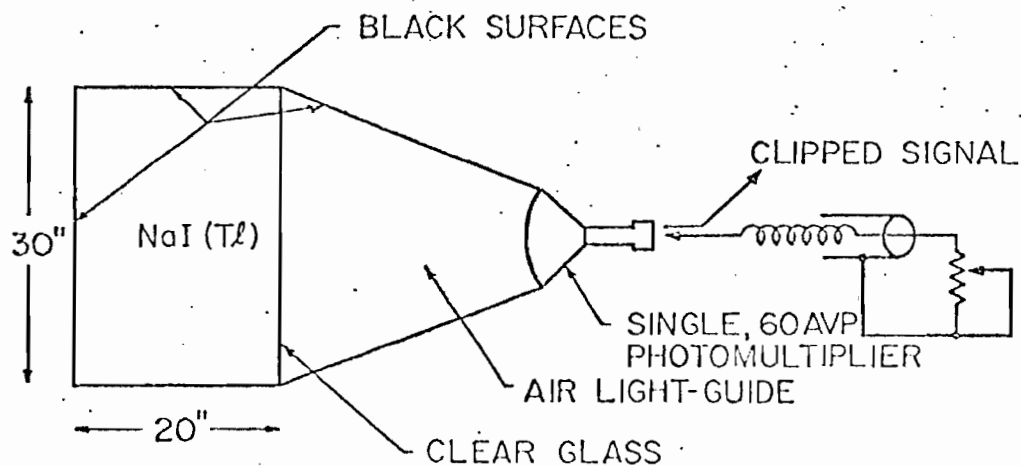
Handwritten signature



(a) NaI (Tl) LIGHT COLLECTION BY DIFFUSE REFLECTION



(b) TEST FOR ENHANCEMENT OF DIRECT COLLECTION OF NaI (Tl) LIGHT



(c) METHOD FOR FAST PULSE SHAPING AND DIRECT-COLLECTION OF NaI (Tl) LIGHT

Figure 1

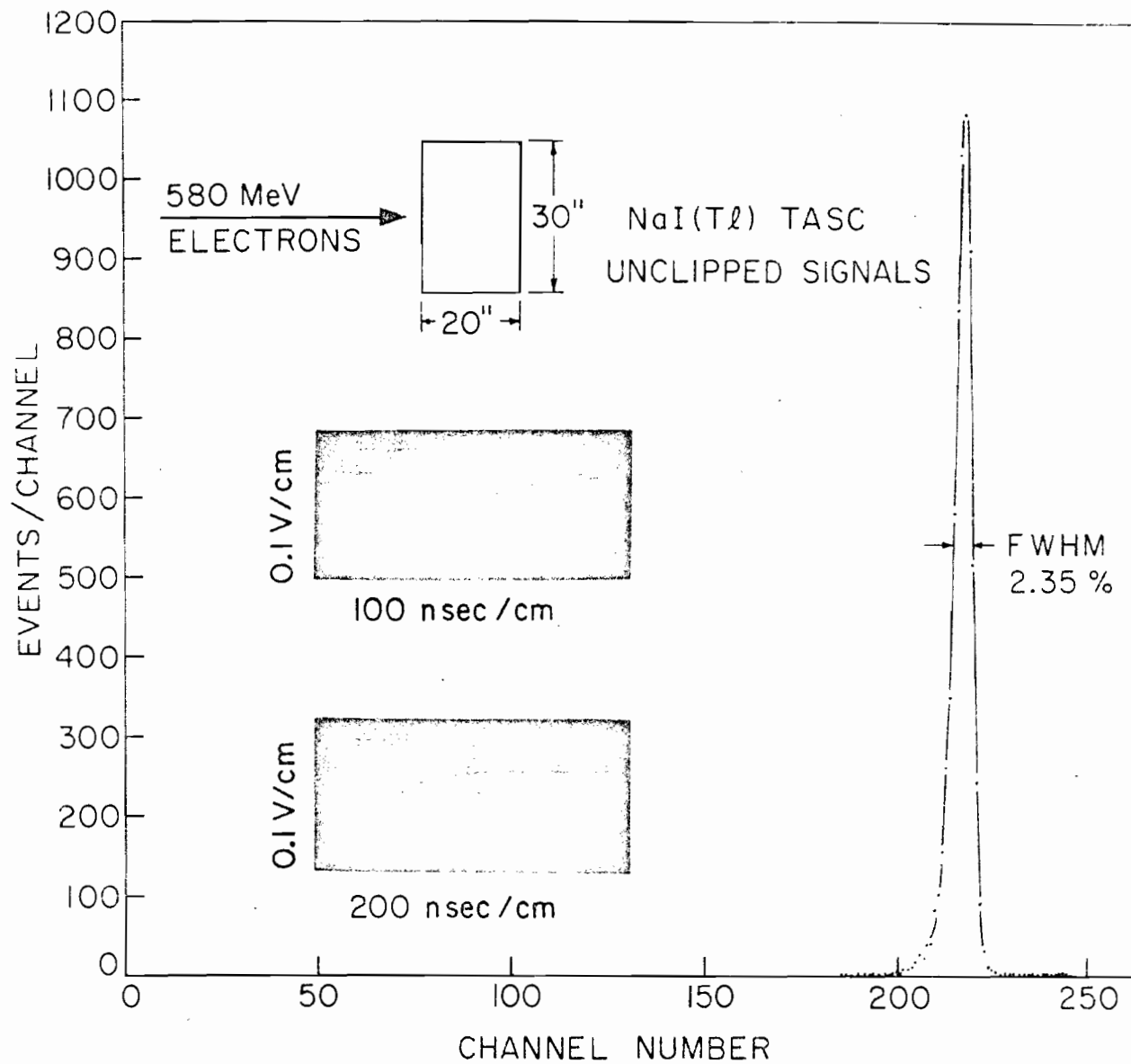


Figure 2

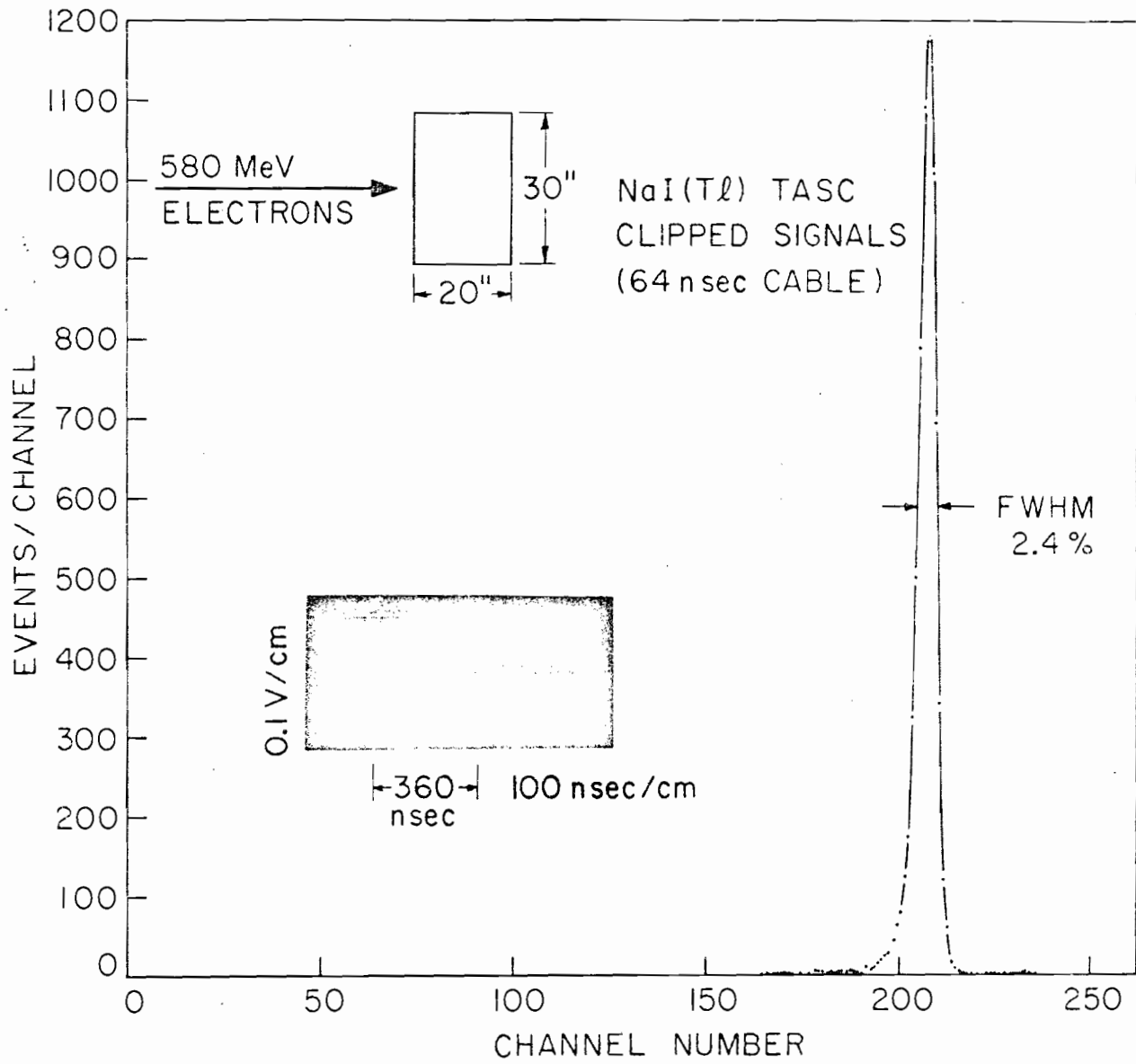
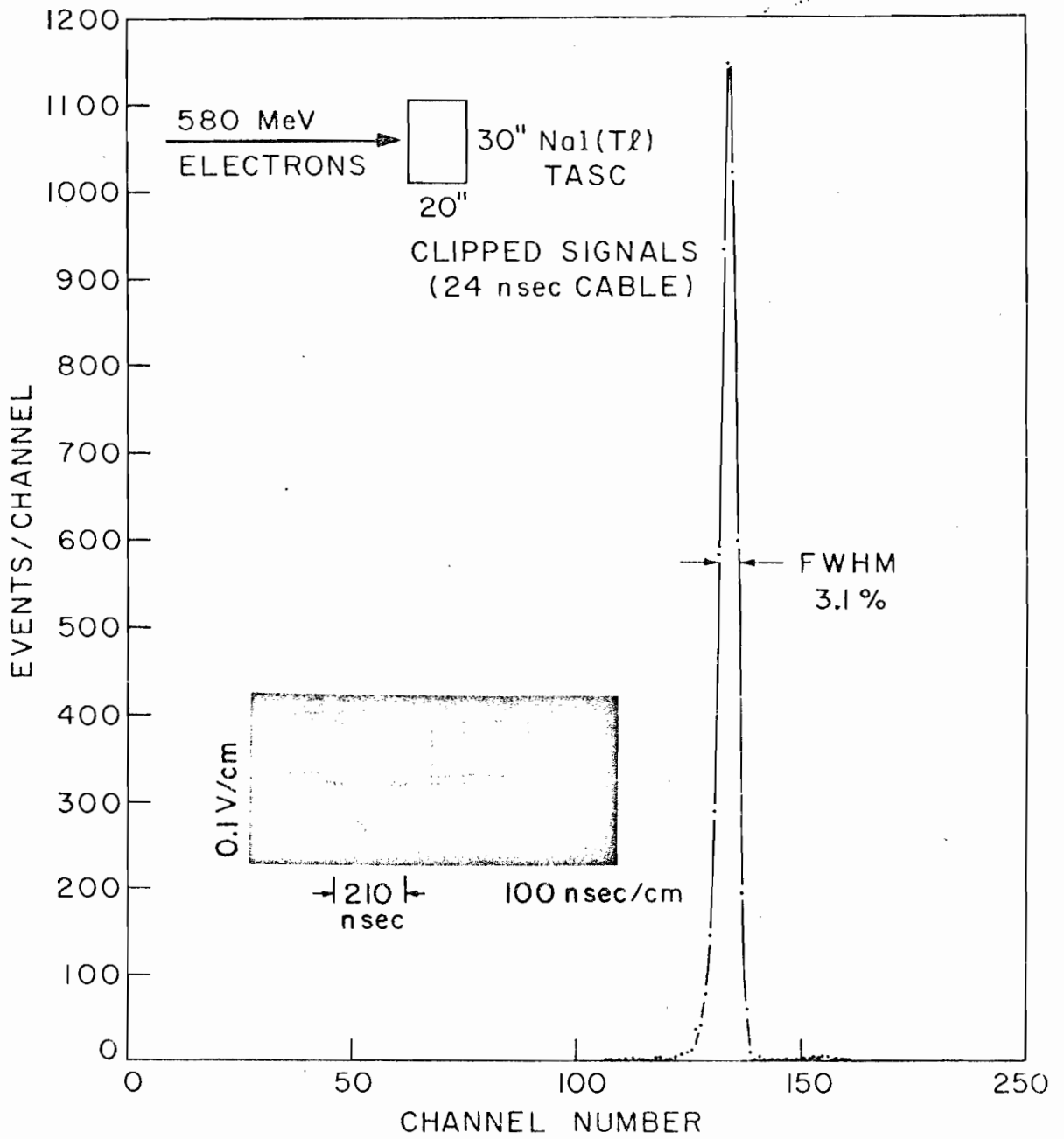


Figure 3



20" THICK, 30" DIAM. NaI(Tl) TASC SIGNAL
SHAPING & ENERGY RESOLUTION RESPONSES
WITH 580 MeV ELECTRONS

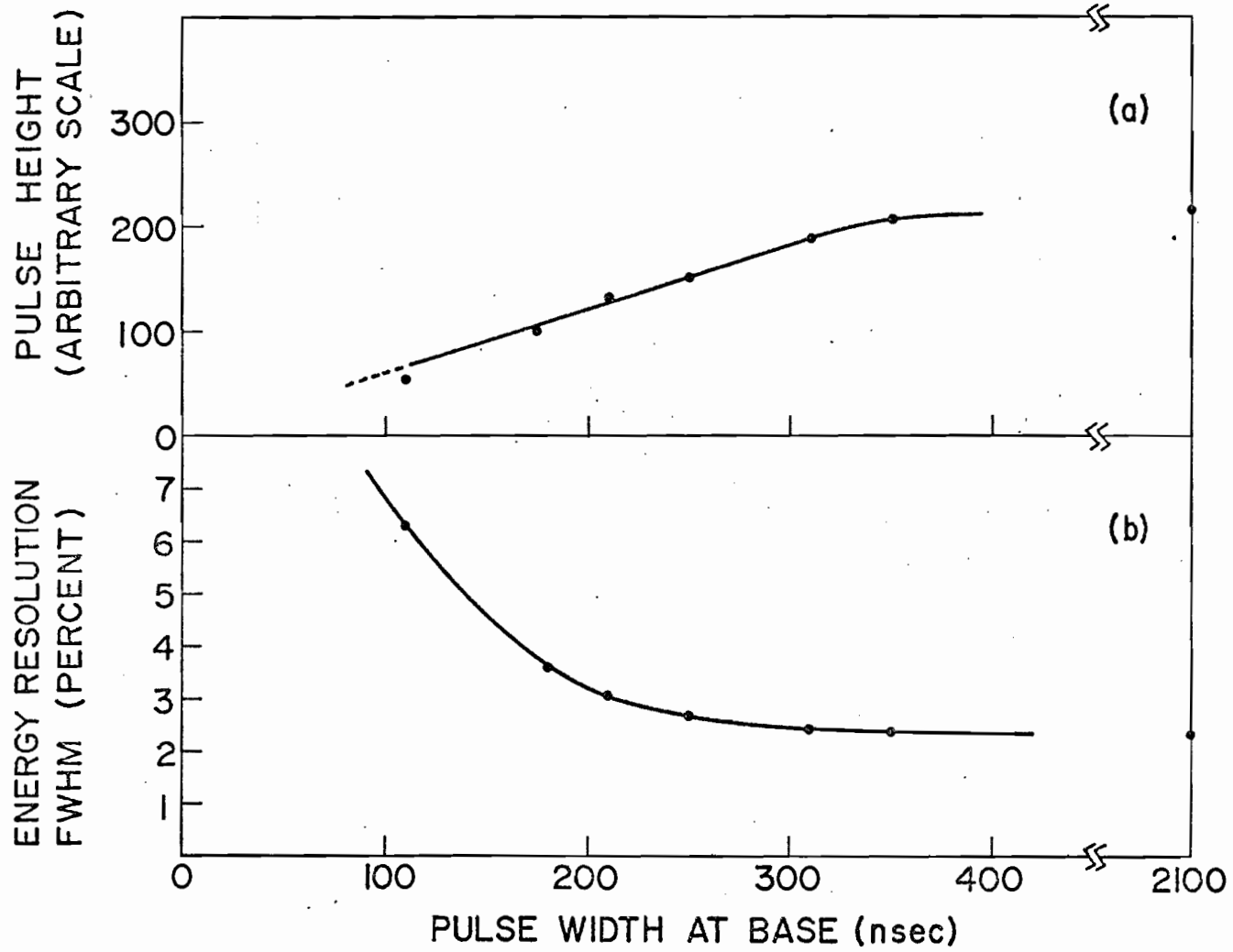


Figure 5

Professor Robert R. Wilson

23 January 1973

TECHNICAL ATTACHMENT II

Background and Pile-up Rates in #192

We know that the beam proposed for this experiment has very good qualities. The four stage beam is far removed from the main ring. It is also sufficiently removed and shielded from the external proton beam and from the secondary beam target. It has a far better transverse displacement than any other beam at NAL. Thus, at the experimental area, beam halo or contamination muon backgrounds are negligible by design and moreover, would be controllable at the front end of the beam. In view of these remarks we should be safe in saying that background in #192 (and also in #193) is entirely target associated at the experimental area. This is somewhat contrary to the personal experiences of many individuals at other accelerator installations or at internal target experimental arrangements.

To estimate the target associated background in #192, I have evaluated the double-differential cross sections for the production of secondaries, coming strictly from hadronic interaction processes. The multi-peripheral model of hadronic interactions is used at 150 GeV and 300 GeV to compute cross sections as a function of production angles and secondary momenta, for p, n, π^+ , π^- and π^0 particles. The use of a 1 meter long LH₂ target is assumed and the target efficiencies are properly accounted for in the production of hadrons, gamma-rays from π^0 decays and in-target conversion of electrons from these gamma-rays. Using the π^0 cross-sections, computer numerical integrations are made to

obtain the double differential distribution of gamma-rays and electrons. Next, momentum integrations are made on all of these spectra to obtain the angular distributions. Finally, angular integrations are made to obtain the rate of events in our detectors.

Earlier, I used this model to estimate the yield of electrons in the NAL High Quality Electron and Pion Beam design work for #193 (and also for #192). I found that my computation agrees to within a factor of about 1.5 with those made by others using different approaches. For the benefit of understanding the background level in #192, we need to know the momentum-angle distribution of all secondaries, starting at the forward direction out to angles of about 300 mrad. Strictly due to hadronic interaction processes, this is the background. Anything in excess of this background becomes redefined as foreground and therefore interesting --the signal in #192, as far as gamma-rays, electrons and muons are concerned. Recent data from the ISR (see Phys. Letters 42B, 279, 1972) show that the large angle production of π^+ , π^- and p from p-p collisions, scales surprisingly well with BNL data. This fact provides additional reliability for my estimations.

In Fig. 6 the momentum-angle distribution of secondary protons or neutrons is shown. The momentum limits attached to the curves provide us with a measure of the maximum momentum value of secondaries, reachable at a given production angle. In each case, at the given momentum limit, 90% of the momentum integration is contained. One-half of the inserted momentum limit corresponds to approximately the

average momentum of secondaries at the given angle. The momentum-angle distribution of secondary π^+ 's and π^- 's is shown in Figs. 7 and 8. Similarly, the distribution of gamma-rays and electrons is given in Figs. 9 and 10.

1) The angular range of interest for the physics in #192 starts at about 50 mrad and extends to about 250 mrad. We conclude from these results that all secondary charged particles (p , π^+ , π^- , e^+ , e^-), produced by hadronic interaction processes, will never reach our detectors. Starting at 40 mrad. and beyond, their momenta are so low that these will be trapped by our analyzing magnet.

2) The high energy secondaries (charged or neutral) are contained within the forward cone of 20 mrad. and extend somewhat out to 40 mrad. At the entrance of our analyzing magnet, I intend to position the target in the gap, at a height such that all high energy charged and neutral secondaries will escape from the magnet, without causing any other harmful secondary collisions. Thus, our detectors will not observe these particles or their debris. Presently, we believe that the use of shielding might be more harmful than beneficial.

3) On a direct line of sight from the target, our detectors will observe (a) background neutrons having average momenta of 3-8 GeV and (b) hadronic generated background gamma-rays having average energy of 1-4 GeV.

4) Background gamma-rays are more abundant than background neutrons by a factor of about 5. From tests we know that in 20" - 30" thick crystals, neutrons will deposit on the average $1/3$ of their energy

whereas gamma-rays or electrons deposit their full energy. Thus signals produced by background neutrals in #192, on the average are equivalent to 1 - 4 GeV full energy absorption.

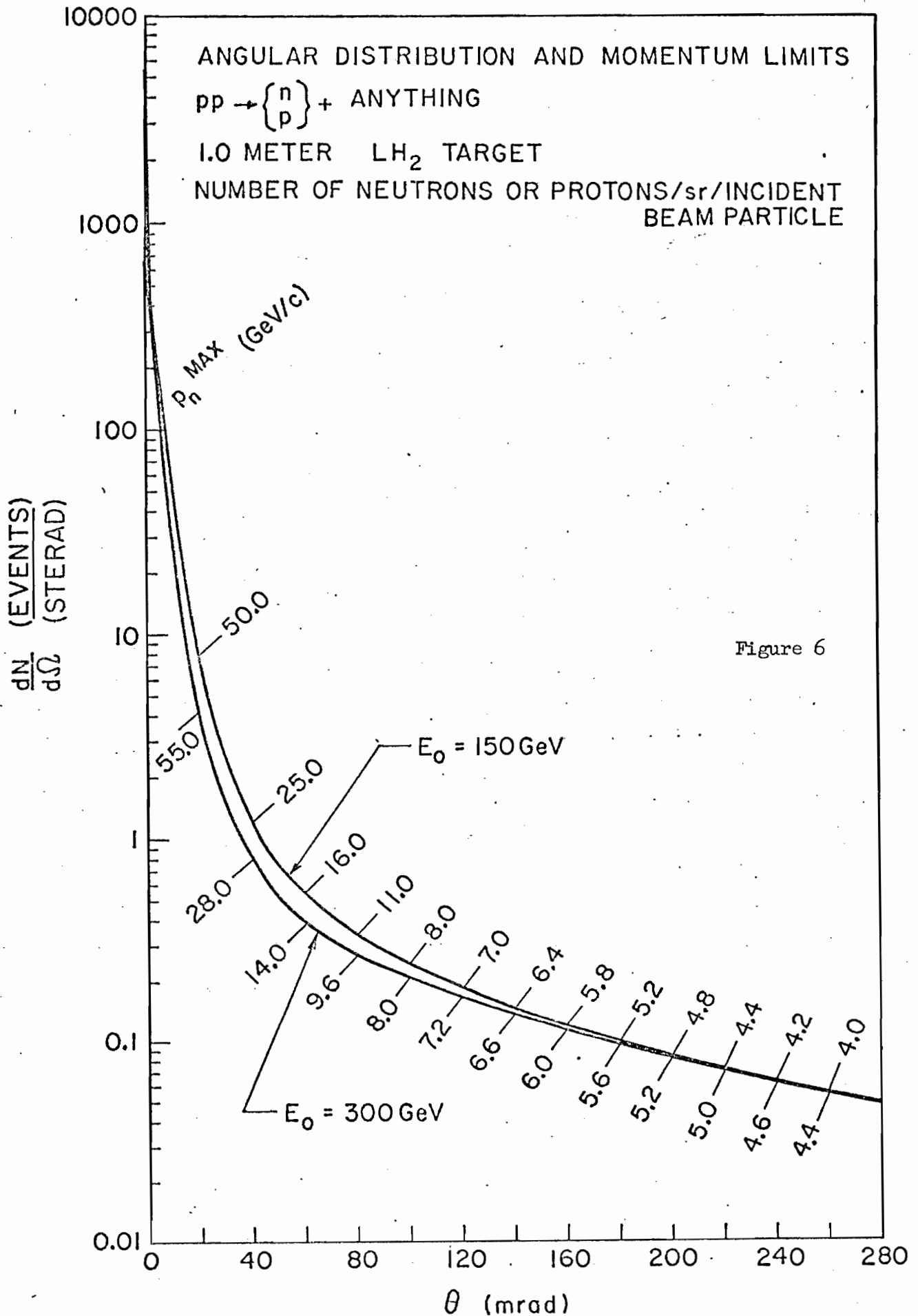
5) The signals expected from the physics in #192 are 10 - 200 times larger than the above background signals in our detectors.

6) Using the parameters $10^8 \pi^-$ /pulse incident on a 1 meter long LH_2 target and our detectors placed to cover the angular range of 40 - 100 mrad., we find that a total of 5×10^5 background low energy neutrons or gamma-rays will be intercepted by our detectors. Also, using a beam of $10^9 \pi^-$ /pulse, which is needed while covering the angular range of 120 - 180 mrad, we find that again the background level is at 5×10^5 /pulse.

7) We have already demonstrated that NaI(Tl) signals are shaped to have 200 nsec full-width at base with good energy resolution. Therefore, at the above rate of 5×10^5 /sec, 10% of large signals from the physics in #192 will have an interference by background small signals.

8) This condition occurs in 10% of our true event triggers and is not characterized as pile-up. In this situation, at most 10% of our valid events will have a zero base-line shift by a small amount. For example, if we have a monochromatic signal providing us with a gaussian line shape distribution, such a zero base-line shift will preserve the peak value of the distribution and broaden the wings at the base of the distribution.

9) Using plastic scintillators which are necessary for other purposes in #192, the fact that such a zero base-line shift has occurred in 10% of valid event signals will be recognized 99.8% of the time. In these cases, event signals will be rejected or tagged so that they are handled separately during the data reduction of our experiment.



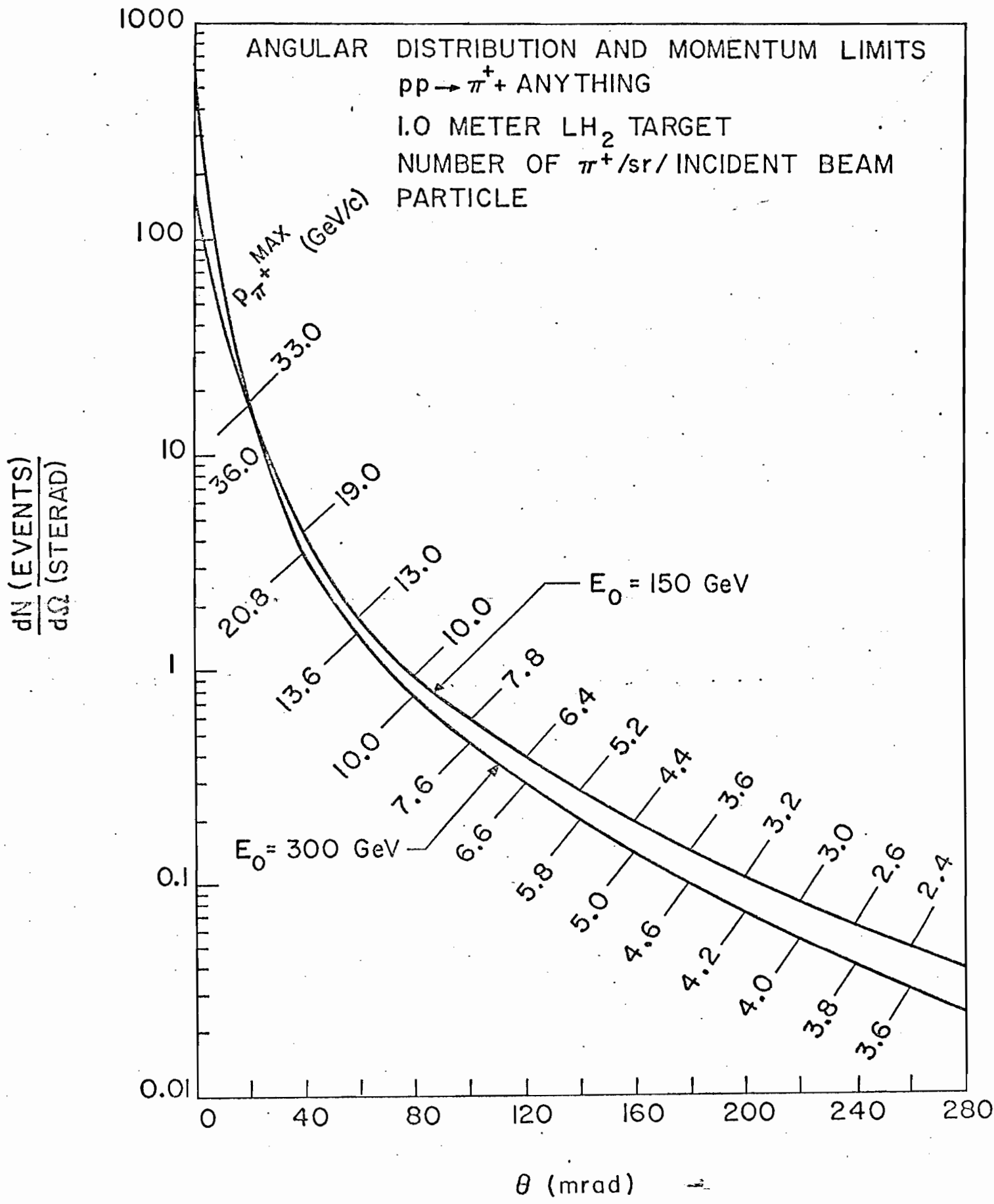


Figure 7

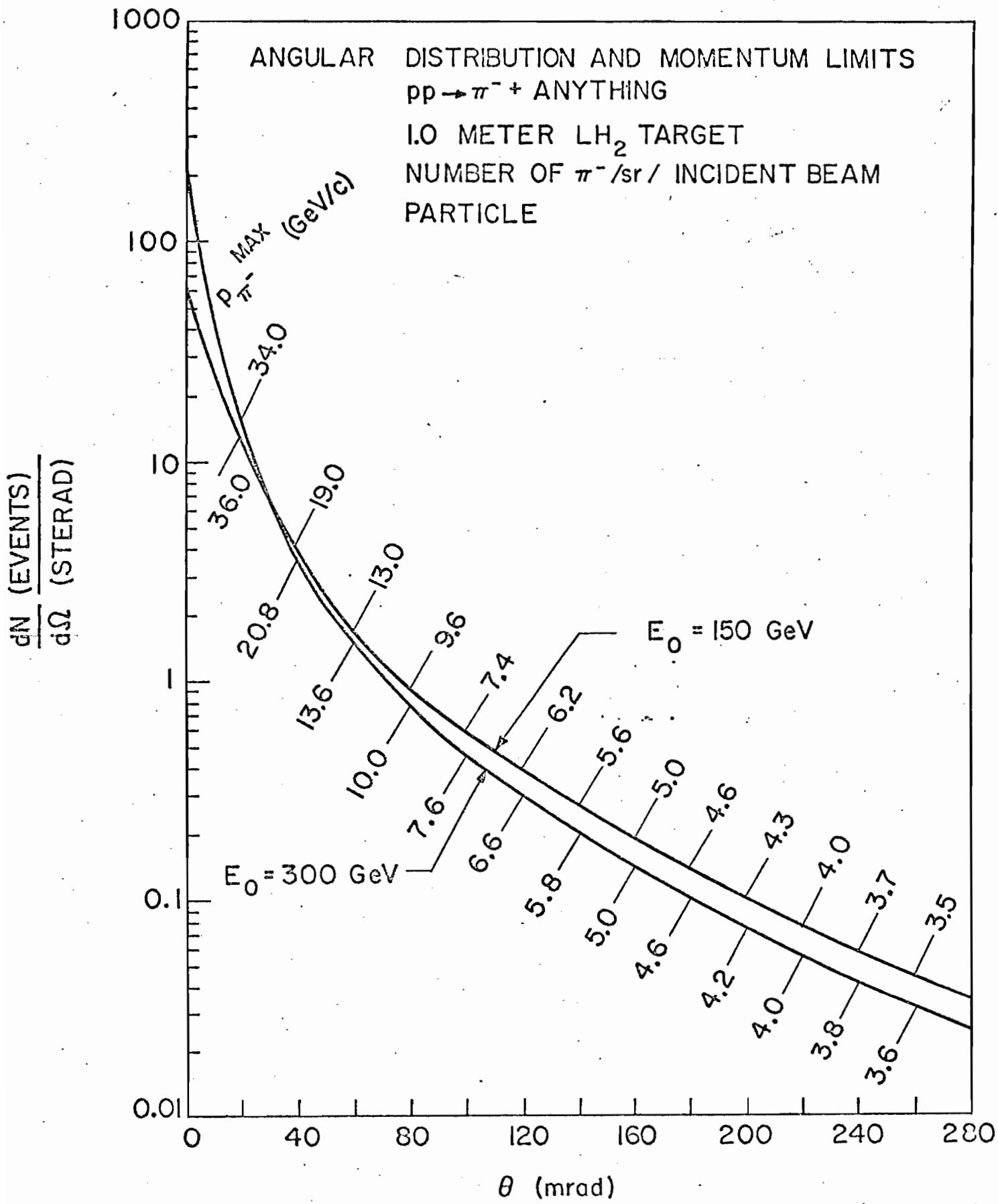


Figure 8

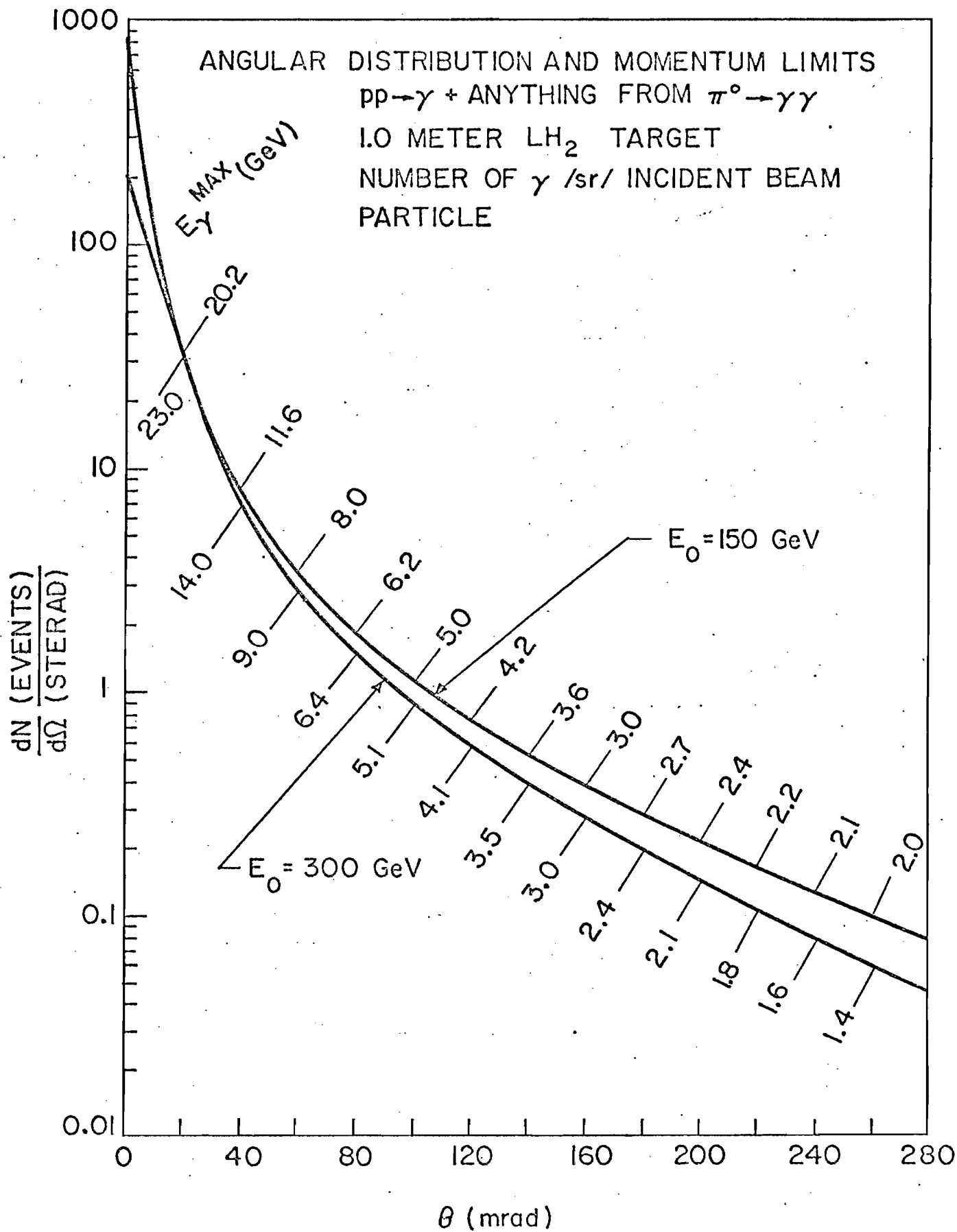


Figure 9

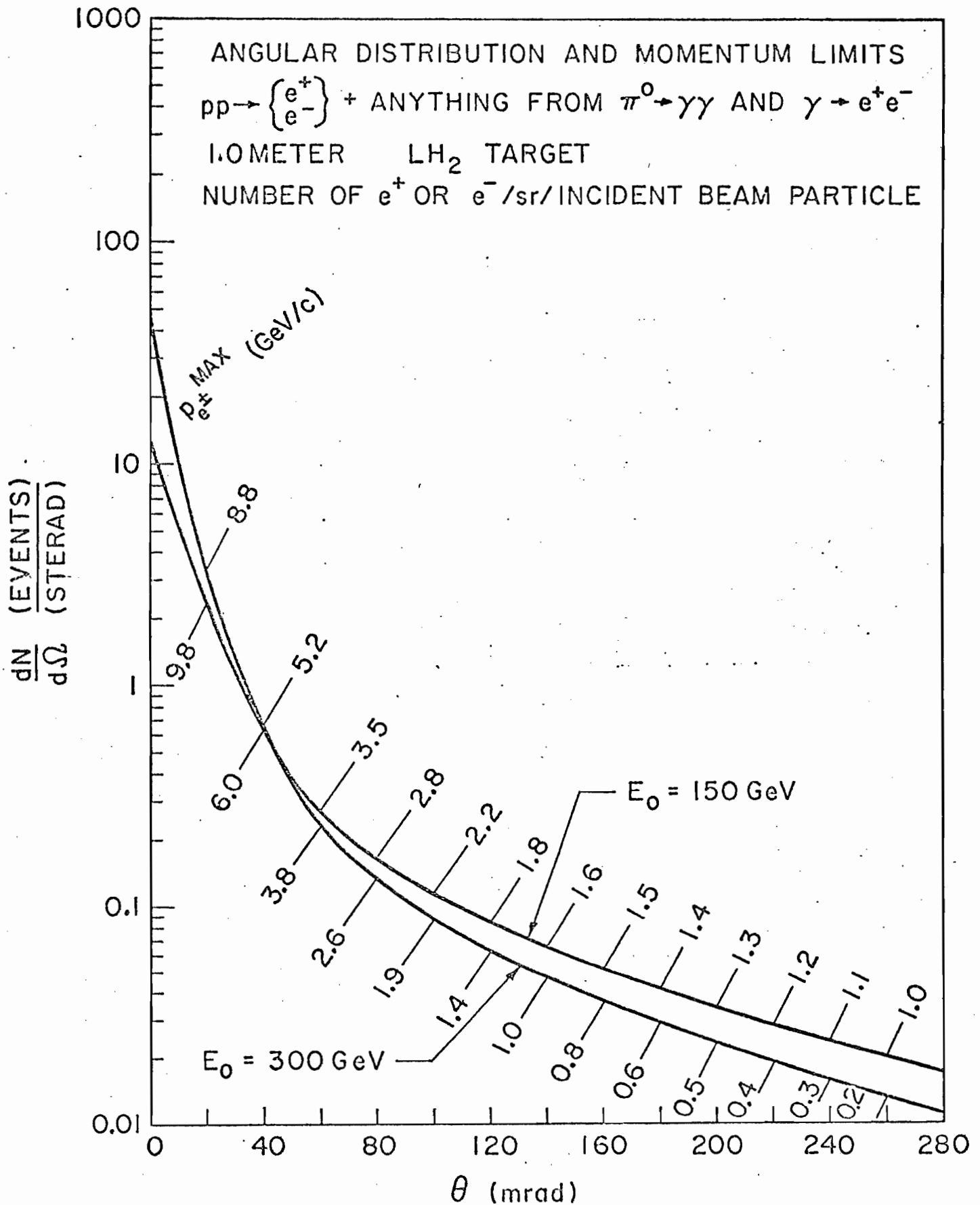


Figure 10

Professor Robert R. Wilson

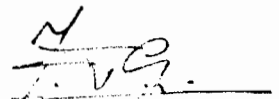
23 January 1973

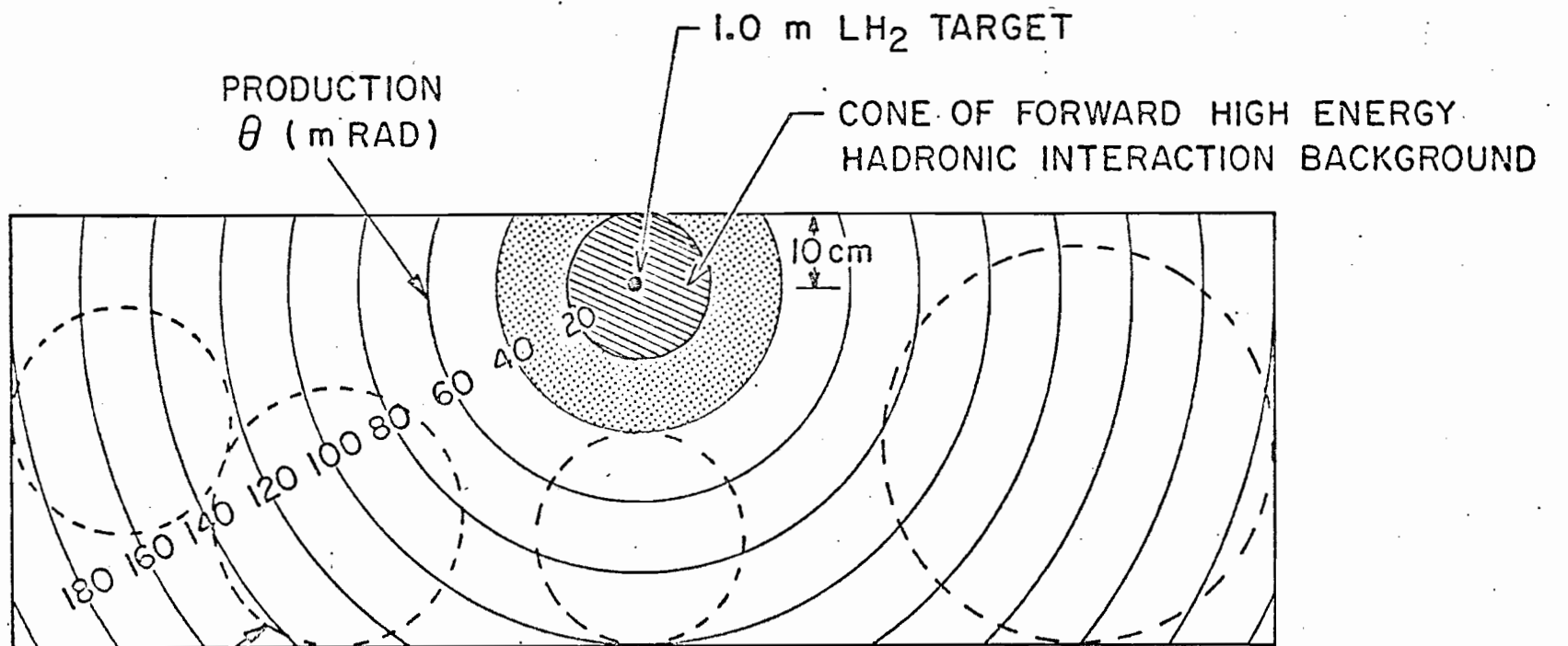
Technical Attachment III

Analyzing Magnet Dimensional Requirements for #192

A 100 kgauss-meter analyzing magnet is required to observe the reactions in #192 and also in #193. In both cases, this magnet serves the needs of several important purposes. These are: a) analyzing the momenta of energetic charged particles produced at large angles in triggered events; b) bypassing from our detectors, the beam and high energy background particles in the forward cone, without causing any other harmful secondary interactions; c) trapping the background of low energy charged particles which are produced mostly at large angles. Moreover, the magnet must have sufficient gap and width, such that a direct line of sight is available between target and detectors, to allow for the observation of produced large angle and energetic gamma rays. Sufficient gap and width are also required for the observation of large angle and energetic electron and muon pairs, detected in coincidence. Finally, the design of a magnet having reasonable magnetic field uniformity requires an aspect ratio of magnet width to gap of at least 2.5:1.

In Figure 11 the required relationship is shown, between target emplacement, detector coverages at large production angles and the region of high energy and otherwise harmful background in #192. This relationship is shown dimensionally projected at the exit face of a 5 meter-long magnet. The attached background studies have influenced us to redesign the superconducting 20 kgauss magnet for #192 (and also for #193) to have a gap of 24 inches. The feature of having superconducting coils in this magnet has allowed us to make an efficient and economical redesign.


R. Wilson



TYPICAL EFFECTIVE COVERAGE OF TASC (γ - e^{\pm} - μ^{\pm}) SPECTROMETERS BEHIND
 60 cm GAP, 180 cm WIDE, 500 cm LONG
 20 kG SUPERCONDUCTING MAGNET

Figure 11

AMENDMENT FERMILAB Proposal # 193

DATE: 14 April, 1975

To : J. R. Sanford, FERMILAB

FROM : Z.G.T. Guiragossian, HEPL

SUBJECT: 10⁹, 50-800 GeV Pure Electrons at the Proton-West First Corrected Focus for E-193

This note describes the manner of converting the high intensity P-West secondary beam at FERMILAB into a pure electron beam, to be used at the first corrected focus of this beam line. Compared with previous designs by us for the P-East Area in which conventional magnets were used, at the P-West first corrected focus the intensity and purity of electrons is unsurpassed. This is strictly due to a) the use of superconducting magnets in the P-West beam and b) the excellent geometrical beam design of the P-West beam by B.C. Cox.

We demonstrate that when this beam is tuned as described here, at the first corrected focus, 10^9 electrons/pulse are obtained with absolutely no contamination in beam spot (a pure electron beam) over electron beam energy dynamic range of 50 GeV to 800 GeV, whereby contamination pions are separated by more than three times the electron spot size. Thus, a very versatile facility is provided at the FERMILAB for electron and pion experiments using the same installation, and making this the highest energy, highest intensity and largest duty cycle electron beam in the world.

1. THE PROTON-WEST BEAM

The Proton-West beam line is conceived as a large acceptance high intensity secondary beam with the use of entirely superconducting beam elements and an ability of reaching up to 1000 GeV/c. For example, already prototyped superconducting dipoles will be used which provide maximum field strengths of 40 kgauss, where only 12-14 kgauss strengths are needed for 300 GeV/c operation. The beam is designed by B.C. Cox, using similar sextupole correcting principles as in our earlier experience (see Z.G.T. Guiragossian and R. E. Rand, Nucl. Instr. Meth. 107, 237, 1973 and "General Rules of Sextupole Corrections in Beams" Technical Note, June 1974 by Z.G.T. Guiragossian). Thus, a small spot size is obtained at the experimental areas without sacrificing beam intensity from the production target. The calculated spot size at the first corrected focus is ± 2 mm horizontally and ± 7.5 mm vertically for a momentum acceptance of $\pm 5\%$. The beam's angular acceptance is 30 μ sterad.

The beam will have two corrected foci for two successively placed experimental stations. For the purpose of this study, we have centered our attention at the first corrected focus since this area will be implemented first, to examine the suitability of producing a pure electron beam satisfying the requirements of our electron experiment E-193.

The P-West beam qualities are entirely adequate and meeting with the requirements of our pion experiments E-192. From what is demonstrated in this Note, the P-West beam qualities are unsurpassed in providing a very high intensity pure electron beam. Consequently, both our pion and the follow-up electron experiments can be executed using the same apparatus and also at the same location, at the first experimental station.

II. EXPECTED ELECTRON INTENSITIES IN THE PROTON-WEST BEAM

Figure 1 shows the predicted electron yield in the Proton-East beam according to our calculation of 1971, together with a preliminary measurement of electron yield in that beam made by the experiment E-25 group with 300 GeV/c incident protons. The Proton-East beam has an acceptance of 12 μ sterad-% (FW). Our prediction is high by a factor of 2.3-3 in the useful region of $X = 0.3 - 0.6$, where $X = P_{\text{electron}}/P_{\text{proton}}$.

The Proton-West beam has an acceptance of 290 μ sterad-% (FW). Therefore, to have the expected electron intensities in the Proton-West beam we scale our calculations by the factor of $(290/12)/2.3 \approx 10$. This is shown in Figure 2 for the case of 400 GeV/c incident protons, where 200 GeV 10^9 electrons/ 10^{13} incident protons are expected.

III. PURE ELECTRON BEAM AT THE FIRST CORRECTED FOCUS OF P-WEST

To have a good electron beam it is required that there be three capabilities. (1) Front-end targeting capabilities for protons to strike a 40 cm long Beryllium target and to be dumped, π^0 gamma-rays to be collected onto a 1.6 mm Uranium foil to produce electrons. This targeting system now has been incorporated in the Proton-West beam design. (2) Small spot size at a recombined focus which is achieved by sextupole corrections so that electron beam intensity at production is preserved. A way of achieving this capability has been demonstrated by B.C. Cox for the current Proton-West beam design. (3) Sufficient amount of bending power in the beam-line to force synchrotron radiation energy loss of electrons, in a distributed fashion throughout the beam-line dipoles. This capability is used to produce a separated electron beam spot, displaced away from the image of surviving background hadronic particles. (A further amount of electron purity is obtained by placing a 3.3 meters long liquid deuterium filter ahead of the Uranium foil. In view of the following demonstration

we have no need for such a filter and herewith dispense with this complication.)

A. Synchrotron Radiation

The fractional energy loss of electrons as they traverse beam-line dipoles is given by:

$$\Delta E/E = 1.26 \times 10^{-8} E (\sum_i B_i^2) L \quad (1)$$

where B_i are the dipole strengths in kgauss, L is the dipole length in meters (uniform length magnets are assumed with $L = 3.05$ m) and E is the electron beam energy in GeV. In beam lines, dipoles are located in clusters, usually having 3 or 4 uniform length dipoles in each cluster. To have transmission of electrons, the magnet settings must be successively tuned down to compensate for the individual amounts of synchrotron radiation. Thus electrons remain on the optics axis. A good fraction of the hadronic background, being off tune, is lost in the beam line and whatever survives is focussed onto a beam spot displaced off axis.

Because synchrotron radiation (S.R) occurs continuously throughout a magnet, the additional angular deflection caused by the energy loss of electrons after exiting a magnet is given by the integral:

$$\begin{aligned} \Delta \theta_{SR} &= \int_0^L \frac{0.03 B dL}{P} \left(\frac{\Delta P}{P} \right)_{SR} \\ &= 1.26 \times 10^{-8} \times 0.03 \int \frac{B dL}{P} P B^2 L \\ &= 1.26 \times 10^{-8} \times 0.03 \frac{B^3 L^2}{2} = 1.89 \times 10^{-10} B^3 L^2 \end{aligned}$$

In a cluster of uniform length magnets the net angular deflection is:

$$\Delta \theta_{SR} = 1.89 \times 10^{-10} (\sum_i B_i^3) L^2 \quad (2)$$

or equivalently, hadronic particles suffer this additional deflection when the magnets are tuned down to compensate for synchrotron radiation of electrons. Each magnet is tuned down by the appropriate amount

given by equation (1). It is necessary to tune down each magnet by the full amount of energy loss caused by magnets ahead of it and then also, by one half the amount of energy loss caused by itself. This "radiation compensated tuning" procedure applies to all beam line magnets - dipoles, quadrupoles and sextupoles.

Finally, after this procedure the off-axis focus of surviving hadronic background is found a distance d away from the on-axis focus of electrons, where d in mm is given by:

$$d(\text{mm}) = \sum_j d_j = 1.89 \times 10^{-7} L^2 \sum_j (\sum_i B_i^3) l_j \quad (3)$$

l_j in meters is the lever arm between clusters of dipoles forming beam-line bends. Of course, the proper evaluation of image separation requires a ray tracing program to take into consideration the effect of radiation loss in quadrupoles and sextupoles as well. However, equation (3) gives a good lower limit and we have ascertained that in one example with conventional magnets, equation (3) gives a separation which is some 15% lower than the Monte Carlo ray tracing program. With superconducting magnets we could be underestimating more than this, the goodness of these separations.

Clearly, to have a pure electron beam on an experimental target it is necessary to have a) a small spot size together with b) an electron-pion image separation which is at least as much as the spot size. Thus, a suitable scraper or veto counter can be used to eliminate the small amount of surviving hadronic background localized at the displaced focus. An example of separated beam profiles is shown in Figure 3 where conventional magnets are used up to a second corrected focus. This is the result of our earlier design effort, showing the best that can be done with conventional magnets.

B. Enhanced Synchrotron Radiation in Beam-Lines

Up to the limit of available beam dipole field strengths we can force synchrotron radiation to occur in an optimum manner by choosing conditions which maximize a) synchrotron radiation caused energy loss of electrons ($\sum_i B_i^2 \times L$ effect), b) synchrotron radiation caused angular deflection

$$(\sum_i B_i^3 \times L^2 \text{ effect})$$

while, c) beam line geometry is preserved and d) off-axis hadronic particle displacement is maximum

$$(\sum_i B_i^3 \times L^2 \times l_j \text{ effect}) .$$

In these considerations the power of superconducting magnets is made evident by the following example: for 100 GeV electrons a single

36 kgauss 3.05 meters long dipole with a lever arm of 100 meters will cause by synchrotron radiation a fractional loss in momentum of 0.506%, which makes possible for an additional deflection of 82 μ rad, translating to a shift of 8.2 mm at the end of the lever arm. This unique capability is made available only by the use of superconducting beam line magnets, a feature which is already planned for the Proton-West beam.

In cases where beam-line dipoles are found in clusters of 3 or 4 magnets and especially at lower beam momenta, we can force enhancement of synchrotron radiation by having reversed bends in some magnets and running others at maximum field strength, while preserving beam-line geometry. This technique was devised and used in our earlier studies and the separation effects produced by it is shown in Figures 3(a) and 3(b), where conventional magnets were used with $B_{\max} \leq 14$ kgauss. The same technique produces spectacular effects in a much shorter beam-line when superconducting magnets are used. For the purpose of this demonstration, conservatively we restrict $B_{\max} \leq 36$ kgauss, even though prototyped dipoles for the P-West beam are designed to operate at $B_{\max} = 40$ kgauss.

In each cluster we wish to optimize for energy loss ($\sum_i B_i^2 L$) and maximum deflection caused by synchrotron radiation ($\sum_i B_i^3 L^2$). Among several configurations in polarity and in strength, the best choice is found to be that which has maximum field strength at the center of the cluster with magnet polarity in normal mode. By concentrating maximum field strength on the central magnet in normal polarity and lesser amounts of strength in opposite polarity on the outer magnets (+ + + \rightarrow - \oplus - or, + + + + \rightarrow - \oplus \oplus -) the $\sum_i B_i^3$ term is optimized, thus producing optimum amount of electron-pion separation at lower momenta. This configuration can be scaled upwards for higher beam momenta, until reverse bends are not needed to preserve beam-line geometry. Even beyond this point, the $\sum_i B_i^3$ term is optimized by concentrating maximum field at the center of a cluster, balanced by lower field strengths in same polarity on the outer magnets (+ + + \rightarrow + \oplus +). This configuration continues to win until at very high momenta all magnets in a cluster are running at equal strengths.

C. Conditions for Preserving Beam-Line Geometry for Maximum Synchrotron Radiation

We consider a cluster of three magnets, B_1, B_2, B_3 , with the beam entering at B_1 and leaving from B_3 . The magnets are set to bend respectively by amounts of $\alpha_1, \alpha_2, \alpha_3$ producing a fixed beam line angle θ_{bend} . At fixed momentum, if the tune or polarity of these magnets is changed to some arbitrary values, producing bends $\beta_1, \beta_2, \beta_3$, beam-line geometry is preserved only if θ_{bend} is maintained and also if rays come out on axis without a parallel displacement:

that is,
$$\theta_{\text{bend}} = \alpha_1 + \alpha_2 + \alpha_3 = \beta_1 + \beta_2 + \beta_3 \quad (4)$$

and,
$$3\alpha_1 + 2\alpha_2 + \alpha_3 = 3\beta_1 + 2\beta_2 + \beta_3 \quad (5)$$

(the case of a cluster of four magnets is: $4\alpha_1 + 3\alpha_2 + 2\alpha_3 + \alpha_4 = 4\beta_1 + 3\beta_2 + 2\beta_3 + \beta_4$).

Conditions (4) and (5) can be satisfied simultaneously only by having a symmetrical arrangement where $\alpha_1 = \alpha_3$ and $\beta_1 = \beta_3$. Thus,

$$2\alpha_1 + \alpha_2 = 2\beta_1 + \beta_2 \quad (6)$$

In hadronic secondary beams, magnets in a cluster usually are set to bend by equal amounts so that $\alpha_1 = \alpha_2 = \alpha_3 = \alpha_0$ and equation (6) reduces to:

$$\theta_{\text{bend}} = 3\alpha_0 = 2\beta_1 + \beta_2 \quad (7)$$

Let B_0 be the field strength of one of the magnets, say at 300 GeV/c, in a cluster of three magnets of equal strength and polarity. In going from the tune of + + + to that of - \oplus - :

$$\begin{array}{ccccccc} B_1 & = & B_2 & = & B_3 & = & B_0 & & B_1 & B_2 & B_3 & = & B_1 \\ + & & + & & + & & & \rightarrow & - & + & - & & \end{array}$$

equation (7) requires that $(3\alpha_0 = - 2\beta_1 + \beta_2)$

$$B_1 = \frac{B_2 - 3B_0(p/300)}{2} \quad (8)$$

where B_2 is set at some maximum value and B_0 is known from beam design. This configuration applies for electron beam momenta of less than 300 GeV/c. Similarly, the tune of + \oplus + requires that:

$$B_1 = \frac{3 B_0 (p/300) - B_2}{2} \quad (9)$$

where again B_2 is set at a maximum value. This configuration applies for electron beam momentum of more than 300 GeV/c. At 300 GeV/c $B_1 = B_3 = 0$ and $B_2 = 3 B_0$. This scheme optimizes the $\sum B_i^3$ term and¹ this provides a maximum amount of synchrotron radiation¹ caused deflections from each cluster. In particular it allows us to have excellent separation of electrons at lower momenta where electron yield is extremely high.

IV. ELECTRON PION IMAGE SEPARATIONS AT THE FIRST CORRECTED FOCUS OF THE P-WEST BEAM.

The Proton-West beam design by B. C. Cox is sufficiently well advanced at this time, such that for the purpose of our demonstration realistic beam-line bends and nominal dipole settings can be used. Down to the first corrected focus, the Proton-West beam is described by two major bends. Each bend is caused by a cluster of three superconducting dipoles. These are 10 ft long superconducting magnets designed to provide maximum field strength of 40 gauss.

The external proton beam will strike a Beryllium target some 161 ft ahead of the first bend; a sufficient distance for the front-end targeting arrangement, both for the production of pion beams and electron beams.

The nominal dipole settings are given for a 300 GeV/c pion beam, together with beam-line bends and lever arm behind each cluster.

Dipole Cluster	(kgauss) B_1, B_2, B_3	Total Field Length 3 L	θ Bend	Lever Arm
1	+ 12, + 12, + 12	30 ft	0.628°	325 ft
2	+ 13.7, + 13.7, + 13.7 (B_4, B_5, B_6)	30 ft	0.717°	184 ft

It is necessary that the full complement of beam-line magnets be installed at the time when the electron beam is produced. These are: 6 dipoles, 12 quadrupoles and 4 sextupoles, up to the first corrected focus. It is also necessary to control each dipole independently, in polarity and field strength. Practically, the controls of dipoles B_1 and B_3 , and, B_4 and B_6 can be tied together.

The attached tables give a) optimum dipole settings to enhance synchrotron radiation caused image separations of electrons and b) the amount of image separation of surviving hadronic background, as a function of several electron beam momentum values. In each beam momentum case, the first entries of the B_i columns are dipole tunes for the production of a standard hadronic¹ secondary beam. Below these, the second entries are magnet tunes according to equations (8) or (9) to provide optimum amounts of synchrotron radiation caused deflections of electrons (largest possible $\sum B_i^3$), while preserving beam-line geometry. With these settings, the fractional momentum loss of electrons is calculated using equation (1) and these appear in the next column. The third entries under the B_i headings are dipole strengths tuned down to compensate for synchrotron radiation energy loss of electrons and in this manner, to keep electrons on-axis and hadrons off beam axis.

In particular, each individual magnet will be tuned down successively to have uniform radiation compensation in the manner described earlier. For the purpose of this demonstration we have simply used $1/2 (\Delta p/p)_{SR}$, obtained from and applied to each entire cluster.

Dipoles are now tuned to transmit electrons and to cause an additional deflection on background hadrons by the amount of $\Delta \theta_{SR}$. This is given in the next column and is calculated using equation (2). Finally, the off-axis shift of hadronic background particles is calculated using equation (3). d_1 is the shift caused by the first dipole cluster at the end of lever arm which is taken to be the distance between first and second bends; d_2 is the shift caused by the second dipole cluster at the end of its lever arm, the distance between the second bend and the momentum recombined focus. Thus, d , the sum of $d_1 + d_2$, realistically describes the total image shift of surviving hadronic² background particles at the first corrected focus of the P-West beam. Again, we emphasize this estimate of d is a lower limit and we have tested the validity of this approximate method against a precise Monte Carlo ray tracing program. Note that by treating lever arms of dipoles as in the above, the intermediate focussing effects of quadrupoles is averaged and the shift of surviving hadrons is estimated.

The results of our calculations are displayed in Figure 4, in which d (mm) is given as a function of electrons beam momenta. On the same figure, the electron beam spot size is also shown. (At lower beam momenta the spot size image is slightly larger, caused by multiple scattering broadening of source size at the Uranium converter foil. For comparison purposes, in Figure 4 we also show a similar curve describing the electron-pion image separation as obtained from our earlier studies in which conventional magnets were used for the Proton-East beam (see also Figure 3). This comparison is spectacular. Figure 4 demonstrates that the resulting electron beam at the first corrected focus of P-West is pure at all beam momenta. The surviving pion background is imaged a distance away of about three times the spot size of on-axis electrons, and therefore can be absorbed in a Tungsten block.

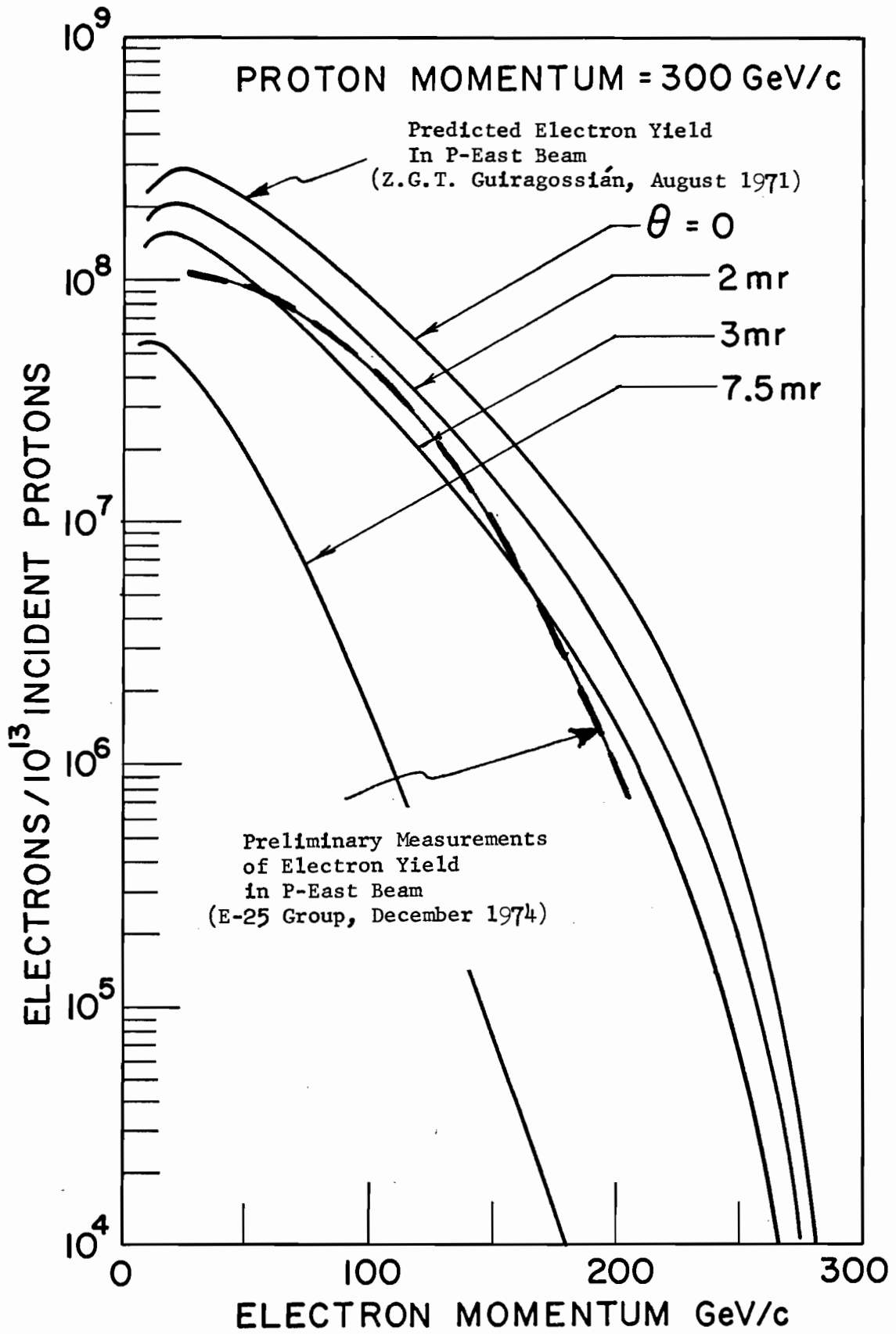


FIGURE 1

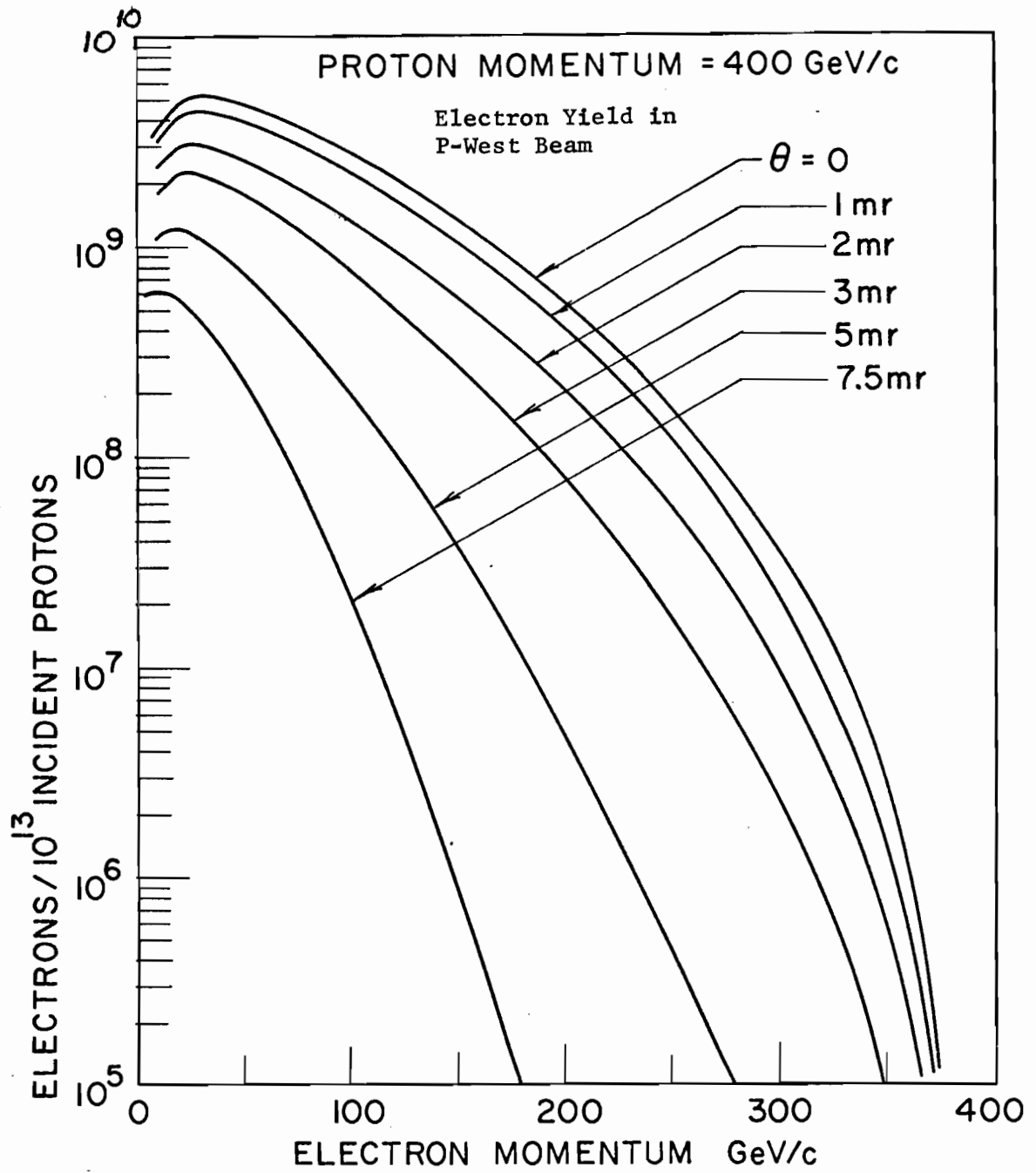
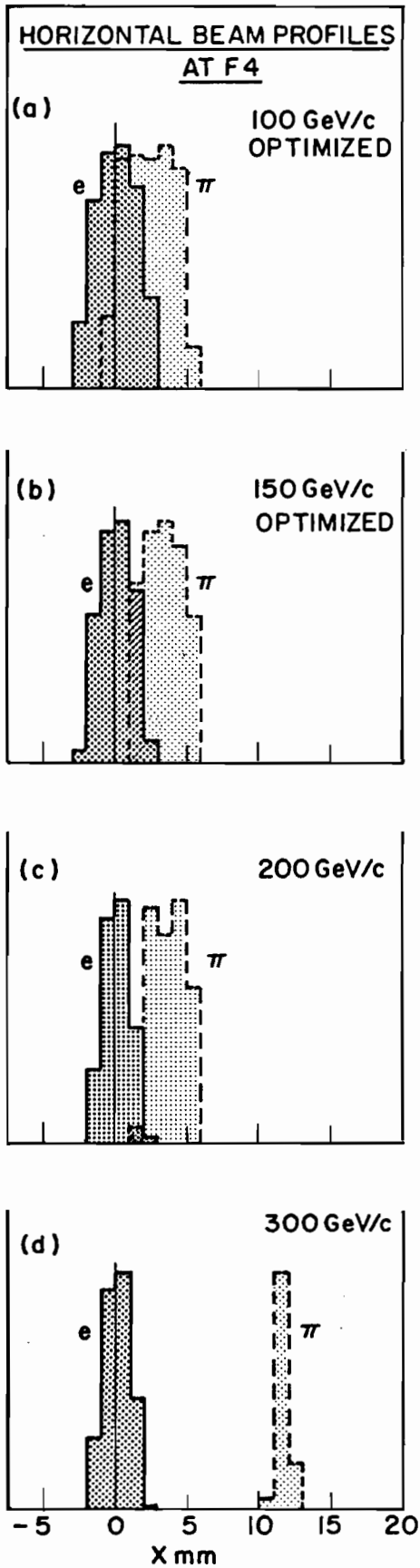


FIGURE 2



PROTON-EAST BEAM
2nd Corrected Focus
CONVENTIONAL Magnets.

Fig. 3. Electron and pion horizontal beam profiles at F4 showing the effect of synchrotron radiation in a radiation compensated beam.

(a) 100 GeV/c, (b) 150 GeV/c. At these two momenta all the magnets in the beam line are used, some with reversed polarity, to maximize ΣB^2 and enhance the e, π separation, (c) 200 GeV/c, (d) 300 GeV/c. At these higher momenta, only the necessary number of bending magnets consistent with $B \leq 14$ kgauss are used.

FIGURE 3



ENGINEERING NOTE

E-192/193

12

SUBJECT

10^9 , 50 - 800 GeV PURE ELECTRONS
at P-West 1st corrected focus.

NAME

Z.G.T. GUIRAGOSSIAN

DATE

4-8-75

REVISION DATE

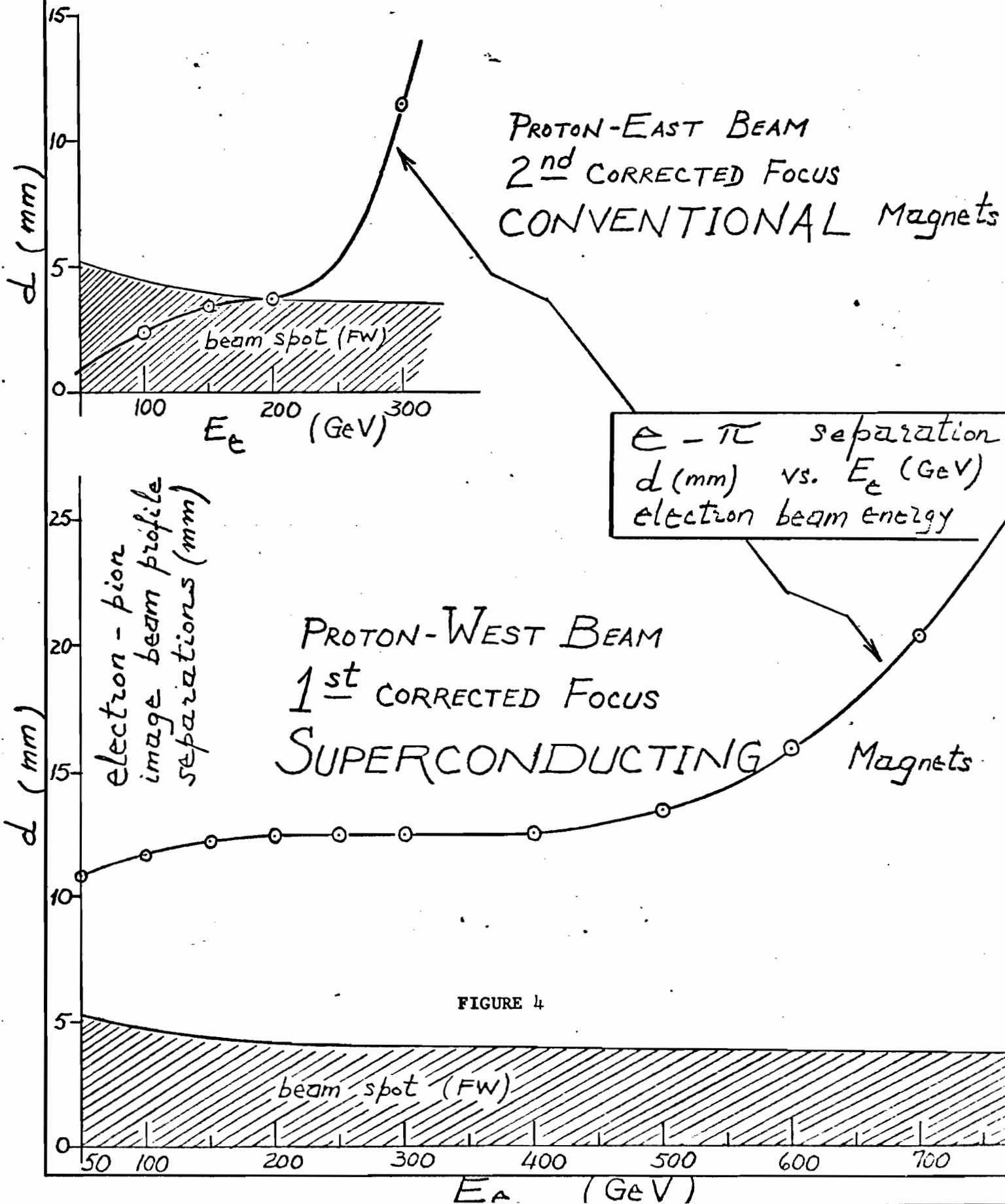


FIGURE 4



SUBJECT

10⁹, 50-800 GeV PURE ELECTRONS
at P-West 1st corrected focus.

NAME

Z. G. T. GUIRAGOSSIAN

DATE

4-8-75

REVISION DATE

P _e (GeV/c) beam	Proton-West Beam, 1 st corrected focus. (Superconducting B, Q, S) B ₁ , B ₂ , B ₃ 1 st bend dipole cluster; $\theta_{\text{bend}} = 0.628^\circ$; $l = 99.06$ m, lever arm $L_B = 3.05$ m; $B_{\text{max}} = 40$ kgauss.						
	B ₁ (kgauss)	B ₂ (kgauss)	B ₃ (kgauss)	$\Delta p/p \times 10^{-2}$ synch. rad.	$\Delta \theta \times 10^6$ synch. rad.	d ₁ (mm)	d (total) = d ₁ + d ₂ mm
50	+2 -15 -14.975	+2 +36 +35.940	+2 -15 -14.975	0.336	69.8	6.92	10.9
100	+4 -12 -11.963	+4 +36 +35.890	+4 -12 -11.963	0.609	75.3	7.46	11.8
150	+6 -9 -8.962	+6 +36 +35.849	+6 -9 -8.962	0.841	78.5	7.77	12.2
200	+8 -6 -5.968	+8 +36 +35.811	+8 -6 -5.968	1.051	80.0	7.93	12.4
250	+10 -3 -2.981	+10 +36 +35.773	+10 -3 -2.981	1.262	80.4	7.96	12.5
300	+12 0 0	+12 +36 +35.731	+12 0 0	1.494	80.2	7.95	12.4
400	+16 +6 +5.937	+16 +36 +35.621	+16 +6 +5.937	2.103	80.2	7.95	12.6
500	+20 +12 +11.817	+20 +36 +35.452	+20 +12 +11.817	3.044	84.1	8.34	13.5
600	+24 +18 +17.597	+24 +36 +35.193	+24 +18 +17.597	4.483	95.8	9.49	16.0
700	+28 +24 +23.210	+28 +36 +34.815	+28 +24 +23.210	6.585	118.2	11.71	20.4
800	+32 +30 +28.572	+32 +36 +34.287	+32 +30 +28.572	9.518	152.9	15.15	27.1



ENGINEERING NOTE

E-192/193

14

SUBJECT

10^9 , 50-800 GeV PURE ELECTRONS
at P-West 1st corrected focus.

NAME

Z.G.T. GUIRAGOSSIAN

DATE

4-8-75

REVISION DATE

P_e (GeV/c) beam	Proton-West Beam, 1 st corrected focus. (superconducting B, Q, S) B ₄ , B ₅ , B ₆ 2 nd bend dipole cluster; $\theta_{\text{bend}} = 0.717^\circ$; $l = 56.08$ m L _B = 3.05 m; B _{max} = 40 kgauss. level arm					
	(kgauss) B ₄	(kgauss) B ₅	(kgauss) B ₆	$\Delta p/p \times 10^{-2}$ synch. rad	$\Delta \theta \times 10^{-6}$ synch. rad	d_2 (mm)
50	+2.283 -14.575 -14.551	+2.283 +36 +35.940	+2.283 -14.575 -14.551	0.331	70.8	3.97
100	+4.567 -11.150 -11.117	+4.567 +36 +35.893	+4.567 -11.150 -11.117	0.594	76.5	4.29
150	+6.850 -7.725 -7.693	+6.850 +36 +35.853	+6.850 -7.725 -7.693	0.816	79.4	4.45
200	+9.133 -4.300 -4.278	+9.133 +36 +35.816	+9.133 -4.300 -4.278	1.025	80.5	4.51
250	+11.417 -0.875 -0.870	+11.417 +36 +35.776	+11.417 -0.875 -0.870	1.247	80.5	4.51
300	+13.700 +2.550 +2.531	+13.700 +36 +35.728	+13.700 +2.550 +2.531	1.509	80.2	4.50
400	+18.267 +9.400 +9.294	+18.267 +36 +35.592	+18.267 +9.400 +9.294	2.264	82.1	4.60
500	+22.833 +16.250 +15.965	+22.833 +36 +35.369	+22.833 +16.250 +15.965	3.505	92.1	5.17
600	+27.400 +23.100 +22.471	+27.400 +36 +35.019	+27.400 +23.100 +22.471	5.449	115.4	6.47
700	+31.966 +29.950 +28.705	+31.966 +36 +34.504	+31.966 +29.950 +28.705	8.313	155.4	8.71
800	+36.533 +34.284	+36.533 +34.284	+36.533 +34.284	12.310	212.6	11.92